Investigating the stability of amyloid assemblies towards fragmentation

Mireb Mishell

University of Kent

DECLARATION

I confirm that the wording of this thesis is entirely my own. No part of the thesis has been copied from scientific journals, websites or any other sources.

Mireb Mishell

December 2020

ACKNOWLEDGEMENTS

First and foremost, I thank my Father YHVH for His Goodness and Grace. Thank you for giving me the strength and guidance to complete this research and thesis.

I would also like to express my sincere gratitude to my project supervisor Dr. Wei-Feng Xue for giving me the opportunity to do this research project. Thank you for your patience, motivation and constant support throughout the project and writing of the thesis. It has been a great privilege to work and study under your guidance.

I am also extremely grateful to have had an amazing lab manager, Tracey Purton. Thank you for teaching me the methodology to carry out the research, your immense knowledge and invaluable guidance. I could not have completed the project without you.

I also thank my fellow lab mates Liam Aubrey, Liisa Lutter and Sarina Sanami for their friendship, encouragement and insightful suggestions during the course of the project.

Lastly, I thank my parents for their unconditional love, care and continued support. Special thanks goes to my best friend Matthew Milne for his love encouragement. It was a great comfort and relief to be able to talk to you during difficult times. I'm so grateful to have you in my life.

ABSTRACT

Amyloid fibrils are densely packed, highly polymorphic protein aggregates typically found in patients with neurodegenerative disorders such as Alzheimer's and Parkinson's disease. The fibrils are characterised by a cross-β core comprising of a succession of contiguous β-strands stacked perpendicularly to the fibril axis. The organisation attributes to the tough and highly stable nature of amyloid structures that allows them to withstand degradation and serve a variety of normal physiological functions in organisms ranging from bacteria to mammals. It is unclear why some amyloid structures are beneficial and others pathogenic. Increasing research into the amyloid lifecycle, the process by which soluble monomeric proteins and peptides misfold and self-assemble into amyloid fibrils, has revealed four main stages: primary nucleation, elongation, secondary nucleation and fibril fragmentation. Interestingly, fragmentation is thought to play a key role in the propagation of the amyloid conformation due to striking effects on the fibril structure, therefore it may provide insight into their stability and pathogenicity. In this study, the mechanical stability of *in vitro* formed fibrils of Sup35NM, a functional prion, and α-synuclein, a prion-like amyloid associated with Parkinson's disease, were analysed by sonication followed by atomic force microscopy imaging. Results confirm a decrease in the mean α-synuclein particle length with increased sonication, as well as an increase in the number of fibril extension sites for elongation. Both factors would significantly enhance the potential for cytotoxicity due to increased biological availability of short amyloid particles for interaction with other cellular components and membranes, the diffusion across which is further enhanced by the reduction in overall fibril size. The infective potential of amyloid particles is measured by the likelihood of internalisation of particles by cells. Therefore, fragmentation is crucial for the propagation of the amyloid conformation since it successfully increases the load of small cytotoxic amyloid species with highly infectious potentials compared to their longer counterparts.

TABLE OF CONTENTS

CHAPTER 4: DISCUSSION

ABBREVIATIONS

AD	Alzheimer's Disease
Aβ	Amyloid-β
AβO	Amyloid-β Oligomer
ACM	Amyloid-Converting Motif
α-Syn	α-synuclein
αFFB	α-synuclein Formation Buffer
AFM	Atomic Force Microscopy
APP	Amyloid Precursor Protein
CD	Circular dichroism
CJD	Creutzfeldt–Jakob disease
CMA	Chaperone-Mediated Autophagy
CR	Congo Red
CSF	Cerebrospinal Fluid
Cryo-TEM	Cryogenic Transmission Electron Microscopy
CV	Column Volume
ER	Endoplasmic Reticulum
EM	Electron Microscopy
FTIR	Fourier Transform Infrared
GdnHCL	Guanidine Hydrochloride
Hsp	Heat-Shock Protein
HD	Huntington's Disease

LB	Lysogeny Broth
mQH$_2$O	Mili Q Water
MLB	Melki Lysis Buffer
MLBG	Melki Lysis Buffer with Guanidine (for denaturing)
MLBGE	Melki Lysis Buffer with Guanidine and increased Imidazole (for Elution)
NAC	Non-Amyloid-β Component
NCC	Nucleated Conformation Conversion Model
NFT	Neurofibrillary Tangle
NMR	Nuclear Magnetic Resonance
NP	Nucleated Polymerisation Model
PALM	Photoactivated Localisation Microscopy
PD	Parkinson's Disease
PFD	Prion Forming Domain
PMEL	Premelanosome Protein
PSPD	Position Sensitive Photo-Detector
PrP^{C}	Cellular Prion Protein
PrP^{SC}	Scrapie Prion Protein
sHsp	Small Heat Shock Proteins
ssNMR	Solid State Nuclear Magnetic Resonance
SFFB	Sup35NM Fibril Formation Buffer
SANS	Small-Angel Neutron Scattering
SAXS	Small-Angle X-ray Scattering

SIM	Structured Illumination Microscopy
STED	Stimulated Emission Depletion
STORM	Stochastic Optical Reconstruction Microscopy
TEM	Transmission Electron Microscopy
ThT	Thioflavin T
TSE	Transmissible Spongiform Encephalopathies
UPS	Ubiquitin-Proteasome System
WT	Wild Type

CHAPTER 1: INTRODUCTION

1.1 Overview of the amyloid lifecycle and biological consequences

1.1.1 Definition of amyloid

Amyloid is a 3D conformational state that can be adopted by most soluble monomeric proteins and peptides upon misfolding events (Gallardo et al., 2020; Ke et al., 2020). Amyloid formation proceeds by the self-assembly of these misfolded species into large, unbranched fibrillar structures (Fig 1.1.1b) that are built from repetitively stacked β-strands aligned perpendicular to the fibril axis (Fig 1.1.1e), generating the 'amyloid fold' (Greenwald and Riek, 2010; Eichner and Radford, 2011). The β-strands, stabilised by extensive mainchain hydrogen bonding, subsequently form long ribbon-like cross β-sheets (Fig 1.1.1d) that are further packed against each other to yield larger structures called protofilaments (Fig 1.1.1c), which assemble together into amyloid fibrils (Fitzpatrick et al., 2013). The first known observation of amyloid was in 1639 but the term was coined much later in 1854 by Rudolf Virchow who discovered these structures between cells in various tissues and organs of patients who died of systemic amyloidosis (Cohen, 1986; Kyle, 2001). These pathological proteinaceous deposits were mistakenly believed to be related to starch due to their histochemical staining property, hence the name amyloid, meaning 'starch-like'. However, the term 'amyloid' has persisted even though in 1859 amyloid fibrils were found to be chemically different from starch due to their ability to bind the dye Congo red and exhibit green birefringence under cross-polarized light (Eichner and Radford, 2011). By this definition, an increasing number of amyloid-forming proteins have been identified, many of which are linked to conditions ranging from Alzheimer's and Parkinson's diseases to type II diabetes. Conversely, those serving vital biological functions in organisms ranging from prokaryotes to humans have also been identified (Chiti and Dobson, 2017; Jackson and Hewitt, 2017).

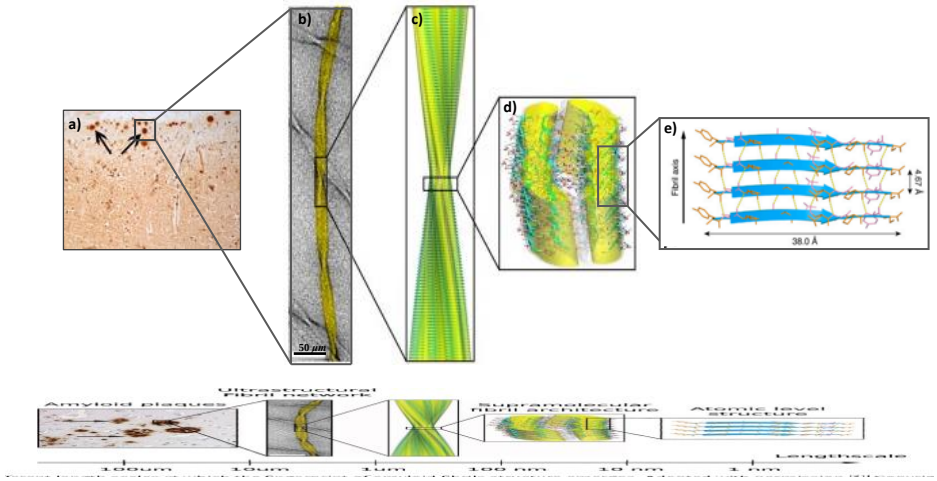

Figure 1.1.1- Structure of Amyloid assemblies. *(a) Small round deposits ("corpora amylacea"), as described by Virchow, observed in the nervous system. (b) An electron micrograph of the ultrastructural cross-β amyloid fibril network formed by an 11-residue fragment of the protein transthyretin. (c) Magic-angle spinning nuclear magnetic resonance (MAS-NMR) atomic-resolution structure (0.5 Å) of the triplet fibril fitted into the cryo-TEM reconstruction. Supramolecular protofilaments exhibit the classic amyloid morphology and are 10 – 20 nm in diameter and 1 – 3 µm in length. (c) Ribbon representation of the highly ordered cross-β core composed of arrays of ß-sheets running parallel to the long axis of the fibrils; oxygen, carbon, and nitrogen atoms are shown in red, grey, and blue, respectively. (e) The ß-sheet viewed perpendicularly to the fibril axis illustrating the parallel in-register ß-strands (blue arrows) and the hydrogen bonds (dotted yellow lines) defining the ß-sheet. Image a from (Cohen, 1986), images b, c, d and e from (Fitzpatrick et al., 2013).*

1.1.2 Atomic structure of amyloid

In 1935, biophysicists Astbury and Dickinson were first to discover the unique yet universal cross-β quaternary conformation of amyloid fibrils using X-ray diffraction. The fibre diffraction pattern revealed distinctive reflections at 4.8 Å and ~10 Å (Fig 1.1.2.1) corresponding to the spacing between β-strands and packing of the side chains between β-

sheets, respectively (Eisenberg and Jucker, 2012). The atomic structure was further confirmed by the characteristic β-sheet signals produced by circular dichroism (CD) spectrophotometry and Fourier transform infrared (FTIR) spectroscopy (Ke et al., 2020). Since the discovery of the amyloid fold, Astbury's hypothesis that all polypeptide chains can adopt a fibrillar structure is now widely recognised as a generic property of all proteins. Interestingly, the cross-β fold is independent of the amino acid sequence and the native fold of the protein. Rather, it arises from wholescale rearrangement of the polypeptide chain and sometimes reassignment of secondary structure elements (Cremades and Dobson, 2018; Gallardo et al., 2020). At the secondary structural level, fibrils have been observed to have a high β-sheet content but some may have a β-sheet content as low as 35% (Zandomeneghi et al., 2004). Developments in X-ray crystallography, solid-state nuclear magnetic resonance (NMR) spectroscopy, and cryogenic transmission electron microscopy (cryo-TEM) techniques have yielded even higher-resolution tertiary and quaternary structures. This has helped shape the modern biophysical definition of amyloid fibrils, which describes the following general features: (1) fibrils are typically several micrometres in length and 10 – 20 nm in diameter; (2) parallel or antiparallel β-sheets (Fig 1.1.2.2) and their self-complementary interdigitating loops constitute the tightly packed hydrophilic amyloid core, the highly repetitive nature of which is attributed to the vast network of intramolecular and intermolecular interactions in the region (Buxbaum and Linke, 2012); (3) a pair of β-sheets run parallel to the fibril axis with their extended strands running perpendicular to the axis; (4) each sheet is a standard Pauling-Corey β-sheet packed "in register," whereby each strand is hydrogen bonded to the strand above and below so that identical side chains are on top of one another along the fibril axis (Eisenberg and Jucker, 2012). As a result of the extensive backbone hydrogen bonding between β-strands within the amyloid core, the end-stage fibril structure is exceptionally stable both thermodynamically and mechanically (Gallardo et al., 2020). Consequently, this region is responsible for the strong

meridional reflection at ~4.8 Å, as well as templating of new peptides to the same amyloid conformation to allow elongation of the corresponding protofilament.

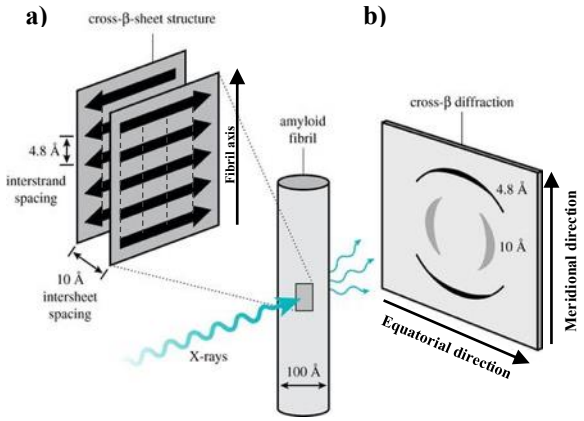

Figure 1.1.2.1- The atomic structure of amyloid fibrils. *(a) Schematic diagram of in parallel cross-β sheets comprising of several polypeptide chains (thick black arrows) that are stacked to form protofilaments. Identical sidechains running perpendicular to the fibril axis are separated by a repetitive inter-strand spacing of 4.8 Å, while the spacing between β-sheets running perpendicular to the fibril axis is ~10 Å. (b) The characteristic X-ray diffraction pattern of the fibril cross-section. A strong, sharp meridional (vertical) reflection at ~4.8 Å is produced by interactions between β-strands, whereas a diffuse equatorial (horizontal) reflection at ~10 Å is produced by the interaction between β-sheets within protofilaments. Image from (Eisenberg and Jucker, 2012).*

Intermolecular hydrogen bonding between main-chain atoms of the polypeptide chain is common to all peptide and protein molecules. Proteins with exposed amide N-H and carbonyl C=O groups on their main-chain are likely to adopt the amyloid state due to the coupling of these groups via hydrogen bonding between the lone pair of electrons on the carbonyl oxygen atom and the amide hydrogen atom (Eisenberg and Jucker, 2012). The electrostatic interactions of all aligned hydrogen bonds mutually polarise each other, further stabilising the interdigitated

β-sheets (Fig 1.1.2.2). However, fibrillar structures with slight shifts between β-sheets have also been observed, causing incompletely paired β-strands at the fibril ends with exposed hydrophobic residues and unsatisfied hydrogen bonds (Cremades and Dobson, 2018). Recruitment of additional polypeptide chains with the cross-β structure could stabilise these exposed fibril ends, allowing extension of the fibril (Fitzpatrick et al., 2013).

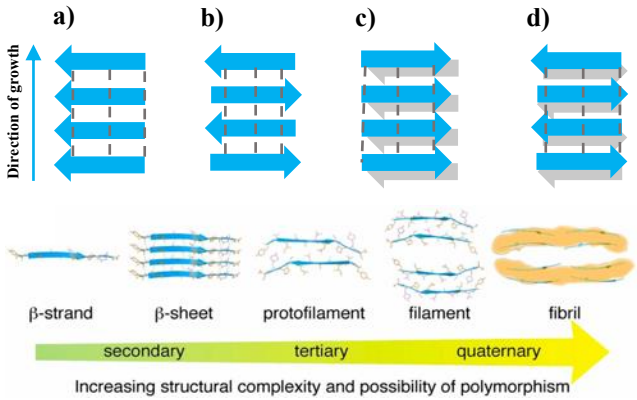

Figure 1.1.2.2- Schematic diagram of the cross-β core structure of amyloid fibrils. *(a) parallel and (b) antiparallel cross-β motifs as observed in fibrils made up of short peptide monomers with a single β-strand segment. (c) double-layered parallel and (d) antiparallel cross-β motifs as observed in fibrils made up of longer peptide monomers with two β-strand segments. In both cases, fibrils may contain multiple copies of the same motif, stacked against each another in a direction perpendicular to the direction of growth and to the β-strand. Backbone hydrogen bonds represented by dashed grey lines. Images a, b, c and d from (Tycko, 2014), image e from (Fitzpatrick et al., 2013).*

Stacking of β-sheets (face-to-face, face-to-back, back-to-back, etc.) results in the formation of protofilaments (Fig 1.1.2.2.e), the most basic unit of cross-β assemblies (Greenwald and Riek, 2010). Within the protofilament, the sidechains protruding from each pair of β-sheets are tightly interdigitated into dry, self-complementing steric zipper arrangements (Fig 1.1.2.3) which correspond to the ~10 Å reflection (Nelson et al., 2005). The interface between the sheets

is devoid of water molecules, thus this motif is termed the "dry steric zipper". Exclusion of water between β-sheets maximises the hydrophobic effect which further stabilises the amyloid core (Eisenberg and Jucker, 2012) as well as the strong sidechain-mainchain and sidechain-sidechain hydrogen bonding from loops that interconnect β-strands (Gallardo et al., 2020). Inter-sheet contacts can also be stabilised by non-specific Van der Waals interactions between sidechains of adjacent protofilaments, aromatic stacking, salt bridges, interactions with solvent, and both polar and nonpolar internal channels (Nelson et al., 2005; Gallardo et al., 2020). Resultant fibrils are composed of varying numbers of protofilaments with features analogous to classical polymers. Thus, amyloid fibrils can withstand degradation by proteases, detergents, and heat (Nelson et al., 2005). The protofilaments may twist around each other in a left- or right-handed fashion. The left-handed twist is the most prevalent form where the β-sheet secondary structure conformation is composed of L-amino acid residues (Aubrey et al., 2020).

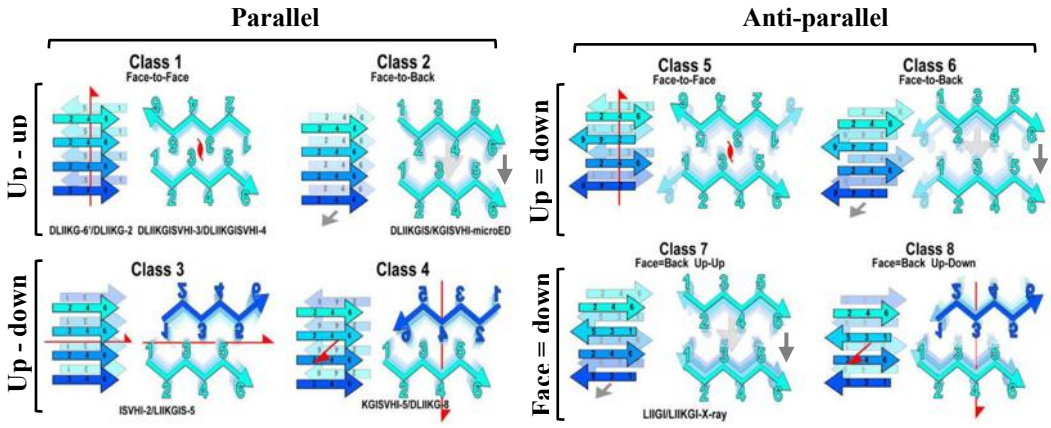

Figure 1.1.2.3- Eight different symmetry classes of amyloid steric zippers. *X-ray diffraction reveals that a pair of identical β-sheets can be classified by the orientation of their faces, the orientation of their strands, and whether the strands within the sheets are parallel or antiparallel. The most common sheet-to-sheet arrangement for steric zippers is face to face (class 1). The red arrows show two-fold screw axes and the grey arrows show translational symmetry. The amino acid sequences below each class are the protein segments belonging to those classes. Image from (Guenther et al., 2018).*

1.1.3 Structural polymorphisms of amyloid

The assembly of amyloid fibrils - from the arrangement of the β-strands into β-sheets, to the packing of the β-sheets into protofilaments and the packing of protofilaments into filaments which ultimately mature into fibrils - produces various structural polymorphisms of amyloid assemblies that may occur at the different stages of the self-assembly process. Polymorphism are structural variations both at the molecular and ultrastructural level among different amyloid fibrils formed by a particular polypeptide chain. Polymorphs can be observed macroscopically via AFM, cryo-TEM and ssNMR which collectively reveal that amyloid fibrils are formed of individual protofilaments whereby different precursor proteins may lead to different numbers of protofilaments (Ke et al., 2020). AFM and EM images in particular can differentiate fibril polymorphs based on the degree of twisting along the longitudinal axis of the fibrils producing varied periodic cross-over distances, the number of filaments per fibril, the shape and size of the cross-sectional area of fibrils (Aubrey et al., 2020). Changes in the environment are likely to promote different local structures, each representing a different polymorph in the aggregation energy landscape (Greenwald and Riek, 2010). As a result, regardless of sharing precursors of different or identical sequences, fibril polymorphs display varying seeding characteristics and rates of fragmentation, which in turn may influence their biological activities such as the potential to propagate in a prion-like manner or the ability to associate with cytotoxic species (Lutter et al., 2019; Aubrey et al., 2020).

Amyloid polymorphisms are divided into two classes, sequence polymorphism and assembly polymorphism (Fig 1.1.3). In sequence polymorphism, a polymorph contains at least one amino acid residue change due to genetic mutations or translational errors at ribosomes. Changes in the polypeptide sequence affect the structure of the amyloid core (segmental polymorphism), packing of the amyloid core (packing polymorphism), and the arrangement of protofilaments

(filament polymorphism) (Lutter et al., 2019). Filament polymorphism is a subclass of assembly polymorphism whereby polymorphs arise due to differences in the number and lateral arrangement of protofilaments within a fibril, as well as the weak and non-specific Van der Waals interactions upon which tight binding between protofilaments is based. Packing and segmental polymorphisms are grouped under core polymorphism, the second subclass of assembly polymorphism whereby polymorphs arise due to changes in the amyloid core as a result of variations in β-sheet content, conformation of non β-strand segments, steric zipper packing and specific contacts between residues. In packing polymorphism, same amyloid segments pack in different ways, possibly due to a registration shift whereby a pair of sheets forming the steric zipper in one polymorph shift their interdigitation in another. These steric zipper arrangements are also dependent on whether β-strands of β-sheets are parallel or antiparallel, and whether adjacent β-sheets that form the steric zipper pack the same or different surfaces together (Lutter et al., 2019). Heterosteric zippers, zippers formed from the interdigitation of non-identical β-sheets, have also been observed in constrained models derived from ssNMR and cyro-EM (Greenwald and Riek, 2010). Such hetero-amyloid spines would also greatly increase the number of potential amyloid polymorphs. In segmental polymorphism, different segments of an amyloid protein are capable of forming different cross-β cores. Regardless of the molecular origins of each polymorph, all are likely to interact with each other forming other types, resulting in a vastly heterogeneous mixture of fibril polymorphs that is often observed within amyloid populations.

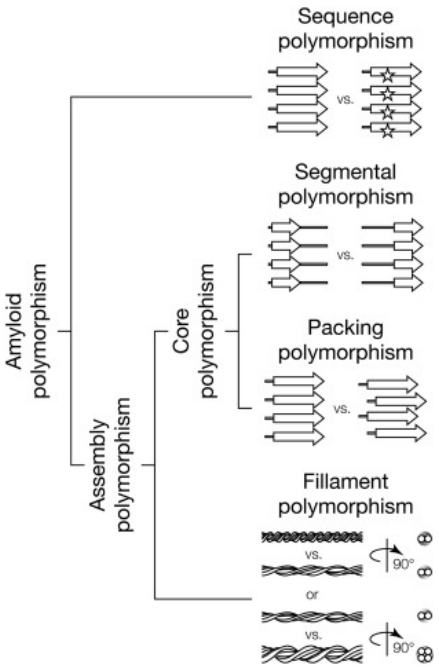

Figure 1.1.3- Schematic illustrations of each type of amyloid polymorphism. *Amyloid polymorphism is classified into sequence polymorphism and assembly polymorphism. Assembly polymorphism is further divided into core polymorphism and filament polymorphism, where core polymorphism is further divided into segmental polymorphism and packing polymorphism. Image from (Lutter et al., 2019).*

1.1.4 Biological consequences of amyloid formation

Research into the conformational, morphological and kinetic properties of amyloid aggregates is steadily increasing due to the urgent need to understand the link between protein misfolding and an increasing number of associated human disorders. Amyloid formation in most prevalent in mammals where common amyloid forming proteins include α-synuclein in Parkinson's disease, amyloid-β and tau in Alzheimer's disease, the huntingtin protein in Huntington's disease, amylin (or islet amyloid polypeptide) in type II diabetes and the prion protein associated with transmissible spongiform encephalopathies (Eisenberg and Jucker, 2012; Knowles et al., 2014. Many of these diseases are strongly linked to ageing, such as Alzheimer's and Parkinson's disease, while others such as type II diabetes are associated with lifestyle. The

ability of amyloid to effectively transition between the soluble and insoluble state allows them to exhibit various biophysical and biological properties, supporting a diversity of functions in almost every kingdom. Such functionality is likely to originate from the highly repetitive structure and tight packing of end-stage fibrils, providing stable storage environments, favourable mechanical properties, and in some cases, active catalytic surfaces for biosynthetic pathways (Arosio et al., 2015). In humans, these include epigenetic switches, scaffolds for melanin formation, and storage of peptide hormones. In fungi, amyloid is a crucial information carrier within the immune system and long-term memory, with further involvement in signalling. In some prokaryotes, Curli and Fap are crucial for biofilm formation and surface adhesion (Greenwald and Riek, 2010; Otzen and Riek, 2019). Despite large differences in their primary sequence, algorithms used to analyse amino acid sequences have revealed that all amyloid forming proteins contain cross-β motifs that are rich in hydrophobic amino acids with high propensity to aggregate and assemble into fibrils (Pawar et al., 2005). Over 50 of these short amyloidogenic peptides have been identified which provide insight into the link between the physiochemical properties of these amino acids, as well as their order in the sequence, and their propensity to form rigid secondary β-structures (Marshall et al., 2014; Lutter et al., 2019).

1.1.5 Definition of prions

Prion is a term coined by Prusiner (1982) to describe a subclass of amyloid that can be transmitted between cells and organisms. These infectious protein particles proliferate in a similar manner to amyloid via template-directed folding of the normal peptide to the prion protein form either spontaneously or by transmission from an already infected cell. All prions propagate via non-Mendelian genetic traits i.e. prions can adopt several different infectious conformations which are generally referred to as prion strains or variants without the need for an accompanying nucleic acid since all the biological information for propagation is encoded

in the amyloid conformation (Griffith, 1967). Conversions are followed by a change in the protein's functional status which may correspond to a loss of normal activity and/or gain of toxic activity. This allows new strain variants to differentially interact with the same host background to cause distinct phenotypes. For example, mammalian prion protein PrP^{C} is an endogenous cell-surface glycoprotein that plays an important role in prion diseases which are collectively termed transmissible spongiform encephalopathies (TSEs) (Manni et al., 2020). Upon conversion to the PrP^{Sc} isoform (Scrapie prion protein), the prion protein may be transmitted to daughter cells from one organism to another via infected meat products, and even across species, infecting both humans and animals. Conversion may occur by chance or spontaneous DNA mutations that encode for a mutant PrP, leading to a loss of function which is unlikely to contribute to prion-associated neurodegeneration because lack of PrP^{C} in knockout mice does not lead to neuronal death (Stohr et al., 2008). Instead, gain of toxic activity is likely to initiate prion disease which can be sporadic, inherited, or acquired, arising from different versions of PrP. In contrast, several prions non-toxic to humans have also been discovered, as well as those with neutral or beneficial effects in fungi (Lutter et al., 2019).

1.1.6 Structure of yeast prions

Commonly studied yeast prion systems include [URE3], [*PSI*], and [*PIN*] of the budding yeast *Saccharomyces cerevisiae*, and the [Het-s] prion system of the filamentous fungus *Podospora anserine.* The best studied yeast prion is [PSI^{+}], which is the prion phenotype associated with Sup35p. Monomeric Sup35 is an essential mRNA translation termination factor (eRF3) but conversion to the infectious state results in loss of solubility and an extension of the C-terminal region which reduces termination activity. The cell consequently exhibits an elevated level of stop codon readthrough, altering the proteome. Therefore PSI^{+} acts as an epigenetic regulator of gene expression (Konno et al., 2020). Wild-type Sup35 protein is composed of three

domains: (1) the N-terminal (N) domain, also known as the prion forming domain because it contains the 5.5 imperfect repeats (PQGGYQQYN), is responsible for the [*PSI*$^{+}$] propagation; (2) the highly charged middle (M) domain which has strong solubilising activity; (3) the essential C-terminal domain which acts in translation termination. Indeed, a prion forming domain (PFD) and a functional domain are common features among all prions (Fig 1.1.6). The PFD of Ure2p, Sup35p, and Rnq1p is a short, intrinsically disordered region of low complexity that is rich in polar uncharged glutamine/asparagine (Q/N) residues. These characteristics of PFDs are likely to drive prion activity but are not the only driving force since the HET-s FPD is more typical of a normal globular protein (Dergalev et al., 2019). Interestingly, the transition to the prion-like conformational state may have evolved in eukaryotes to regulate gene function as suggested by the abundance of PFDs in eukaryotic proteomes relative to prokaryotes. This makes yeast an excellent prion model system to study amyloid formation and propagation, the results from which could be translated to disease context.

Although the self-assembly of prions is not strictly dependent on their amino acid composition, Q/N residues are important prion-forming regions because they encourage the formation of a diffuse network of hydrogen bonds that substantially increase the likelihood of amyloid formation, as well as disorder (Sabate et al., 2015). The short amyloid cores formed by PFDs act as nucleating regions for amyloid assembly, allowing propagation of the prion state. However, since hydrogen bonding between residues is relatively weak, there is a degree of brittleness which potentially increases the rate of fragmentation once amyloid has formed. This in turn generates more short amyloid cores that are capable of transmission, nucleation and propagation between mother and daughter cells (Fernández et al., 2017). The intrinsically disordered nature of specific regions, such as the N and M domains of Sup35NM, is also necessary for the conversion to the cross-β conformation. Moreover, Sup35NM can adopt an

even greater number of distinct amyloid core structures depending on the temperature and surrounding electrolyte species (Konno et al., 2020). However, the existence of functional prions and amyloid structures at physiological conditions requires robust cellular control of aggregation mechanisms. A possible hypothesis which prevents generation of pathogenic amyloid species is that cross-β cores of prions are typically longer than normal and so exhibit reduced propensity to form amyloid by primary nucleation. This allows the protein to remain soluble within the cytoplasm in order to maintain function as required, as well as display varying degrees of brittleness which in turn increase the rate of chaperone-assisted fragmentation and subsequent propagation into non-infected cells (Fernández et al., 2017).

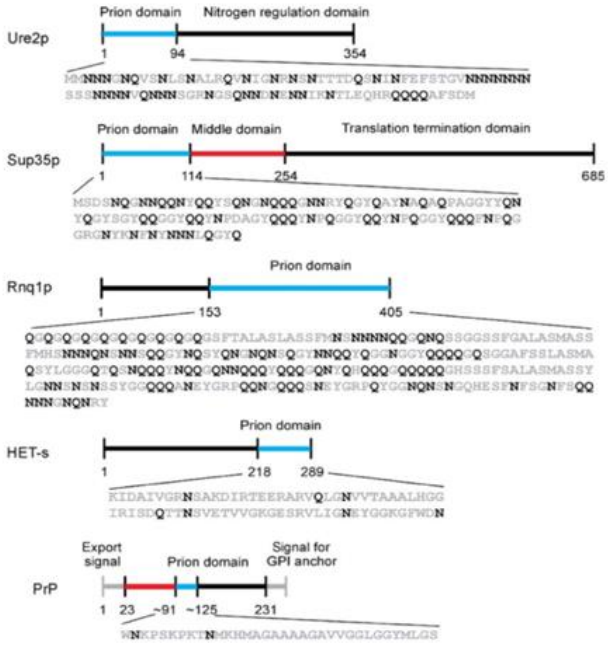

Figure 1.1.6- Structural features of Ure2p, Sup35p, Rnq1p, HET-s, and PrP. *Prion domains are marked in blue and functional domains that code for globular folds in black. The M-domain of Sup35p is likely to act as an extended spacer connecting the prion and functional domains whereas the N-terminal portion of PrP (residues 23–91) is likely to be a signal peptide. It is unclear why three of the five prion domains (Urep, Sup35p and Rnq1p) have unusually high contents of Asn and/or Gln. These residues are shown in black in the prion domain sequences, while other residues are grey. Image from (Baxa et al., 2006).*

1.1.7 Transmissibility of amyloid/prions

The transmissible fold of prions and prion-like proteins is thought to arise from the structural repetitiveness of the amyloid cross-β core. In mammals, the new strain variants are transmitted as infectious diseases but inherited through miosis in fungi. In humans, prion aggregates can spread from cell-to-cell via several mechanisms (Fig 1.1.7) such as via tunnelling nanotubes, trafficking within exomes, glycosylphosphatidylinositol (GPI) painting, membrane budding and transport within vesicles (Sigurdson et al., 2019). As previously established, not all amyloid proteins are transmissible, therefore not all can be considered prions. However, although transmissibility was originally suggested for PrP, there is increasing evidence describing a similar 'prion-like' propagation for amyloid-β (Nussbaum et al., 2012), α-synuclein (Tarutani et al., 2018), huntingtin (Jeon et al., 2016), and tau (Clavaguera et al., 2017), whereby aggregation develops in a particular region of the brain and spreads towards more distal interconnected regions in a stereotypic manner as disease progresses (Wentink et al., 2019). Although these proteins are potentially infectious, they differ from prions because the likelihood of these proteins to transmit between individual humans is relatively low. Cell-to-cell transmission of prion-like proteins only occurs between neighbouring cells whereas prions can be transferred between individuals by ingestion or by access to wounds (Lutter et al., 2019). For example, tau inclusions can be induced in transgenic mice expressing WT human tau by injecting tau-containing human brain extract (Clavaguera et al., 2013). Similarly, the presence of Aβ40, Aβ42, and tau, has also been reported in individuals with Creutzfeldt–Jakob disease (CJD) who had been treated during childhood with human cadaveric pituitary-derived growth hormone (c-hGH) (Purro et al., 2018). This provides evidence for the iatrogenic transmission of Aβ and tau, as well as other prions, possibly due to contaminated surgical equipment used during medical procedures (Laron, 2018). This begs the question why infectivity at the organism level is restricted to prions. To answer this, it's important to

understand the molecular and mechanistic features that define prion-like. Fragmentation during the amyloid/prion lifecycle is a major contributor to the infectivity of amyloid proteins because it generates smaller oligomeric particles of varying size that can be internalised into vesicles and transported across long ranges to be taken up by non-infected cells (Danzer et al., 2012). However, within the highly heterogenous size distribution of fragmented particles generated lies a threshold which prevents transmissibility. The upper threshold particle length for Sup35 seems to be ~200 nm. Particles exceeding this length cannot be transferred by vesicular cell-to-cell transport (Tanaka et al., 2006; Marchante et al., 2017).

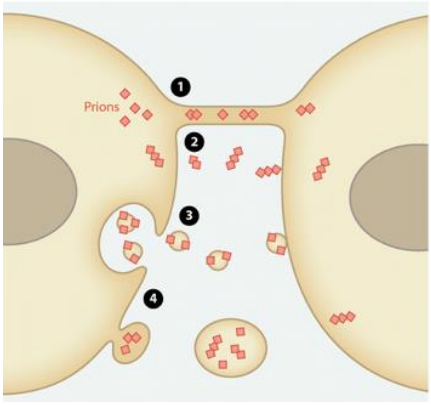

1.1.7- Schematic illustration of the possible pathways for the cell-to-cell transmission of prions. *Prions aggregates can spread via several mechanisms including via (1) tunnelling nanotubes, (2) glycosylphosphatidylinositol (GPI) painting, (3) trafficking within exomes, and (4) membrane budding and transport within vesicles. Image from (Sigurdson et al., 2019).*

1.1.8 The amyloid lifecycle

The amyloid lifecycle is a series of molecular processes which describe the *de novo* formation, growth and propagation of amyloid. In most biological systems, there are at least four key stages that constitute the lifecycle – primary nucleation, elongation, secondary nucleation and fragmentation (Fig 1.1.8) (Lutter et al., 2019). Some systems only exhibit two stage – primary nucleation and elongation. Amyloid self-assembly typically proceeds through nucleated

polymerisation where all steps are dynamic and reversible. In the initial stages, completely or partially misfolded monomeric peptides or proteins undergo spontaneous conversion to the amyloid conformation through a series of thermodynamically unfavourable reactions. The conversion process is remarkably slow but can be accelerated by intrinsic factors such as genetic mutations, truncation and extensions, or by extrinsic factors including denaturing temperatures, denaturing pH conditions, various solvents, metal ions such as Zn^{2+} and Cu^{2+}, membranes and shear forces (Ow and Dunstan, 2014). The amyloid core of these precursor proteins gradually becomes more stable as other peptides aggregate with it to form primary nuclei. These species have an increased propensity for further growth by monomer addition than dissociation into monomers. As a result, this stage of the cycle generates a vast heterogeneous mixture of aggregates of varying β-sheet content and size (Arosio et al., 2015). As the solution becomes supersaturated with aggregated material, nuclei elongate rapidly via template-directed assembly whereby exposed ends of corresponding protofilaments recruit free monomers that adopt the same conformation as those making up the filaments (Lutter et al., 2019). These exposed ends are crucial to elongation because they act as growth active sites for the addition of more peptides which are continuously produced by the host organism (Beal et al., 2020). Thus, increasing the number of fibril ends will significantly increase the rate of elongation, as well as radically shortening these rate-limiting steps of fibril formation.

Secondary nucleation and fragmentation typically occur at a much higher rate than primary nucleation and elongation because they are either not concentration dependent or depend on abundant surfaces of pre-formed amyloid. Secondary nucleation is a type of heterogeneous nucleation where the lateral sides of existing protofilaments or fibrils catalyse the nucleation of new aggregates from the monomeric state (Lutter et al., 2019). Fibrils grow similarly to template elongation but in a manner that results in apparent “branching”. Fragmentation

involves the breaking of fibrils catalysed by chaperones or mechanical stress. This step not only creates more reactive fibril ends for elongation but the size reduction also enables propagation of the amyloid conformation by generating smaller particles that act as seeds. Seeds are post-nucleation species that are capable of growing via templating elongation into protofilaments which subsequently assemble into fibrils. Propagation in this manner is crucial for the infectivity of amyloid, prions and prion-like amyloid, into new cells. Transmissibility of short fibrils is likely to be the primary cause of toxicity in neurodegenerative disease due to their ability to disrupt membranes, whereas long fibril structures are considered relatively inert end products of amyloid assembly (Xue et al., 2009; Beal et al., 2020). Thus, studying the inherent stability of amyloidogenic species towards fragmentation can provide further insight into the biological implications of these structural differences.

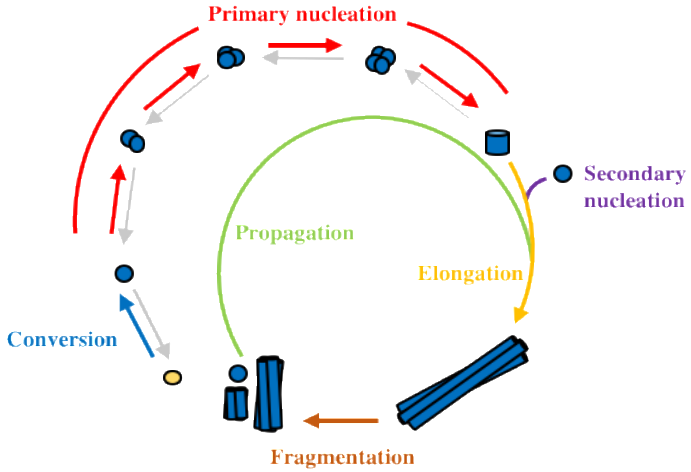

Figure 1.1.8- Schematic illustration of the lifecycle of amyloid/prion assembly via nucleation polymerisation. *The four key stages of the amyloid lifecycle are: (1) primary nucleation from monomers in solution which occurs upon conversion of peptides (yellow circle) to the amyloid state (blue circle); (2) elongation (growth) via monomer addition to existing aggregates whereby new monomers bind to growing fibril ends and adopt the same conformation as those making up the filaments; (3) surface catalysed secondary nucleation from monomers on the lateral side of existing fibrils; (4) fibril fragmentation involving the breaking of fibrils catalysed by chaperones or mechanical stress. Image adapted from (Lutter et al., 2019).*

1.1.9 Amyloid growth kinetics

All amyloid fibrils arise from a common aggregation pathway that is a nucleation dependent process first proposed by Wetlaufer in 1973 (Chiti and Dobson, 2017; Knowles et al., 2014). The precise mechanism is highly complex because it depends on the intrinsic characteristics of the protein as well as the environmental conditions under which aggregation occurs. During a typical amyloid fibril formation reaction, soluble species undergo a nucleation step that results in the formation of oligomeric species which grow via further monomer addition into protofilaments that intertwine to form mature amyloid fibrils. This nucleation-polymerisation reaction is comprised of three characteristic stages (Fig 1.1.9b): (1) a slow, thermodynamically unfavourable nucleation phase; (2) an exponential elongation phase; (3) a saturation period leading to the final plateau phase (Invernizzi et al., 2012). The growth profile of fibril formation displays sigmoidal growth kinetics, suggesting the overall reaction rate is a first-ordered process governed by the concentration of the reacting species. Thus, the self-assembly reaction can be accelerated by the addition of homologous pre-formed fibrils that act as seeds/templates into existing aggregates to promote the transition from the soluble to the aggregated state.

The lag phase is densely populated by native state monomeric proteins or peptides which undergo several conversion steps from their functional soluble state to the amyloid state. When a critical concentration is reached, oligomers begin to form by monomer addition faster than they can dissociate into monomers. These first few elongation events generate larger aggregates called nuclei which have the highest Gibbs free energy along the aggregation pathway (Fig 1.1.9a), therefore act as the energy barrier between soluble monomers and amyloid fibrils (Linse, 2019). The spontaneous, yet relatively slow *de novo* formation of nuclei occurs in a highly thermodynamically unfavourable and reversible manner as described by Oosawa and Asakura (1975), making the nucleation phase the rate-limiting step. As a

consequence of the high energy barrier of primary nucleation, duration of this lag phase is called the lag time because it depends on the probability of a nuclei forming and beginning to elongate when the critical monomer concentration is exceeded. As nuclei form local interactions, elongation occurs via monomer addition into oligomeric intermediates of varying size in a thermodynamically favourable manner, yielding larger, more flexible fibrous structures called protofilaments which twist around each other to provide further strength and stability to the resultant fibrils. Secondary processes begin to dominate the growth phase thereafter as new aggregates are formed at a rate dependent on the concentration of pre-existing fibrils. These secondary processes can be further divided into monomer-independent processes, such as fragmentation, and monomer-dependent processes, such as secondary nucleation. The generation of more active fibril ends by fragmentation and the branching on lateral sides of existing protofilaments or fibrils via secondary nucleation significantly increases the rate and yield of amyloid fibrils. The increase in fibrillar particles displaying active ends demonstrates a direct correlation between fibril fragmentation rates and cytotoxicity (Xue et al., 2009). However, surface catalysed nucleation has also been observed in many disease states to be a key factor in the generation of toxic oligomers (Samuel I A Cohen et al., 2013; Gaspar et al., 2017). These processes mark the beginning of the exponential growth of the total mass of fibrillar species as a function of time. The rate of conversion of amyloidogenic precursor proteins into fibrils is greatest at this point (Arosio et al., 2015). Assembly proceeds in an exponential manner until a final plateau is reached in the equilibrium phase where fibrils are the most prevalent species in the reaction and the monomer concentration reaches a steady state. Resultant fibrils are much more stable, insoluble and rigid compared to monomeric proteins due to a lower free energy exhibited as a result of more extensive backbone hydrogen bonding (Fig 1.1.9a – b). Fibril yield remains constant thus mature fibrils are considered end-

point assemblies. However, dissociation and association events continue to occur even at the final plateau, resulting in molecular recycling within amyloid fibrils (Invernizzi et al., 2012).

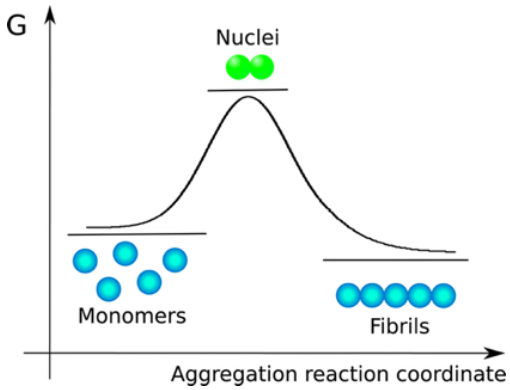

Figure 1.1.9a- Free energy diagram of amyloid fibril formation. *The nucleus is the state with the highest associated free energy, therefore acts as the energy barrier between soluble monomers and amyloid fibrils. The total monomer concentration governs which state dominates at equilibrium. Image from (Arosio et al., 2015).*

Seeding significantly increases the rate of fibril formation because it by-passes the rate-limiting steps dominating the lag phase of fibril formation. The aggregation profile follows a single exponential function where elongation of the fibril becomes the new rate-limiting step since predominant secondary processes are absent (Fig 1.1.9b). This phenomenon is sometimes called templating because once a pre-formed amyloid fibril or "template" is introduced into a solution containing monomeric protein, elongation is initiated by the addition of monomers to the fibril ends which subsequently adopt the cross-β structure, becoming the next templating surfaces. This results in a rapid generation of new fibrils with the same morphology, chirality and local packing of monomers as in the seed (Linse, 2019). Seeds are known to exhibit specificity in amyloid fibrils whereby seeding is most effective when the amyloid sequence of the seed closely resembles that of the targeted amyloid forming protein. For example, turkey lysozyme amyloid seeds accelerate fibril formation of hen egg white lysozyme at a greater rate

than human lysozyme. The lower efficiency of cross-species transmission is also observed in TSEs and between different types of yeast prions (Krebs et al., 2004).

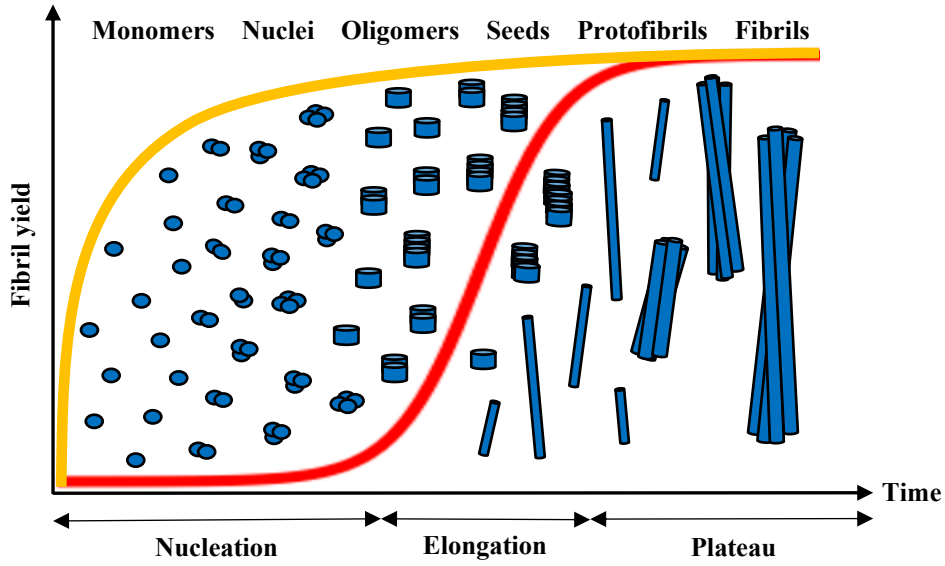

Figure 1.1.9b- Characteristic aggregation curves for the nucleated self-assembly reaction of amyloid fibrils. *The characteristic sigmoidal curve (red), generated using Thioflavin T fluorescence intensity, illustrates three distinct stages to amyloid growth – a lag phase, an exponential phase and a final plateau. The lag phase corresponds to the initial nucleation events where conversion of functional soluble monomeric proteins to the amyloid conformation occurs through thermodynamically unfavourable and reversible protein misfolding events. These precursor proteins aggregate into single nuclei which grow via monomer addition into oligomeric intermediates of varying size until a critical concentration of aggregated material is reached. Oligomers coalesce to yield larger, more fibrous structures called protofilaments in the exponential phase, which assemble into fibrils. Secondary processes such as fragmentation and secondary nucleation begin to dominate, increasing the number and growth rate of fibrils at an exponential rate. A final plateau is reached where fibril growth slows to an eventually stop as the monomer concentration is steadily consumed. Alternatively, the lag phase can be by-passed in the presence of a significant number of seeds where the aggregation profile follows a single exponential function (yellow).*

1.2 Amyloid in Biology

1.2.1 Overview of protein folding

Proteins constitute most of a cell's dry mass. They are not only the cell's building blocks but also execute the majority of the cell's functions including enzymatic activity, transport, chaperones, antibodies, messengers, etc. A protein's function is typically determined by its precise three-dimensional conformation, which in turn is governed by the order of amino acids in the primary sequence of the polypeptide chain, as well as cellular interactions. The unfolded polypeptide chain is subsequently directed towards a stable, low energy state fold called the native state (Fig 1.1.9.2), thus the final fold of a protein is generally one that minimises its free energy (Leopold et al., 1992). Protein conformations are also dynamic and heavily influenced by the surrounding enviroment and chemical properties, generating a large number of degrees of freedom in the polypeptide with an astronomical number of possible conformations. The high degree of conformational flexibility arises from the nature of the peptide bond, while the amino acid sidechains allow a large number of mostly non-covalent interactions. Polypeptides can therefore adopt many different conformations, most of which are thermodynamically unfavourable or non-functional. Therefore, generally only one conformation corresponds to the native state conferring biological activity under physiological conditions. This means, it would take $\sim 10^{11}$ years for a ~100 residue protein to search through all possible conformations until it finds the lowest energy state as suggested by Levinthal's Paradox (1969). This is not possible in a universe the age of 1.4^{10} years, where folding of a typical protein *in vivo* takes 0.1-1000 seconds. Therefore there must be a folding pathway whereby some regions must stabilise first and guide further folding. In the 80s and 90s, experiments to try and define protein folding pathways were inconclusive because folding intermediates were seen to form asynchronously and pathways were indistinct. Several folding models, from classical nucleation–propagation model to the folding funnel model, have since

been proposed to complement experiments towards a better understanding of this complex folding process. The folding funnel model (Fig 1.2.1) is widely adopted whereby protein folding proceeds via multiple unpredictable routes and many intermediate conformations. The broad top of the funnel represents a vast number of different conformational states that exist either in the fully unfolded or stretched form. Proteins subsequently collapse into the folding funnel via different routes available through different intermediates. For proteins that fold without intermediates, the surface of the funnel would be smooth. The narrow bottom of the funnel therefore represents the unique native structure of proteins (Ke et al., 2020).

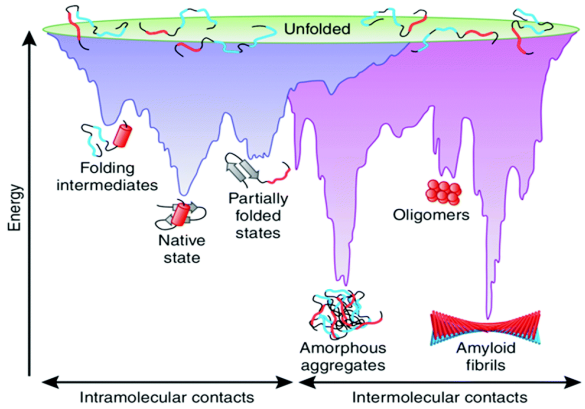

Figure 1.2.1- The energy landscape of protein folding and aggregation. *Proteins in a multitude of different conformational states (the purple surface) 'funnel' to the native state by forming intramolecular contacts. The ruggedness of the free-energy landscape is due to the existence of multiple pathways, each with a distinct pool protein species: monomers, soluble oligomers, and insoluble fibrillar species. The conformations move towards amorphous aggregates or amyloid fibrils via intermolecular contacts (the pink area). Aggregation is normally prevented by molecular chaperones but some misfolded species can rapidly elongate into fibrils via intermolecular. In other pathways, a large number of oligomeric species become trapped in local minima and accumulate. These kinetically trapped conformations must overcome high energy barriers to reach a favourable downhill path. The structural configuration of the oligomers is not optimal for elongation therefore the final fate is transformation into fibrils following slow partial unfolding. Image from (Ke et al., 2020).*

Unfolded or misfolded proteins are highly unstable because their hydrophobic residues and segments of unstructured polypeptide backbone are exposed to the solvent. These are typically buried in the protein's core but if the protein cannot refold quickly enough into its soluble native state, the exposed hydrophobic residues may self-associate into disordered aggregates, driven by hydrophobic forces and interchain hydrogen bonding (Barral et al., 2004). Since this is a common phenomenon, living systems have developed several protective mechanisms that regulate concentrations of potentially pathological aggregates to mitigate cytotoxicity. Under normal physiological conditions, the cell manages these potentially pathological aggregates either by preventing their formation or promoting their removal i.e. by encouraging refolding, sequestering, or degradation of the protein using chaperones, the proteasome, or autophagy, respectively. However, these quality control mechanisms typically decline with age or stress, allowing more aggregation prone species to further cluster into various superstructures which quickly become insoluble. Further growth of these aggregates will be directed towards the lowest free energy state, which often results in an ordered morphology e.g. fibrils that can hinder cellular processes, leading to cellular dysfunction and disease.

1.2.2 Disease association

Approximately 50 disorders associated with amyloid formation have been identified (Pulawski et al., 2012; Chiti and Dobson, 2017). In each case, a specific protein counters the structure-function paradigm by adopting a highly unstable structure which increases its propensity to aggregate either intra- or extracellularly in the peripheral tissues, peripheral organs, or the brain. Accumulation of abnormal protein in large amounts, possibly kilograms, can disrupt intracellular functions, potentially resulting in cell death and tissue damage. The brain is particularly vulnerable to this type of accumulation because it is composed of a highly organised collection of neurones which cannot regenerate unlike somatic cells. Thus, although

intrinsically disordered proteins may accumulate in multiple different tissues, the most severe amyloid pathologies are neurogenerative disorders. The mechanism of cytotoxicity varies depending on the protein involved but in some pathologies it remains unclear, preventing the identification of a clear therapeutic target for each disease. Until recently, mature fibrils were considered to be the cytotoxic species but increasing evidence suggests that end-stage fibrils found in extracellular plaques and inclusion bodies are relatively inert. Instead, the cytotoxic potential of amyloid particles is greatest with decreasing particle length, making non-fibrillar oligomeric species more pathogenic (Xue et al., 2009). Fragmentation of fibrils therefore catalyses the spread of disease pathology. Several mechanisms of cytotoxicity have been proposed on the basis that small, flexible and usually spheroid fibril fragments are responsible for membrane homeostasis disruption in diseases including Alzheimer's. The reduced size and spherical shape increases the propensity to interact with cell membranes, enabling pore formation and abnormal flow of ions which disrupt calcium homeostasis and mitochondrial function, possibly inducing apoptosis (Bucciantini et al., 2004; Demuro et al., 2005).

1.2.2.1 Alzheimer's disease

Alzheimer's disease (AD) is the most common fatal neurodegenerative disorder and the leading cause of dementia worldwide caused by the cortical deposition of fibrillar amyloid-β (Aβ) plaques. The pathological hallmarks of AD, which become more prevalent with advancing age, are: (1) extra-neuronal amyloid plaques primarily composed of insoluble Aβ1-42; (2) intraneuronal neurofibrillary tangles (NFTs) containing hyperphosphorylated species of the tau protein (Giasson et al., 2003; Invernizzi et al., 2012). Accumulation of senile plaques disrupts synaptic function, leading to significant neuronal atrophy and neuronal death starting in the entorhinal cortex and hippocampus, later spreading into different areas in the brain parenchyma (Serrano-Pozo et al., 2011). Patients with AD will therefore typically experience a progressive

decline in cognitive function, spatial orientation, and memory loss (Leifer, 2009). These symptoms usually manifest after the age of 65 in late-onset AD (90-95% of cases), but can also occur in younger individuals with early-onset AD (5-10% of cases) (Penke et al., 2020).

Late-onset AD is strongly associated with the ε4 allele of the apolipoprotein E (ApoE) gene, carrying an estimated 50–70% risk factor. On the other hand, early-onset form is most prevalent in Down Syndrome patients but other genes with the disease-causing mutations identified via linkage analysis are *PSEN1, PSEN2* and *APP* (Owen et al., 2019). *APP* encodes the amyloid precursor protein (APP), an ubiquitously expressed transmembrane protein which facilitates neurite growth, neuronal adhesion, and axonogenesis (Penke et al., 2020). In 1991, John Hardy and David Allsop proposed the amyloid cascade hypothesis which suggests that errors in APP processing leads to the aggregation of Aβ and subsequently Alzheimer's disease. APP in healthy brains is sequentially cleaved by two membrane-bound endoproteases, α- and γ-secretases, generating the non-toxic p3 fragment of Aβ which is essentially $A\beta_{17–42}$. In the amyloidogenic pathway, APP undergoes pathological cleavage by β and γ-secretases respectively, yielding 38–43 amino acid Aβ peptides including amyloidogenic Aβ40, Aβ42 and Aβ43 (Benilova et al., 2012; Selkoe and Hardy, 2016). High levels of trace metals found in amyloid plaques have also spurred a large interest on the role of metals in AD. Zn^{2+} and $Fe^{2+/3+}$ influence α-secretase activity, whereas Cu^{2+} seems to affect β-secretase activity, suggesting their presence is likely to shift APP processing towards the amyloid pathway (Roberts et al., 2012). Fe seems be a critical player in the Aβ aggregation pathway because it impedes the formation of ordered fibrils from amyloidogenic Aβ metastable species (Liu et al., 2011). However, binding of Aβ to oxidized forms of $Fe^{2+/3+}$ or Zn^{2+} produces hydrogen peroxide which contributes to oxidative stress and eventual cell death (Tabner et al., 2002). Moreover, APP mutations at the N-terminal of Aβ influence the rate of Aβ production whereas

mutations at the C-terminal influence the ratio of Aβ peptides with Aβ40 being the most abundant (~80-90%), followed by Aβ42 (~5-10%) (Murphy and LeVine, 2010). These Aβ peptides exhibit different levels of cytotoxicity with longer forms of Aβ being more hydrophobic and fibrillogenic, making Aβ40 the most benign and Aβ43 the most cytotoxic (Benilova et al., 2012). The difference in the aggregation propensity may be due to mutations that occur in the mid-domain of Aβ which lead to slight conformational changes among resulting Aβ peptides with increased tendency to form oligomers and fibrils. For example, both Aβ40 and Aβ42 fibrils form in-register stacks of parallel cross-β subunits because the C-terminal portion Aβ42 is exposed on the surface whereas it is sequestered in the core of Aβ40 (Chuang et al., 2018). Thus, Aβ42 has a higher propensity to aggregate into insoluble Aβ oligomers and later Aβ fibrils that form extracellular senile plaques within the brain.

The lack of structure of Aβ peptides is likely to be the main driving force of its aggregation. Aβ monomers are flexible, random-coil-like structures with partially helical arrangement in apolar solvents but a largely β-sheet structure in neutral aqueous solution (Penke et al., 2020). Although the function remains unclear, Aβ monomers can be found in the cerebrospinal fluid (CSF) of healthy individuals throughout life. Some studies show monomeric Aβ peptides are involved in learning and memory in young mice but their effects remain controversial (Owen et al., 2019). For example, monomeric Aβ at picomolar concentrations consolidates memory but at nanomolar concentrations it inhibits memory (Penke et al., 2020). Increased pathogenicity at high concentrations is likely due to a greater propensity to aggregate largely via hydrophobic collapse into toxic oligomers with decreased conformational freedom. Aβ Trimers have been shown to initiate primary nucleation at a rate dependent on the concentration of monomers, yielding highly ordered non-crystalline and water-insoluble fibrils that are several micrometres long with a width of 10 – 20 nanometres (Penke et al., 2020). Kinetic

studies reveal that once a critical concentration in the order of 10mM of Aβ fibrils has been exceeded, proliferation of Aβ aggregates is predominantly catalysed by a secondary nucleation mechanism where new aggregates are formed from Aβ dimers at an exponential rate dependent on the concentration of existing fibrils (Samuel I. A. Cohen et al., 2013).

There is increasing evidence that amyloid plaques and insoluble fibrillar aggregates of Aβ exhibit relatively low *in vitro* cytotoxicity. Instead, larger aggregates may facilitate the *in vivo* removal of the smaller, more toxic soluble oligomers. In these works, small soluble Aβ oligomers (AβOs) are considered the primary cytotoxic species due to the greater diffusion capability through tissue and into various compartments. The most significant toxicity of AβOs is toward the synapse where both receptor-mediated interactions and non-receptor-mediated membrane interactions have been described. According to the receptor hypothesis, soluble AβOs act as pathogenic ligands at excitatory synapses where they can bind to postsynaptic structures and interact with several putative receptors including PrP, NKAa3, TREM2, NMDA, and EphB2. This in turn stimulates downstream intracellular signalling pathways which inhibit long-term potentiation (LTP), leading to eventual synapse loss (Penke et al., 2020). Since the aforementioned receptors play important roles in mediating AβO cytotoxicity, understanding downstream signalling cascades may provide a clear therapeutic target for AD. Non-receptor membrane cytotoxicity arises from the ion channel hypothesis where AβOs possessing ring-like structures insert themselves into cell membranes and interact with specific membrane lipids to form β-barrel pores that act as aberrant ion channels. The Aβ channels lower the membrane potential, inducing an influx of Ca^{2+} ions into the cell which in turn impairs synaptic function, resulting in apoptosis and atrophy of affected areas of the brain (Kuchibhotla et al., 2008). This effect is believed to be a generic, non-specific mechanism for the cytotoxicity for all oligomeric amyloid species.

1.2.2.2 Tauopathies

Tau is another protein present in the intracellular neurofibrillary tangles (NFTs) within AD brains in the form of aggregated paired helical filaments. Tau is also prevalent in other neurodegenerative diseases such as frontotemporal dementia (FTD), Pick's disease, progressive supranuclear palsy, Parkinson's disease (PD) and dementia with Lewy bodies (Fig 1.2.2b) (Penke et al., 2020). This strongly suggests that tau itself can cause neurodegeneration without the accumulation of Aβ. There are six isoforms of the protein ranging from 352 to 451 amino acids in length, generated by alternative splicing of the human microtubule-associated protein gene (*MAPT*). The isoforms are further divided into two families, namely the three-repeat (3R) and the four-repeat (4R) class which possess three or four microtubule-binding repeat domains (Owen et al., 2019). Like monomeric Aβ, native state tau is intrinsically disordered but a highly soluble multifunctional protein. However, it is best known as a microtubule-associated phosphoprotein located in axons where it facilitates microtubule assembly and motor-driven axonal transport (Mandelkow and Mandelkow, 2012). Despite the predominantly polar composition, the presence of hexapeptide motifs increase tau's propensity to form β-sheets but aggregation is generally avoided under normal physiological conditions as with monomeric Aβ.

Tau can be post-translationally modified under both physiological and pathophysiological conditions. In AD, tau is found to be extensively phosphorylated to a stoichiometry at least three times higher than tau in a normal brain (Penke et al., 2020). Hyperphosphorylation of serine, threonine and tyrosine residues reduces tau's affinity for microtubules, thereby destabilising the cytoskeleton and disrupting axonal transport as tau readily dissociates (Owen et al., 2019). Therefore, a correct ratio of tau isoforms as well as the fine balance between the kinase and phosphatase activity is required for maintaining the biological activity of the tau

protein. Other post-translational modifications such as ubiquitination, nitration, glycation and acetylation, as well as mutations in the *MAPT* gene encoding tau such as P301L, V337M and R406W, also greatly influence tau's tendency to polymerise into tau oligomers and filaments, which eventually deposit as NFTs inside neurons and the extracellular brain space (Penke et al., 2020). Kinetic analysis reveals that aggregation proceeds via monomeric assembly into small oligomers in a first order reaction. A slow structural conversion step follows before fibril formation (Shammas et al., 2015). Smaller, diffusible tau assemblies are more toxic than larger, stable fibrillar structures because at acidic pH, the short amphipathic helices of tau oligomers can interact with membrane lipids to irreversibly form permeable ion channels (Patel et al., 2015). Like Aβ42 channels, tau channels depolarise the membrane, disrupting Ca^{2+} ion homeostasis. However, tau channels are not blocked by Zn^{2+}, possibly due to the large fraction of aggregated tau embedded within the membrane (Patel et al., 2015). It is likely that the presence of tau channels exacerbates the effects of Aβ42 channels in AD brains, as observed in transgenic mice which exhibit more severe symptoms of memory loss at earlier stages of disease progression (Patel et al., 2015).

Although Aβ plaques and NFTs are not the primary cause of cytotoxicity, they are not benign and are likely to co-exist in exchange with their soluble proteinaceous constituents. These large aggregates not only serve as a source of toxic oligomeric species, but they can also physically hinder transport processes within cells, leading to local neuritic dystrophy. Moreover, Aβ oligomers have been shown to promote the re-internalisation of NFTs in the extracellular brain space. Internalised aggregates act as seeds which induce the sequential phosphorylation, misfolding, and aggregation of intracellular tau in a 'prion-like' propagation mechanism (Fig 1.1.7). As well as promoting tau cross-seeding, Aβ also activates GSK3β which in turn triggers hyperphosphorylation of tau, resulting in the dissociation of tau from microtubules and tau

oligomer formation. These findings support the assumption that Aβ precedes the hyperphosphorylation and aggregation of tau. Other cases where Aβ and tau are tightly coupled and mutually reinforcing include maintenance of iron homeostasis of the brain and activation of neuroinflammatory pathways (Penke et al., 2020).

1.2.2.3 Parkinson's Disease

Parkinson's disease (PD) is the second most prevalent neurodegenerative disorder, characterised by the deposition of proteinaceous inclusion bodies called Lewy Bodies (LBs) and Lewy Neurites (LNs) composed of intrinsically disordered α-synuclein (α-syn) (Gaspar et al., 2017). The spread of Lewy pathology across the brain is accelerated in a 'prion-like' manner by α-syn oligomers, attributing to the progressive nature of PD. Aggregation begins in a small portion of neurons in the olfactory bulb and the dorsal motor nucleus of the glossopharyngeal and vagal nerves (Fig 1.2.2a), causing progressive degeneration that spreads as far as the substantia nigra (Owen et al., 2019). Similarly to Aβ and tau, α-syn oligomers confer cytotoxicity by permeabilising cell membranes and inducing apoptosis due to disruption of cell homeostasis. Death of dopaminergic neurons results in lower levels of striatal dopamine, a type of neurotransmitter crucial for initiating and controlling voluntary and involuntary movements. Thus, major symptoms of PD are characterised by bradykinesia where sufferers experience resting tremor, rigidity, and postural instability along with non-motor symptoms that mainly include autonomic dysfunction and cognitive impairment (Lees et al., 2009).

α-Syn is a natively unfolded 140 amino acid long protein encoded by the *SNCA* gene in humans. In healthy individuals, monomeric α-Syn is expressed at high levels at the presynaptic terminal of neurones in the brain, where it is thought to interact with several proteins and phospholipids possibly to facilitate the assembly of the SNARE machinery associated with

vesicular trafficking and release of dopamine (Burre et al., 2010). Smaller amounts of α-syn are also found in the heart, muscles, and other tissues where the function remains unclear. Traditionally, the monomeric form of α-synuclein is considered to be intrinsically disordered but when it is not bound to membranes, it adopts an α-helical enriched conformation. The non-amyloid-β component (NAC) domain of α-syn is a 12 residue stretch of hydrophobic amino acids that is highly prone to forming an amyloid core but it is partially protected by long-range interactions between the C-terminal and the NAC region, and between the N- and C-termini (Owen et al., 2019). However, missense mutations such as A53T, E46K, and A30P in the *SNCA* gene can promote primary nucleation of α-syn but only A53T and E46K have been shown to accelerate fibril formation (Chuang et al., 2018). Moreover, *in vitro* experiments have revealed that aggregation is very sensitive to solution conditions such as temperature, pH, salt concentration, as well as post-translational modifications such as phosphorylation at Ser129 by polo-like kinases, oxidative stress, and the presence of fatty acids (Hashimoto et al., 1999; Karube et al., 2008; Paleologou et al., 2010).

PD is thought to arise when α-syn levels exceed a critical concentration which increases the likelihood of aggregation. The mechanism by which α-Syn fibrils form is described to be a nucleation dependent polymerisation reaction where assemblies grow by the addition of protein monomers to fibril ends. The number and length of fibrils increases by primary nucleation, which is often heterogenous, but new fibrils can also form through the fragmentation of pre-existing fibrils or surface-catalysed secondary nucleation. *In vitro* aggregation assays have revealed that secondary nucleation of monomers on the fibril surface is the dominant secondary process, occurring at mildly acidic conditions (pH < 6) (Buell et al., 2014; Gaspar et al., 2017). α-Syn has a pI of 4.7 therefore it carries a net negative charge at neutral pH (Uversky et al., 2001). Since charge is controlled by pH, it is likely that the pH dependence of secondary

nucleation is due to the electrostatic repulsion between monomers, and between monomers and fibrils. It is established that the newly generated oligomeric species serve as templates for secondary nucleation because the monomers added to growing fibril ends adopt the same conformation as the monomers in the seed. Thus, the structure of resulting fibrils at low seed concentration resembles fibrils formed *de novo* under the same solution conditions. However, at high seed concentration, structural information of seed fibrils is preserved (Peduzzo et al., 2020). Thus, secondary nucleation may be responsible for the propagation of pathology and the progressive nature of PD. Interestingly, α-syn is also reported to co-aggregate with tau. The interaction between the two disease-causing proteins could therefore provide further mechanistic understanding.

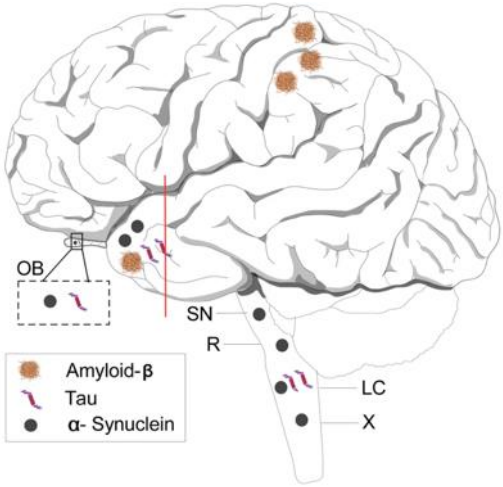

Figure 1.2.2a - Lateral view of the human brain showing the main locations of Aß, tau and α-syn accumulation. *OB (olfactory bulb), SN (substantia nigra), R (raphe nuclei), LC (locus coeruleus), X (nucleus of the vagus nerve). Image from (Ubeda-Bañon et al., 2020).*

1.2.2.4 Transmissible spongiform encephalopathies

Transmissible spongiform encephalopathies (TSEs) are a group of incurable prion diseases that include Creutzfeldt-Jakob Disease (CJD) in humans, Kuru in humans, bovine spongiform encephalopathy (BSE) in cattle, and scrapie in sheep. TSEs are associated with the

amyloidogenic form of the aforementioned mammalian prion protein (PrP^C) encoded by the highly conserved mammalian *PRNP* gene. The soluble cell membrane protein, anchored by a C-terminal glycosylphosphatidyl inositol, is expressed in a large variety of tissues but localised predominantly in neurons where it is thought to be involved in peripheral myelin maintenance, protection against oxidative stress, regulation of embryonic cell adhesion and binding of copper (Invernizzi et al., 2012; Castle and Gill, 2017). In particular, the copper binding activity of PrP^C is demonstrated to be crucial in the maintenance of N-methyl-d-aspartate receptors (NMDARs), which are involved in Aβ mediated neurotoxicity (Sigurdson et al., 2019; Manni et al., 2020). Lesser known roles are observed in the regulation of specific immune processes and in the progression of cancer (Manni et al., 2020). Currently, over 40 mutations have been identified in the PrP gene that give rise to pathology. The majority of these are sporadic with only 15% being heritable (Invernizzi et al., 2012).

At the core of the prion infection mechanism is a large conformational change induced within the PrP^C protein. In the native form, PrP^C is mostly α-helical with less than 3% β-sheet content. However, changes in the environmental may induce the formation of an insoluble PrP^{Sc} form which exhibits approximately 47% β-sheet content. PrP^{Sc} acts as a template for further fibril growth by incorporating monomers and changing them to the same PrP^{Sc} isoform. Prion conversion can occur either on the plasma membrane or within the endocytic pathway via several mechanistic models including the heterodimer model, the cooperative model like an oligomeric enzyme, or nucleation-dependent polymerisation (Stohr et al., 2008). The latter is the most widely accepted model for the conversion of PrP^C to PrP^{Sc}, which involves two phases: nucleation and elongation. Regardless of the origin, all prion conversions are accompanied by an autocatalytic process which changes the proteins functional status, generating new prion strains within a single host species without variation in PrP genotype.

Each strain is associated with a different PrP^{Sc} conformation and pattern of glycosylation which in turn allows a cell or organism to exhibit distinct phenotypic states.

The highly β-sheet rich PrP^{Sc} isoform is particularly susceptible to aggregation and accumulation, especially in the brain and spinal cord where it is most prevalent. Depending on the disease, deposits of aggregated prion protein are variable in size, ranging from small, soluble oligomers to long, thin, unbranched fibrils. Large PrP^{Sc} aggregates are believed to disturb neuronal proteostasis (protein folding, trafficking, and processing), as well as the ubiquitin/proteasome system and autophagy/lysosome pathway (degradation mechanisms for aggregated proteins), further enhancing PrP^{Sc} accumulation (Barmada et al., 2014). There is also increasing evidence that PrP^{Sc} stresses the endoplasmic reticulum by stimulating the unfolded protein response. This cellular stress response disrupts PrP^{C} trafficking and results in translational shutdown of PrP^{C} that consequently weakens the neurons, causes synaptic loss, and subsequent cell death. As in the case of Aβ, α-syn and tau, oligomeric forms of PrP^{Sc} are considered more neurotoxic than larger assemblies. Increasing evidence also reveals cross-talk between PrP^{Sc} and several other disease-associated misfolded proteins including various oligomeric assemblies of Aβ and α-syn (Manni et al., 2020).

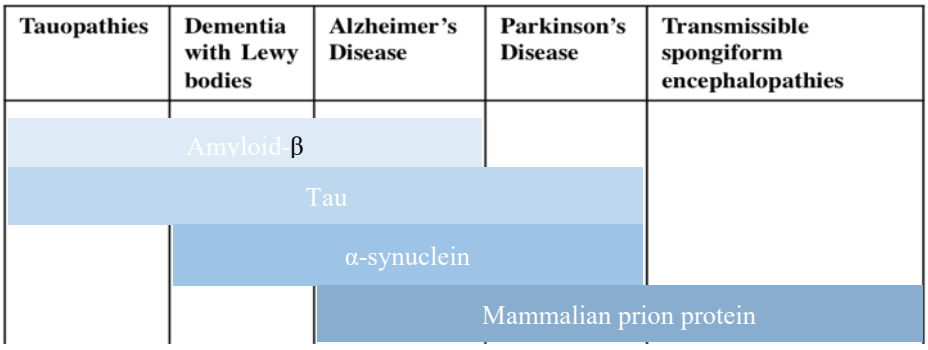

Figure 1.2.2b- Summary of diseases associated with amyloid formation. *The aggregates formed in each neurodegenerative disorder contain one or more amyloid-forming proteins.*

1.2.3 Functional amyloid

1.2.3.1 Pigmentation

In humans, premelanosome protein (PMEL17) is a crucial structural protein that forms amyloid fibrils within melanosomes of melanocytes and retinal pigment epithelial cell (Castle and Gill, 2017). These structures support the melanosome architecture and catalyse melanin synthesis within these organelles. PMEL17 has a repeat domain (RPT) which exhibits high amyloidogenicity but the overall structure retains the non-amyloid form under neutral pH that is achieved by protein compartmentalisation (Invernizzi et al., 2012). PMEL17, initially synthesised as a type 1 integral membrane glycoprotein in the ER, enters the secretory pathway where it is terminally glycosylated in the Golgi apparatus before being navigated into early endosomes at the plasma membrane. These endosomal compartments mature into melanosomes which provide an acidic environment to facilitate amyloid formation (Maji et al., 2009). The RPT is rich in glutamic acid residues which at low pH become deprotonated and charged. These charged residues restrict fibril formation to localised sites of melanasome biogenesis to prevent deleterious interactions with other proteins. The RPT amyloid fibrils stack laterally, forming sheets that accelerate melanin formation by three-fold. Thus, lack of PMEL or mutations in the PMEL gene result in various degrees of hypopigmentation. Proteolytic processing of APP is similar to that of PMEL17 but aggregation lacks regulation by protein compartmentalisation. This makes PMEL function an excellent model for studying the regulation of amyloid formation within the endomembrane system.

1.2.3.2 Storage of proteins and peptide hormones in secretory granules

In mammalian cells, over 30 peptide hormones are stored in the form of amyloid in secretory granules. Secretory proteins and peptide hormones self-assemble into amyloid fibrils within the acidic lumen of the secretory granules of neuroendocrine cells and exocrine cell. At pH 5.5,

these proteins and peptides adopt the amyloid conformation above a critical prohormone concentration during proteolytic processing within the Golgi. Aggregation is further controlled by chemical modifications; the presence of glycosaminoglycans (GAGs) such as heparin can stabilise the amyloid structures (Greenwald and Riek, 2010; Invernizzi et al., 2012). This creates a dense granule core where hormones in the amyloid state can be stored at much higher concentrations for extended periods of time. This allows a slow release of soluble monomeric forms of hormones into the extracellular matrix upon secretion by exocytosis as the granules dissolve when exposed to high extracellular pH. The dissociation rate of each peptide hormone can also be controlled by ion concentration and extracellular chaperones (Maji et al., 2009).

1.2.3.3 Protein storage under stress

Eukaryotic cells exposed to stressors such as extreme temperatures, hypoxia, and acidosis have evolved to alleviate the effects of unfavourable growth conditions by initiating amyloidogenesis to store large quantities of proteins in nuclear amyloid-bodies called A-bodies. This post-translational pathway allows the cell to rapidly and reversibly convert native state proteins to an amyloid-like solid phase in response stressors (Audas et al., 2016). Expression of ribosomal intergenic noncoding RNA (rIGSRNA) in response to hypoxia and heat shock induces multiple proteins displaying the amyloid-converting motif (ACM) to spontaneously enter an amyloid-like insoluble state possibly via interactions between RNA and the arginine/histidine rich region of the ACMs of proteins. This triggers A-body formation in the nucleus into which the amyloid fibrils are stored. The cell then enters a state of dormancy since many of the proteins targeted to A-bodies are involved in cell progression and DNA synthesis. Upon signal termination, the heat-shock chaperone pathway is able to disaggregates A-bodies to restore proteins into their functional native-forms (Jackson and Hewitt, 2017).

1.2.3.4 Synaptic plasticity

Another functional mammalian amyloid protein is human cytoplasmic polyadenylation element binding protein 3 (CPEB3), a prion-like mRNA translation regulator crucial for the maintenance of long-term memory related synaptic plasticity in the hippocampus. CPEB3 has an N-terminal low-complexity domain (LCD) rich in glutamine and asparagine residues. The LCD is orthologous to the tripartite prion domain architecture of *Aplysia* and *Drosophila* CPEB, resembling the Q/N-rich domain of yeast prions (Drisaldi et al., 2015). In the basal state, synaptic CPEB3 is repressed by SUMOylation in hippocampal neurons. This increases protein solubility because a chimeric CPEB3 protein fused to small ubiquitin modifier-2 (SUMO-2) cannot aggregate, therefore cannot activate translation. Following neuronal stimulation, a decrease in SUMOylation and increase in Neurl1-mediated ubiquitination activates CPEB3 to aggregate and assemble into amyloid fibrils. Fibrillar CPEB3 promotes polyadenylation and translation of target mRNAs involved in the consolidation of long-term synaptic connections and memories (Fioriti et al., 2015).

1.2.3.5 Regulated necrosis

Receptor-interacting protein kinase-1 and -3 (RIP1 and RIP3) are essential mediators for TNF-induced programmed necrosis, a major cell death mechanism that is activated in conditions when the apoptotic pathway is compromised or in sterile inflammation. Extracellular stimuli such as tumour necrosis factor (TNF) activate a series of auto- and cross-phosphorylation events between the threonine/serine protein kinases RIPK1 and RIPK3, causing them to co-assemble through their RIP homotypic interaction motif (RHIM) domains into a functional heterodimeric signalling complex known as the necrosome. This amyloid scaffold in turn mediates programmed necrosis by recruiting free RIP3 (Li et al., 2012). Autophosphorylation of RIP3 at Ser227 recruits and further phosphorylates mixed lineage kinase domain-like

(MLKL) at Thr357/Ser358, triggering it to polymerise and translocate to the plasma membrane where it induces membrane rupture (Vanden Berghe et al., 2016).

1.2.3.6 Sexual reproduction

Functional amyloid is naturally abundant in the sperm acrosome where it facilitates the controlled release of proteins during the acrosome reaction. Several peptide fragments of the prostatic acid phosphatase (PAP) enzyme such as PAP 248–286, PAP 85–120, and fragments of semenogelin 1 and 2 (SEM1 and SEM2) form amyloid and amyloid-like fibrils in human seminal fluid, respectively (Jackson and Hewitt, 2017). Although these fibrils were originally identified to promote HIV infection, they also have antimicrobial functions whereby fibrils retain low quality sperm to mediate their clearance by macrophages therefore only allowing healthy sperm to fertilise the oocyte. Thus, low levels of seminal amyloid is associated with reduced male fertility but it may also reduce risk of HIV transmission. The antimicrobial activity of cystatin-related epididymal spermatogenic protein (CRES) fibrils has also been reported, as well as its role in the acrosome reaction and normal lysosomal function in the epididymal (Chuang et al., 2018). Functional amyloid is also observed in insect and fish eggshells which protect the oocyte and developing embryo from harsh external environments.

1.2.3.7 Antimicrobial

Other antimicrobial peptides (AMPs) that are also capable of forming amyloid fibrils include Protegrin-1 (PG-1) and LL-37. Insoluble protegrin is sequestered in Azurophilic granules of neutrophils and macrophages but activated upon infection by bacteria, fungi, or viruses that are enveloped by cell membrane. Azurophilic granules fuse with the pathogen vacuole, allowing protegrins to form pores to permeabilise membranes upon release (Jackson and Hewitt, 2017).

1.2.3.8 Surface adhesion and colony formation

Functional amyloid are most prevalent in bacterial biofilm communities where almost 40% of the species integrate amyloid into the extracellular matrix, increasing cell hydrophobicity and promoting surface attachment for colonisation (Otzen and Riek, 2019). *E. coli* in particular have evolved to exploit the tough, fibrous structure of amyloid proteins Curli and Fap to create a fibrillar extracellular matrix to facilitate surface adhesion and invasion into eukaryotic cells through interactions with host proteins such as fibronectin and the major histocompatibility complex (Chiti and Dobson, 2006; Marshall et al., 2014). The main component of Curl is CsgA, a soluble glycine rich residues with a high propensity to aggregate into amyloid fibrils *in vitro.* Intracellular aggregation would be harmful to the cell therefore amyloid formation occurs extracellularly via the secretory pathway where the CsgG subunit facilitates transport to the cell surface where the CsgF subunit helps membrane-bound CsgB to allow nucleation and subsequent amyloid assembly of CsgA (Invernizzi et al., 2012; Otzen and Riek, 2019). As a result, some bacteria are able to survive in humans treated with antibiotics if bound to biofilms. Both curli and CsgA can also induce production of proinflammatory cytokines in the*E. coli* sepsis reaction. Chaplins are another type of functional amyloid associated with various *Streptomyces* species. Like Curli, Chaplins are secreted extracellularly and found on *the Streptomyces* aerial hyphae to aid spore dispersal, colonisation and attachment of bacteria to surfaces (Invernizzi et al., 2012).

1. 3 Controlling protein misfolding and aggregation

1.3.1 Overview of proteostasis

It is evident that proteins have coevolved with their biological environments to maintain suitable concentrations of functional of amyloid necessary for life and limit the formation and accumulation of cytotoxic species. The regulatory systems associated with protein homeostasis

are collectively termed proteostasis, which comprises a vast network ranging from cell compartmentalisation to the regulation of protein synthesis, proper folding, and degradation (Fig 1.3.1). Molecular chaperones are important components of this network as they form functional complexes with each other and numerous co-chaperones to assist in *de novo* protein folding as well as other fundamental cellular processes such as the unfolded protein response (UPR), protein compartmentalisation, chaperone-mediated autophagy (CMA), and the ubiquitin-proteasome system (UPS) (Fig 1.3.1). Protein aggregates may arise from the failure of such protective mechanisms to refold or degrade misfolded species in a timely manner, leading to a widespread loss of protein homeostasis and cellular dysfunction.

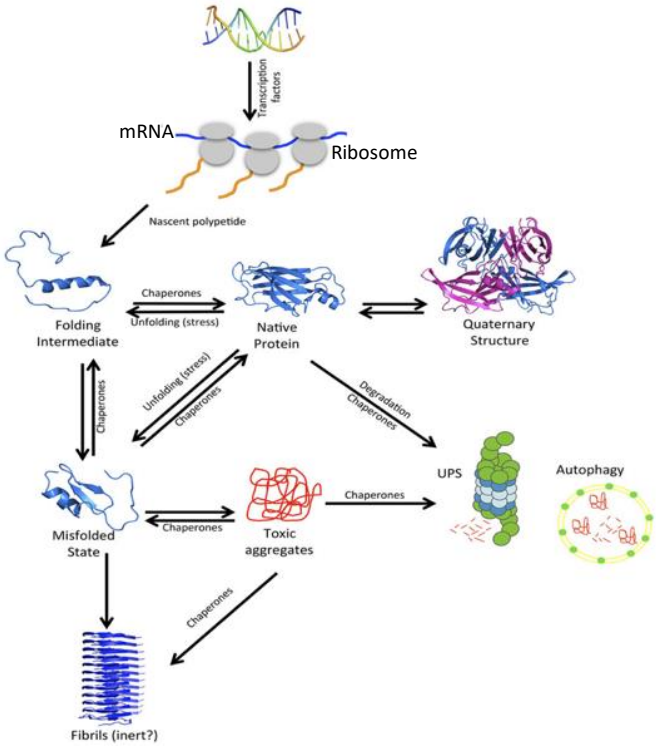

Figure 1.3.1- Overview of the proteostasis network comprising of the ribosome, chaperones, autophagy and lysosomal targeting. *Proteins can adopt many different conformational states following their synthesis at the ribosome. The proteostasis network ensures proteins are in the right state at the right time and in the right place to achieve their final functional native 3D structure. Imbalances in proteostasis leads to protein misfolding and aggregation, resulting in widespread loss of protein homeostasis and disease. Image from (Pallarès and Ventura, 2016).*

1.3.2 Chaperones

1.3.2.1 The Hsp70/Hsp40 system

Protein misfolding is most common during translation at the ribosome in protein synthesis. Spontaneous genetic mutations, splicing errors, ribosome stalling, and premature termination are some examples of transcriptional and translational errors that may increase the likelihood of misfolding of the nascent polypeptide. Errors in post-translational modifications due to mislocalisation of the polypeptide, molecular crowding, or age-related decline in cellular functions can also be detrimental (Chaari, 2019). As a result, ribosomes are a primary target for molecular chaperones, in particular, members of the heat-shock protein 70 (Hsp70) family which act both under normal physiological and stress conditions. Hsp70 is the most highly conserved group of molecular chaperones that are ubiquitous in the bacterial, archaeal and eukaryotic cytosol, as well as in the eukaryotic nucleus, mitochondria, chloroplasts and endoplasmic reticulum (ER). Hsp70 facilitates *de novo* protein folding as soon as a nascent chain longer than 60 amino acids emerges from the ribosome exit channel (Barral et al., 2004). Like many other cytosolic chaperones, Hsp70 functions in complex with co-chaperones such as Hsp40 to modulate its ATPase activity and target its function, which is to recognise exposed segments of hydrophobic amino acids in the nascent peptide chain and promote the proper formation of noncovalent interactions that lead to the native folded state. Via ATP-regulated binding, misfolded species are subsequently transported by Hsp40 to Hsp70 for refolding or degradation. This supports the action of the Hsp70/40 complex to inhibit the early steps of Aβ42, α-Syn and polyQ-based amyloid aggregation in an ATP-dependent manner by solubilising these oligomers, converting them to non-toxic forms. The action of human Hsp70 (Hsc70) has been demonstrated in neuroglioma cells, where MAL3-101 effectively inhibits Hsp70, increasing α-Syn induced cytotoxicity. However, function can be restored by the co-chaperone for Hsp70, 115-7c (Chuang et al., 2018). Moreover, Hsc70 can transfer htt_{ex1}

oligomers into inclusion bodies (Owen et al., 2019). Yeast prions heavily rely on chaperones such as Hsp70 to maintain the correct size and number of fibril seeds for prion propagation. There are two subclasses of *Saccharomyces cerevisiae* Hsp70, namely Ssa1 and Ssb1/2, which have opposing effects on the Sup35 aggregate load and [*PSI*$^{+}$] maintenance by enhancing and suppressing prion formation, respectively. Ssb inhibits formation of [*PSI*$^{+}$] in [*psi*$^{-}$] cells by enhancing the curing efficiency of excess Hsp104 and either promoting the refolding of [*PSI*$^{+}$] into the non-prion conformation or targeting misfolded proteins for degradation. Ssa on the other hand is thought to stabilise the prion form, increasing *de novo* formation of [*PSI*$^{+}$] as well as the amount of monomeric Sup35 protein by antagonising [*PSI*$^{+}$] curing and solubilisation of Sup35 aggregates (Greenwald and Riek, 2010). This has been demonstrated in [*PSI*$^{+}$] cultures that overproduce the Sup35 protein where the proportion of [*psi*$^{-}$] cells increases with excess Ssa. Hsp70 has also been shown to increase the lag phase of prion protein Ure2p fibril formation in yeast (Knowles et al., 2014).

1.3.2.2 The Hsp90 system

Members of the Hsp90 family act downstream of the Hsp70/Hsp40 system and play a key role in regulating protein structure by recognising the substrates in a conformation close to the native state. Hsp90 is the most abundant molecular chaperone in the cell but unlike Hsp70, Hsp90 is localised to the cytosol and the ER and its function is limited to proteins involved in signal-transduction (steroid hormone receptors and protooncogenic kinases) and cell-cycle and transcriptional regulators under normal physiological (Chaari, 2019). Following substrate loading by an Hsp70-dependent mechanism, Hsp90 assists in the folding and subsequent release of the native protein upon ATP hydrolysis. However, Hsp90 reduces its substrate selectivity under stress conditions and acts as a storage compartment for unfolded proteins to be refolded and assembled by other chaperones (Barral et al., 2004). Similarly to Hsp70/40,

Hsp90 also inhibits early aggregation $A\beta_{42}$, as well as assembly of α-Syn, by increasing the lag time during the nucleation phase. These chaperones play a major role especially in PD since they are commonly found localised in Lewy bodies. As a result, they are of great interest because understanding their function may help combat protein aggregation linked to fatal neurodegenerative diseases (Kilpatrick et al., 2013; Owen et al., 2019).

1.3.2.3 Small heat shock proteins and clusterin

Small heat shock proteins (sHsps) are an ubiquitous class of ATP-independent chaperones that are activated in response to oxidative stress and high temperatures prior to refolding attempts by ATP-dependent chaperone complexes. sHsps are most prevalent in the nervous system where they bind partially unfolded polypeptides with high affinity without subtract specificity. The interaction stabilises the polypeptides by protecting their exposed hydrophobic surface from further misfolding or aggregation (Chaari, 2019). sHsps such as sHsp20, Hsp27 and α-β-crystallin have been shown to protect against polyQ and Aβ mediated cytotoxicity by preventing aggregation of $A\beta_{40}$ but not $A\beta_{42}$ despite binding to both forms (Barral et al., 2004). Clusterin is another chaperone whose activity is similar to, but more potent than that of intracellular sHsps. This highly glycosylated heterodimeric chaperone binds to exposed hydrophobic regions of transiently formed prefibrillar species in the extracellular matrix to form soluble, high-molecular weight complexes (Barral et al., 2004). Like sHsps, clusterin is upregulated under stress, aging, tissue injury and diseases such as AD, Down's syndrome and T2DM. Although both clusterin and sHsps can bind to a broad range of proteins, in the context of AD, they are more effective in supressing the nucleation stage of amyloid formation to inhibit the subsequent growth of prefibrillar species rather than inhibiting fibril elongation or disrupting mature fibrils. This same applies with the action of α2-macroglobulin (α2M), another extracellular chaperone of considerable relevance. α2M is not as effective as clusterin

but it is crucial for the clearance of Aβ *in vitro* due to its 2-3 order higher concentration in human blood plasma and CSF compared to that of clusterin (Owen et al., 2019).

1.3.2.4 Disaggregases

Another family of chaperones called disaggregases are also able to solubilise aggregate protein oligomers and amyloid fibrils to their functional native states. *Saccharomyces cerevisiae* Hsp104 is a highly conserved and most effective disaggregase of the AAA+ ATPase family (Mack and Shorter, 2016). Six protomers assemble to form an offset homo-hexameric barrel with a central pore through which mature amyloid fibrils of α-Syn, polyQ, tau, Aβ, PrP and amylin, as well as prions formed by Sup35, Ure2, and Rnq1 are translocated and subsequently dissolved via ATP hydrolysis (Chuang et al., 2018). Interestingly, the Sup35 and Ure2 fragments formed by Hsp104 have been shown to form seeds that could enhance both *in vitro* amyloid formation and infectivity (Chaari, 2019). Metazoa lack Hsp104, instead, the protein-disaggregase machinery is composed of Hsp110, Hsp70, Hsp40, and sHsps which act synergistically to dissolve aggregates of Sup35, α-Syn, and polyQ by depolymerising amyloid fibrils from their ends (Torrente and Shorter, 2013). Interestingly, yeast Hsp104 can interact with the Metazoan Hsp70/Hsp40 disaggregase machinery to eliminate cytotoxicity conferred by polyQ and α-Syn in flies, worms, and rodents (Chuang et al., 2018; Owen et al., 2019). The ability of the metazoan protein-disaggregase machinery to be enhanced by exogenous disaggregases opens several therapeutic opportunities to upregulate amyloid degradation.

1.3.2.5 Chaperonins

Chaperonins are a family of ~60 kDa chaperones composed of monomers that form complexes arranged as two stacked heptameric rings (Fig 1.3.2.5). These double-ring complexes occur in two subgroups. Group I chaperonin GroEL/Hsp60 and its cofactor GroES/Hsp10 is found in

bacteria, chloroplasts, and mitochondria. Group II chaperonin TRiC/CCT is found in the cytosol of eukaryotes and Archaea (Barral et al., 2004; Mack and Shorter, 2016). Both chaperonins inhibit Aβ1-42 aggregation but the effect of TRiC/CCT is more significant. TRiC/CCT is a key example of a single chaperone that can interact with different amyloid proteins via different domains and mechanisms while in an open state. For example, the CCT_{ζ} and CCT_{γ} subunits interact with the NAC component of α-Syn, whereas the CCT_{α} subunit binds to the amphipathic helix of the htt_{ex1} monomer (Owen et al., 2019). Upon binding of non-native polypeptide chains via hydrophobic interactions, the additional helical component of TRiC/CCT acts as a lid for the central cavity in each ring, trapping the protein therein. A major conformational change follows where the central cavity enlarges and shifts its surface to a more hydrophilic lining (Mack and Shorter, 2016). Within this so-called Anfinsen cage, a variety of proteins can fold via an ATP-dependent mechanism in a carefully controlled environment with infinite dilution to avoid undesirable interactions by other molecules and prevent the peptide from entering into kinetically trapped states. Following ATP hydrolysis and binding of ATP to the opposite ring, the substrate is released from the chaperonin but may require several more folding cycles for complete folding. This highly conserved mechanism facilitates the folding of approximately 10% of the eukaryotic proteome (Horwich, 2011).

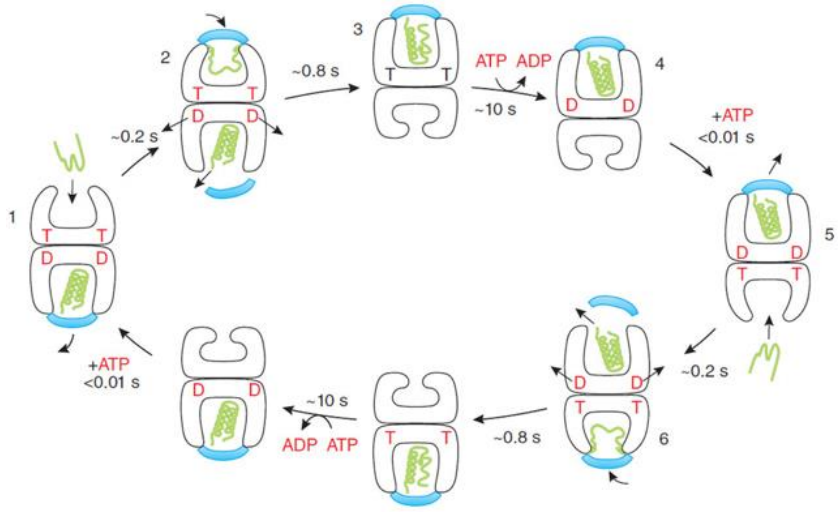

Figure 1.3.2.5- GroEL-GroES reaction cycle. *The cycle is directed via binding and hydrolysis of ATP in respective GroEL rings (T = ATP; D = ADP). (1) non-native polypeptide binds to the ATP-bound GroES ring by hydrophobic interactions; (2) GroEL undergoes major conformational changes where elongation and opening of the ring cavity occurs and the hydrophobic binding surface replaced by hydrophilic surface; (3) protein encapsulated within the chamber is released and encouraged to fold upon ATP hydrolysis; (4) ATP affinity for GroES relaxed but increased for the trans domain for non-native protein; (5) non-native protein binds to the bottom ring followed by ATP; (6) dissociation of GroES, ADP, and the protein which may be folded, in an intermediate state committed to folding or unfolded. A new folding cycle now commences on the trans ring. Image from (Horwich, 2011).*

1.3.3 Degradation

1.3.3.1 Ubiquitin-proteasome system (UPS)

Chaperones are also involved in the regulation of intracellular degradation of misfolded proteins that cannot be refolded. Such species are efficiently removed via two major intracellular degradation pathways - the ubiquitin-proteasome system (UPS and autophagy (Fig 1.3.3). Both systems rely on disaggregases such as Hsp70 in combination with Hsp110 and Hsp40 which target unfolded proteins to the proteasome or lysosome for degradation when

folding is unsuccessful (Ciechanover and Kwon, 2015b). UPS is the much more targeted degradation mechanism that is responsible for the clearance of short-lived proteins. Many natively unfolded or intrinsically disordered proteins including Tau and α-synuclein are targeted by the UPS, where Ub-conjugated proteins are ubiquitinated by Hsp70-associated ubiquitin ligases such as CHIP, and delivered to the proteasome for degradation by shuttles such as UBQLN2 (Chuang et al., 2018). Interestingly, tau-fibrils have been reported to inhibit the ATPase and proteolytic activities of the proteasome but function can be restored in early-stage tauopathy by small-molecule Rolipram which increases cAMP–PKA signalling. Aβ expression is also reported to reduce proteolytic activity of the proteasome in diseased tissue. This in turn may exacerbate cytotoxicity in aggregation diseases (Barral et al., 2004). The greatest risk factor is aging, which leads to reduced capacity to degrade misfolded species in degenerating brains as demonstrated by several studies (Ciechanover and Kwon, 2015b).

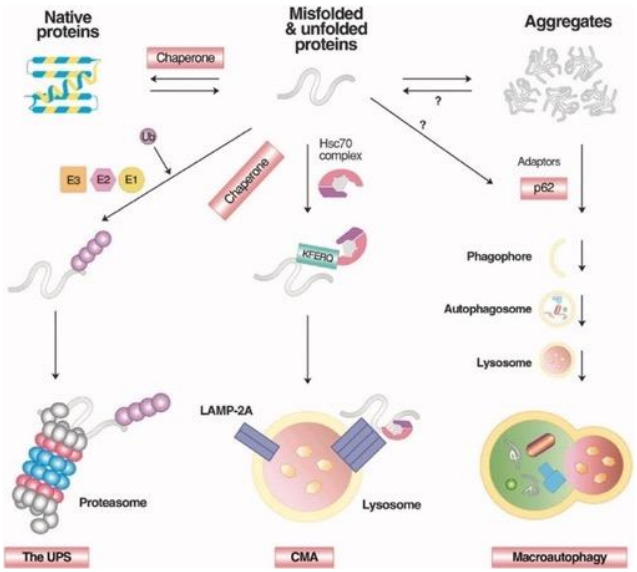

Figure 1.3.3- Amyloid degradation by various cellular proteolytic pathways. *The Hsc70 disaggregase complex binds to unfolded polypeptides via specific motifs to stabilise and shift the population towards the folded state. Proteins that cannot refold are targeted to the proteasome, lysosome, or macroautophagy for degradation. Image from (Ciechanover and Kwon, 2015b).*

1.3.3.2 Autophagy

Autophagy is another catabolic process but it is involved in the clearance of excess long-lived proteins and defective organelles. There are three types of autophagy - macroautophagy, microautophagy, and chaperone-mediated autophagy (CMA). Approximately 30% of cytosolic proteins are degraded via CMA (Fig 1.3.3). This is a selective proteolytic system where only proteins expressing the KFERQ pentapeptide are recognised by Hsc70 and delivered to lysosomes through the lysosome-associated membrane protein type 2A (LAMP-2A) for degradation by lysosomal hydrolases. In degenerating neurons, CMA is activated to remove aggregates of TDP-43, α-Syn, polyQ-Htt, tau, and Aβ (Ciechanover and Kwon, 2015a). In microautophagy, misfolded proteins are directly engulfed by lysosomal membranes, whereas in macroautophagy, misfolded proteins and organelles are encased within an autophagosome and subsequently digested by lysosomal hydrolases upon fusion with lysosome. In neurons, misfolded proteins are packaged in autophagosomes at the distal exon. The autophagosomes subsequently bind to negatively regulated kinesin motors to allow retrograde transport by dynein-kinesin motors along microtubules towards the soma that is rich in lysosomes for degradation (Fig 1.3.3.2). Upon arrival, autophagosomes mature into autolysosomes via fusion with lysosomes (Ciechanover and Kwon, 2015b; Chuang et al., 2018). Proliferating cells are more resistant to oligomer induced cytotoxicity because they can transfer pathogenic species to daughter cells via mitosis. However, the task of clearing such substances becomes increasingly difficult in mature cells due to the downregulation of autophagy proteins (beclin-1, Atg5, and Atg7) with age, attributing to the late onset of most neurodegenerative diseases. In contrast, formation of autophagosome is upregulated in AD, possibly due to an increase in reactive oxygen species (ROS) production and phosphoinositide 3-kinase (PI3K) activity by Aβ, which is accompanied by increased levels of the autophagy initiation proteins beclin-1 and the Atg5-Atg12 complex (Wong and Holzbaur, 2014). In contrast, accumulation of α-Syn in

PD inhibits Rab1a, resulting in Atg9 mislocalisation and defective autophagosome formation (Lipinski et al., 2010). In HD however, autophagosome formation remains unaltered along the exon but inadequate lysosome acidification by presenilin 1 (PS1) can cause neurodegeneration in HD and AD (Wong and Holzbaur, 2015).

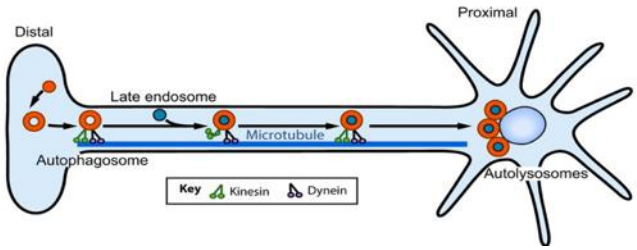

Figure 1.3.3.2- Autophagosome dynamics in neurodegeneration. *Autophagosomes formed in the distal axon of neurons subsequently fuse with late endosomes as they are retrogradely transported along microtubules by dynein-kinesin motors toward the soma. At the soma, autophagosomes mature into autolysosomes via fusion with lysosomes for degradation. Image from (Chuang et al., 2018).*

1.3.3.3 Astrocytes and microglia

Concentrations of Aβ may increase either due to over production as observed in familial AD, or impaired amyloid clearance mechanisms as in sporadic AD. Typically, microglia clear excess soluble Aβ peptides by P2Y4 receptor mediated pinocytosis and phagocytosis (Thal, 2012). There is also evidence of astrocytes mediating Aβ clearance via several mechanisms but they mainly perform their neuro-supportive role in the brain parenchyma (Nagele et al., 2004). However, *in vitro* studies suggest that familial AD mutations increase the sensitivity of astrocytes and the inflammatory response which could result in the death of the astrocytes surrounding the plaques and formation of astrocyte-derived amyloid plaques. Aβ-astrocytes further contribute to the neuroinflammation observed in cerebral amyloid angiopathy (CAA) where they induce inflammatory cytokines, metabolising enzymes neprilysin or insulysin, and reactive oxygen species to combat the accumulation of amyloid plaques along the walls of the

cerebral vasculature (arteries, arterioles and less often veins and capillaries of the nervous system) (Batarseh et al., 2016). As a result, chronic activation of AD astrocytes in response to elevated Aβ levels is more harmful than supportive, thus, a novel therapeutic approach to prevent inflammation-mediated cell death is to reduce astrocyte activation. Since Hsp70 has been identified as a key player in protein disaggregation, degradation, and ubiquitylation, upregulation of Hsp70 may compensate for the age and disease related decline in chaperone expression, autophagy, and proteasome activity simultaneously (Kilpatrick et al., 2013; Mack and Shorter, 2016; Torrente and Shorter, 2013).

1.4 Species and processes of the amyloid lifecycle

1.4.1 Amyloid species

All four stages of the amyloid lifecycle occur simultaneously during the course of the aggregation process, albeit at different rates as governed by rate constants and by the concentration of reacting species. Primary nucleation and elongation are considered primary pathways because they involve the conversion of monomers to larger aggregates. Secondary nucleation and fibril fragmentation are secondary pathways because they generate more reactive fibril ends for elongation (Fig 1.4.1). This creates a highly heterogenous mixture of species, the most prevalent being monomers or fibrils. The dominating species during the lag phase are monomers, whereas fibrils are most prevalent at the final plateau. However, their concentrations become similar during the elongation phase (Arosio et al., 2015). Monomers are the smallest single peptide units that may exist free in solution or as complexes with other monomers in aggregates in a folded or unfolded state. An assembly comprising of multiple monomers is defined as an aggregate. Types of aggregates include nuclei, oligomers, protofilaments, protofibrils, and fibrils. Each one is defined by size, growth rate, degree of order in structure, distinct surface properties, and level of toxicity (Dear et al., 2020).

Oligomers are described as small multimeric aggregate species comprising of 2 – 30 monomers, each with a high free energy. This increases the likelihood of these oligomers to dissociate into their component monomers. As a result, oligomers elongate significantly slower than amyloid fibrils, which are the largest of aggregates containing tens of thousands of monomers. During nucleated polymerisation, oligomers are constantly being formed both by primary and secondary nucleation processes. Oligomers containing the same kind of monomers have a structure that promotes the formation of critical nuclei which can template their fold onto other monomers to elongate faster than dissociation back into monomers. Elongation of these nuclei proceeds via monomer addition to their exposed ends to yield protofilaments which are threadlike structures comprised of a single layer of peptides that associate by β-sheet formation to generate the cross-β structure. Two or more protofilaments can intertwine to form a linear filamentous fibril which becomes the next dominating species. Secondary nucleation subsequently becomes the main process that rapidly generates new oligomers.

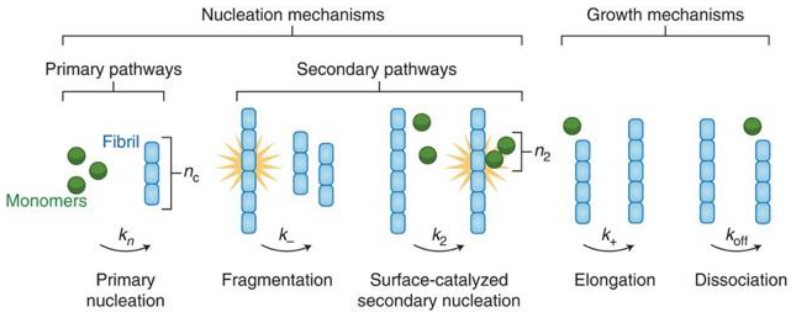

Figure 1.4.1- Primary and secondary pathways of the amyloid lifecycle and associated rate constants. *The microscopic steps in each mechanisms are classified on the basis of their dependence (secondary pathways) or lack of dependence (primary pathways) on the aggregate population. Primary nucleation and elongation are considered primary pathways because they involve the conversion of monomers to larger aggregates. Secondary nucleation and fibril fragmentation are secondary pathways because they generate more reactive fibril ends for elongation.* k_n, k_-, k_+, *and* k_{off} *represent rate constants, and* n_c *and* n_2 *represent the reaction orders of primary and secondary nucleation. Image from (Dobson et al., 2020).*

Another distinguishing factor between oligomers is their relative contribution to the formation of fibrils. “on-pathway” oligomers are intermediate species that react onward to form fibrils, whereas species produced in side-reactions are termed “off-pathway”. In systems where secondary nucleation dominates, all oligomers are fully on pathway, as in the case of Aβ42 oligomers in AD. Although AβOs dissociate rapidly into monomers, they are rapidly reformed therefore have a large contribution to the fibril formation. In conditions where secondary nucleation is suppressed, two kinds of α-synuclein oligomers may co-exist. Both are fully on pathway where one type is formed from monomers and then converts the other type, which in turn converts to fibrils (Dear et al., 2020).

Table 1.4- *Terminology used to describe the species and processes of the amyloid lifecycle.*

Term	Definition
Aggregate	An assembly comprising of two or more monomers *i.e.* dimers, trimers, and higher order assemblies.
Elongation	The action of fibril growth in a direction that is parallel to the main axis fibril whereby protein or peptide monomers are added to exposed fibril ends.
Fibril	A linear filamentous aggregate with a repetitive cross-beta core structure, formed by two or more intertwined protofilaments.
Fibril end	The active site which mediates fibril elongation by the addition of protein or peptide monomers.
Fibril fragmentation	Division of fibrils induced by mechanical or chemical perturbations, thermal stress, or chaperone catalysis.
Monomer	A single protein or peptide chain that exists free in solution or in complex with other monomers in aggregates.

Nuclei	The smallest aggregate species with the highest Gibbs free energy along the aggregation pathway, capable of further growth by monomer addition faster than dissociation of existing monomers.
Oligomer	2-100-mer protein or peptide aggregate that is heterogenous and transient in nature, generated by the first few elongation events of nuclei without any reference to its structure.
Primary nucleation	*De novo* formation of amyloid fibrils via homogeneous or heterogenous nucleation of soluble monomers either in solution or at surfaces or interfaces, respectively.
Protofilament	A single elongated amyloid filament possessing the characteristic cross-β structure where a single layer of peptides associate by β-sheet formation.
Protofibril	A less ordered curve-linear fibril that is structurally comparable to oligomers.
Secondary nucleation	A sub-division of heterogenous nucleation where nucleation of monomers occurs on the surface of existing fibrils.
Secondary processes	Fibril fragmentation and secondary surface nucleation resulting in the accelerated rate of the exponential growth phase of amyloid assembly and elongation growth at fibril ends.
Seed	Post-nucleation species capable of increasing the rate of amyloid assembly either by accelerating fibril growth by elongation or inducing secondary nucleation.

1.4.2 Primary nucleation

Primary nucleation, or *de novo* formation, is the first stage of the amyloid lifecycle which involves the formation of a critical nucleus from free monomers in the amyloid state. Amyloidogenic peptides typically exist in a native aqueous solution phase therefore the initial aggregation process requires partial unfolding of these monomers to assist the transition to the 'solid phase' represented by amyloid fibrils in latter stages of the aggregation. Monomers with exposed amyloidogenic regions have increased propensity to form an amyloid core in an unfavourable and reversible manner but the core can become more stable as other peptide in the same amyloid state aggregate with it. These initial steps of primary nucleation involve monomers only therefore other processes are completely suppressed (Arosio et al., 2015). This confirms primary nucleation is necessary to start the cycle which can proceed either in homogeneous nucleation where nucleation occurs in bulk solution or heterogenous nucleation where nucleation occurs on foreign surfaces or at interfaces (Lutter et al., 2019). Heterogenous nucleation is likely to dominate since biological systems are densely populated with surfaces of different composition and properties. Foreign surfaces such as nanoparticles are shown to have profound effects on aggregation kinetics by either catalysing or inhibiting aggregation, resulting in shortening or lengthening of the lag phase (Arosio et al., 2015). Nuclei begin to form in this presaturated solution of monomers very early on in the lag phase at a constant rate. The rate becomes more significant as monomer is consumed as evident by the growth of aggregates at the end of the lag phase.

1.4.3 Elongation

The system leaves the lag phase and enters the elongation phase once a critical oligomer size is reached. During the elongation phase, nuclei grow at an exponential rate into fibrils by sequestering monomers (Owen et al., 2019). Growth of nuclei occurs either by templated elongation where free monomers are converted to the amyloid state and added to growing

filament ends (Jarrett and Lansbury, 1993), or via assembly of oligomers where nuclei grow into helical oligomers that associate to form a filament (Vestergaard et al., 2007). The subunits of these intermediate species possess a cross-β core which is stabilised by further elongation at a rate much faster than that observed for oligomers in the lag phase. Elongation is reversible but detachment of monomers is highly unfavourable due to the highly stable fibril structure. As a result, conversion of precursor molecules into prefibrillar fibrils is greatest at this point of the reaction (Arosio et al., 2015). Structural polymorphisms begin to arise as 2-6 protofilaments twist around each other to form fibrils. Further growth of these fibrils can occur at exposed ends, creating a more ordered and stable fibril arrangement. Mature fibrils observed in an end-stage *in vitro* assembly reaction are usually long and straight assemblies but there is no formal length, width or twist definition because fibrils with more flexible traits have also been observed to circularise and grow into loops (Lutter et al., 2019).

1.4.4 Secondary nucleation

Secondary nucleation is a monomer-dependent secondary process where nucleus formation is catalysed on lateral surfaces of existing fibrils composed of the same kind of monomers. The new nuclei formed at these binding sites along fibrils subsequently detach and grow via templated elongation in the same linear fashion as the protofilaments making up the parent fibrils, thereby preventing branching (Linse, 2019). Since this is strictly a fibril-dependent process, it is regarded as a type of heterogeneous nucleation. Like heterogeneous primary nucleation, secondary nucleation also accelerates the aggregation process therefore shares some similarities on an energetic level. Although both processes provide active sites for nucleation events, differences arise from the types of surfaces involved. For example, heterogeneous primary nucleation occurs in the presence of foreign surfaces provided by phospholipid membranes, nanoparticles, at the air-water interface, or any surfaces present in

the system (Arosio et al., 2015; Linse, 2019). Secondary nucleation however requires preformed aggregates of the same kind of monomers, therefore it is supressed in the initial lag phase which is dominated by monomers. This means only secondary nucleation can lead to autocatalytic amplification of aggregate mass. Another distinguishing factor of secondary nucleation is that it is not a generic amyloid process but polymorph dependent where only some polymorphs will proliferate via secondary nucleation on fibril surface (Jeong et al., 2013).

1.4.5 Fibril fragmentation

Fibril fragmentation is another secondary process which increases the number exposed fibrils ends for templated elongation. Fragmentation involves the breaking of fibrils into smaller fragments, catalysed by specific molecular chaperones (Hsp104 for Sup35), thermal stress, mechanical perturbation by sonication, or upon biochemical changes within the cell (Lutter et al., 2019). This process can be analogous to microbial or cellular division because it generates more reactive fibril ends for elongation, creating a feedback loop for further nucleation and fragmentation. This molecular recycling results in a continuous cycle of dissociation and association events even at the final plateau of amyloid assembly. Fragmentation also enables propagation of the amyloid conformation, a feature that is crucial to the infectivity of prions and prion-like amyloid because smaller amyloid fragments can be internalised into vesicles and transported across long ranges to be taken up by non-infected cells. Thus, smaller particles are considered the primary pathogenic species whereas full length fibrils are relatively inert. This means the more pathogenic type fibril is less stable and will fragment more readily than a less or non-pathogenic fibril. Thus, fragmentation is linked to pathogenicity (Xue et al., 2009).

1.5 Experimental and modelling approaches to characterise the amyloid lifecycle

1.5.1 Overview

A number of experimental studies coupled with the application of mathematical methods of analysis have provided great insight into the morphologies of different amyloid species involved in the aggregation pathway, as well as the kinetics and mechanisms of their formation and interconversion. These methods measure the decrease in monomer concentration or the appearance of aggregate nuclei, revealing the three distinct phases of amyloid aggregation (Fig 1.1.9b) and their dependence on microscopic processes (Fig 1.1.8) (Dobson et al., 2020). The three macroscopic phases can be explained by either nucleated polymerisation (NP) or by nucleated conformational conversion (NCC). The main difference between these kinetic models is that in nucleated conformational conversion, fibrils are formed quickly from oligomers undergoing a slow conformation transition from a largely unstructured aggregate to a more organised nucleus that can template a region that will become the amyloid core. Unlike NP where nucleation events generally occur after a "critical concentration" of monomers in solution exceeds (Lutter et al., 2019), NCC explicitly considers a non-zero oligomer concentration where fibril formation can occur even if the monomer concentration is below the critical threshold (Owen et al., 2019). These non-linear growth processes are possibly due to the different properties of the amyloid species involved and the rates of their formation, combined with their high sensitivity to environmental and experimental factors.

1.5.2 Monitoring aggregation kinetics

Fluorescence spectroscopy is commonly used to monitor *in situ* the aggregate concentration. Intrinsic fluorescence spectroscopy relies on specific spectral changes upon amyloid formation whereas indirect methods measure the fluorescence from reporter dyes such as thioflavin T (ThT) or direct dyes such as Congo red (CR). It was established in 1922 that non-covalent binding of Congo red to amyloid fibrils exhibits yellow-green birefringence under crossed-

polarized light. This birefringence has since been used as a diagnostic test for amyloid fibrils in tissue sections for several decades and contributes to the definition of amyloid (Khurana et al., 2001). However, to show birefringence**,** the assay requires extreme conditions with 50–80% ethanol, high salt, and alkaline pH to allow binding to amyloid tissue sections of specific thickness. Staining with CR has also been found to be non-specific for amyloid material due to binding to collagen fibres and cytoskeletal proteins, resulting in false-positive results. A more reliable diagnostic dye is ThT (Fig 1.5.2a), a benzothiazole dye which exhibits enhanced fluorescence intensity upon non-covalent binding to in-register side-chains within the β-sheets of amyloid fibrils. Binding to amyloid is therefore more specific than CR under lower pH in relatively simple conditions. As a result, ThT fluorescence assays have remained the standard tool to monitor the kinetics of protein aggregation in real-time and fluorescence imaging of fibrils. Since its discovery in 1959, many ThT derivatives have been developed for *in vivo* detection of amyloid fibrils in the organs and tissues of live patients (Lutter et al., 2019). Fibril formation is followed by measuring the relative changes in the fluorescence intensity over time with respect to the situation at time zero (Fig 1.5.2c). Rate laws derived from the resulting ThT fluorescence curves provide insight into the molecular mechanisms of amyloid assembly as well as the mode of action of fibril formation inhibitors. Despite its longstanding and widespread use, presence of impurities or amorphous protein aggregates in the system makes the fluorescence intensity susceptible to perturbations, with evidence of non-specific binding to DNA. Moreover, ThT cannot be used to distinguish between amyloid fibrils and prefibrillar species because the technique cannot determine the molecular structure. The fluorescence signal is also only linearly dependent on the concentration of aggregate material in a relatively small range of ThT and protein concentrations, which require optimisation in each study.

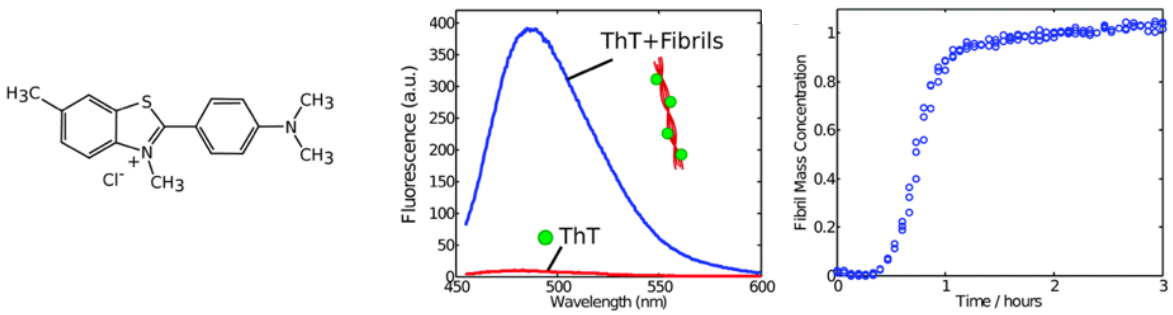

Figure 1.5.2- *(a) Structure of ThT, an extrinsic fluorophore consisting of a benzylamine and a benzothiazole ring which are connected by a C–C bond. The two planar rings of free ThT rotate mutually, quenching the fluorescence. When ThT is bound to cross-β structures, it intercalates into the surface side-chain grooves of the laminated β-sheets running parallel to the fibril's long axis. This prevents mutual rotation, allowing the delocalisation of the p electrons through both aromatic rings (Owen et al., 2019). Abolishment of quenching effects produces the characteristic fluorescence; (b) change in the emission fluorescence spectrum upon binding to amyloid fibrils, showing a dramatic enhancement of quantum yield. The typical excitation wavelength is 440 nm; (c) the fibril formation process is monitored by measuring fibril yield over time. Image from (Arosio et al., 2015).*

Other methods used to monitor *in situ* the monomer and fibril concentration include circular dichroism (CD) and nuclear magnetic resonance (NMR) spectroscopy. Both techniques provide information on the amyloid protein structure as well as the analysis of aggregation kinetics on the principle that each conformation generates a characteristic spectrum which forms the basis for protein secondary structure analysis. While CD measures the differential absorption of left and right circularly polarized light, NMR relies on the unique chemical shift value of protons, nitrogens-15, or carbons-13 in monomeric and fibrillar protein structures. As aggregation proceeds, unstructured monomers are converted into nuclei which elongate into ordered β-sheet fibril. In CD, this conformational change from monomers to fibrils can be

monitored by following the change in the random coil signal, which in turn confirms the nucleation-dependent model for amyloid assembly. NMR however, is more useful for elucidating a residue-specific secondary structure. Fourier transform infrared (FTIR) spectroscopy is another powerful biophysical technique to temporally resolve *in situ* the secondary structural transition during amyloid formation. This technique relies on the characteristic vibration frequency of hydrogen bonded back-bone amides in extended β-sheet structures (Arosio et al., 2015). Like CD and NMR, FTIR can differentiate monomers from fibrils on the basis that each secondary structure is characterized by a unique spectrum. However, FTIR can also distinguish between parallel and antiparallel β-sheets. Scattering methods such as static and dynamic light scattering and small angle scattering can also be used *in situ* to infer the peptide secondary structure and their time evolution. The basis of these techniques is that the scattering intensity of the shining light on the sample is highly dependent on particle size. Thus, scattering properties of large aggregate species will be significantly greater compared to small monomeric species. It is therefore possible to follow fibril formation as well as gain key information about the size and shape of the different amyloid species in bulk solution at each point. The light scattering pattern produced can characterise particles that range from ~100 – 1 nm depending on whether an X-ray (SAXS) or neutron (SANS) beam is used. The distance distribution function subsequently allows all the possible distances in a molecule to be calculated using the bead model as a reference to distinguish between different scattering patterns. The principle behind the bead model is that molecules of different size and shape have different distance distribution functions e.g. for spheres, the distribution function is very symmetrical, for rods it is more skewed. Both small angle scattering techniques allow high throughput studies, screening, and time-resolved analysis, making them highly complementary to other structure determination methods such as NMR.

1.5.3 Visualising amyloid

While the aforementioned methods are crucial for secondary structure characterisation, each method has limitations and cannot accurately distinguish between different types of β-sheet rich species. Therefore, *in vitro* assembly experiments are often complemented by imaging methods to provide relevant qualitative and semi-quantitative information on fibril formation. Historically, ThT and Congo Red (section 1.5.2) have been used to perform imaging of dye bound fibrils growing over time in total internal reflection fluorometry microscopy (Ban et al., 2003). Standard fluorescence microscopy is also typically used to identify antibody-stained aggregates or oligomeric species but the optical diffraction of conventional fluorescence microscopes limits the resolution to the order of λ/2 (~200 – 400 nm) depending on the fluorophore used. This low resolution cannot resolve morphological changes therefore it is unsuitable for detailed viewing of the structure of amyloid fibrils. However, recent advancements in super-resolution techniques have revolutionised fluorescence microscopy. Super-resolution fluorescence imaging techniques include STORM (stochastic optical reconstruction microscopy), PALM (photoactivated localisation microscopy), SIM (structured illumination microscopy), and STED (stimulated emission depletion). The resolution range for SIM is 40 – 50 nm, and 10 – 50 nm for STORM, STED, and PALM. This allows the analysis of the localisation and morphology of aggregates with high precision in both fixed and living cells to reveal the fine amyloid structure (Kaminski Schierle et al., 2011). PALM has been particularly useful in providing information about the intracellular structure and development of α-Syn and htt_{ex1}. Images of α-Syn were generated with resolutions <20 nm, revealing that elongation occurs on both sides of the fibril followed by an uptake of fibrils by neurons, which further confirms the seed-like properties of α-Syn (Owen et al., 2019).

TEM has been used since 1959 to generate even higher resolution (~1 – 2 nm) images of the 3-dimensional structure of amyloid fibrils extracted from liver and spleen, revealing details about fibril length, width, and the degree of twisting along the longitudinal fibril axis. NMR and X-ray crystallography are also used alongside TEM to reveal the atomic structures of amyloid fibrils. However, one limitation of TEM is that the procedure must be performed in a high vacuum to avoid deflection of electrons aimed at the sample by air particles. Moreover, liquid water, which is abundant in biological samples, would immediately evaporate in a vacuum alongside the sample. This means that in order to be visualised by standard TEM, biological samples must be fixed on a surface and dried thoroughly to prevent destruction by the vacuum and electron beam. Both the electron scattering and the likelihood of evaporation can be further avoided under cryogenic conditions where temperatures below -160°C cause water to remain amorphous (vitrified) and no ice crystals form. Vitrification and rapid freezing of the sample helps to preserve the native protein structure and prevent protein fragmentation as chemical bonds are broken by high energy electron beams. Cryo-TEM is thus more suitable especially for large protein assemblies (>500 kDa), and has been instrumental in reinforcing the cross-β structure of the amyloid core. High-resolution cryo-TEM has revealed that amyloid fibrils comprise of individual protofilaments, the number of which may depend on different precursor proteins. For example, cryo-TEM images of insulin fibrils show multiple variations in the number of protofilaments from two to six, and even more different classes of Aβ40. Moreover, analysis of Aβ fibrils shows striations that are 4.7 Å apart, further consolidating the previous interpretation from the fibre diffraction pattern and providing insight into the stability of fibrils (section 1.1.2). AFM has paved the way for further structural characterisation by demonstrating the growth of fibrils where elongation occurs at the fibrils ends by monomer addition and that diameters did not generally change (Ke et al., 2020).

AFM is therefore used in this investigation to characterise the mesoscopic morphology of protein aggregates at even higher resolution. Force-curve based AFM in particular uses a cantilever probe (Fig 1.5.3b) with a very fine tip (Fig 1.5.3c) to physically scan the specimen by intermittent contact. The amplitude, the phase, and the force are sensed by a laser beam that is reflected off the cantilever probe as it scans the sample surface in an up/down and side to side motion. As the probe passes over a raised surface, the reflected laser beam is recorded by a position-sensitive photo diode (PSPD) which detects the vertical and lateral motion of the probe (Fig 1.5.3a). The changes tracked by the PSPD generate an accurate topology map of the surface features. The detail of the image produced is therefore limited by the size of the tip. Thus, the finer the tip, the more accurate the representation of the sample. Distortions mostly occur in the X/Y plane but none in the Z measurements because there is direct contact with the specimen (Fig 1.5.3d). However, images can be corrected by computer methods to some degree. Compared to cryo-TEM, scanning is much slower than the transmission image but AFM imaging can be performed in air or in fluid, and doesn't require staining. The fibrils generated by specific peptides are deposited onto freshly cleaved mica surface and imaged at low contact forces in the pico-newton (pN) magnitude using peak force tapping mode AFM. This allows visualisation of nano-metre (nm) features such as filament assembly, different twist patterns of filaments, width, and height profiles of the different fibril polymorphs generated during fragmentation and elongation events of amyloid assembly (Marchante et al., 2017; Aubrey et al., 2020). As a result, AFM is highly complementary to cryo-TEM methodologies. One limitation of both methods is that the small field of view may not give conclusive results representative of the whole sample. Amyloid fibrils are also highly heterogenous due to the presence of several polymorphisms within a sample. As a result, images of multiple structures within a single sample are obtained and subsequently combined to generate a 3-dimensional reconstruction of the overall protein structure.

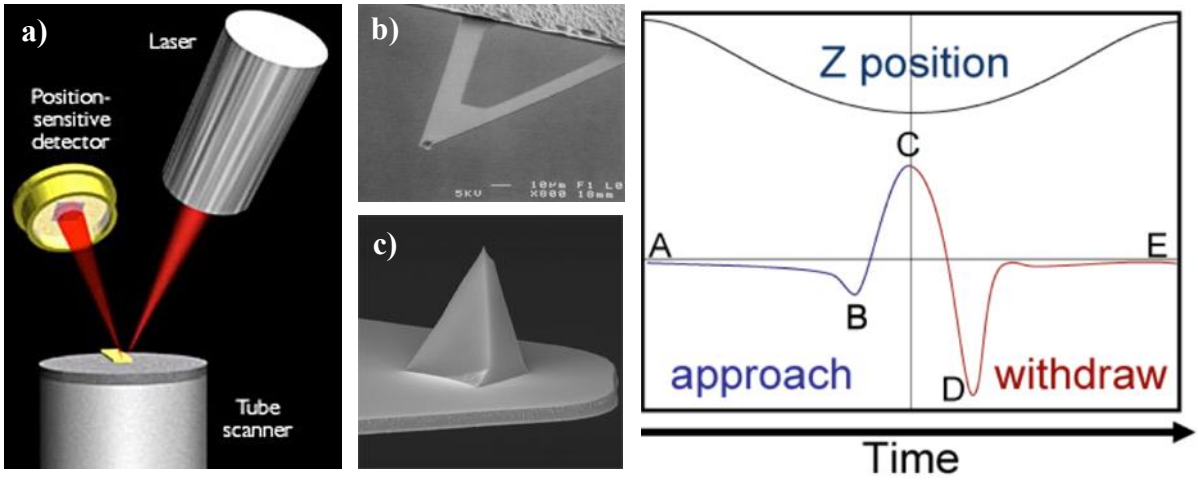

Figure 1.5.3- Force-curve based AFM. *(a) The AFM principle is based on the cantilever/tip assembly where the amplitude, the phase, and the force are detected by a laser that is reflected off the cantilever probe (b) and the deflection is recorded by the PSPD. (c) probe tip, with a radius of ~2nm, scans one pixel at a time. This pixel by pixel measurement can be reconstructed on a computer to create an accurate topology map of the surface features. (d) Force vs. time curve. As the tip of the probe approaches the specimen, a small attractive force exists between the surface and the tip, pulling the probe towards the sample (A). This cause the initial small dip in the graph (B). Once the probe is in contact with the specimen, an increasingly repulsive force takes over and deflects the probe away from the surface (C). When the probe is withdrawn, there is a sticky interaction with the sample producing the large dip (D). The spring gently oscillates as the probe detaches.*

1.6 Concluding remarks

Accumulation and deposition of amyloid fibrils is widely accepted as the origin of a large number of medical disorders that are recognised as global epidemics with increasing medical, social, and economic importance. Amyloid diseases ranging from Alzheimer's and Parkinson's diseases to type II diabetes affect over 500 million people in the world, a number that is rising rapidly. Such conditions remain without a cure, thus amyloid and prions are crucial areas of research; studying the origin and pathological manifestations of amyloidosis would aid the development of new therapeutics. As discussed above, considerable progress has been made in understanding the structural characteristics of the amyloid state, the kinetics and mechanisms directing amyloid formation, and the origins of amyloid toxicity. Alzheimer's and Parkinson's disease are the most extensively studied pathologies due to advancements in cryo-TEM and ssNMR technologies. The studies have provided high resolution atomic structures of Aβ42, Aβ40, Tau, and α-Syn to determine the contribution of amyloidosis to cell degeneration. Structural information for these amyloid fibrils is essential for clinical classification because it may allow patients to be diagnosed at a molecular (angstrom) level (Ke et al., 2020). Thus, one of the aims of this research is to identify the physical and mechanical properties of *in vitro* formed amyloid fibrils of Sup35NM and α-Syn to further understand the structural organisation of these filaments. As evident from previous studies, characterisation is not easy because many aspects of amyloidosis are highly nuanced. For example, fibrils of a particular amyloid protein may vary in length and morphology within the population, generating different amyloid strains that confer different disease phenotypes (Chuang et al., 2018). It remains unclear how these structural polymorphism arise, adding to the complexity of different amyloid systems.

A major advancement in the field of amyloid research is the development of two new classes of amyloid, functional and artificial amyloid, which play important roles *in vivo* as well as in

modern nanotechnologies, respectively. Interestingly, their unique structural and physicochemical properties are thought to arise from the infamous class of pathogenic amyloid typically associated with neurodegenerative diseases. Clues about the structure–function–pathogenesis relationship of amyloid proteins may lie in the amyloid lifecycle, the specifics of which remain under debate including the model for the elongation of fibrils, the molecular characteristics that generate prion-like amyloid, and differences in the formation of functional and disease-associated amyloid. The latter may also provide insight into the properties that cause oligomers and fibrils of disease associated systems to have such deleterious effects on a cellular level that can potentially compromise the condition of the entire organism.

A greater molecular understanding of the amyloid lifecycle is therefore required to guide future therapeutic strategies to effectively treat or prevent amyloidosis, forming the incentive for this research. The rate of fragmentation is of particular importance in this study due to the direct link to pathogenicity as more reactive fibril ends are generated upon fragmentation for elongation, further catalysing the propagation of the amyloid conformation. Model systems Sup35NM and α-synuclein are used to generate their respective prion and prion-like amyloid fibrils. AFM is subsequently used to characterise the fragmentation rate of functional and disease associated amyloid. This will reflect their stability and consolidate understanding of the molecular and mechanistic features that define prion-like.

CHAPTER 2: MATERIALS AND METHODS

2.1. Materials

2.1.1 Plasmids and strains

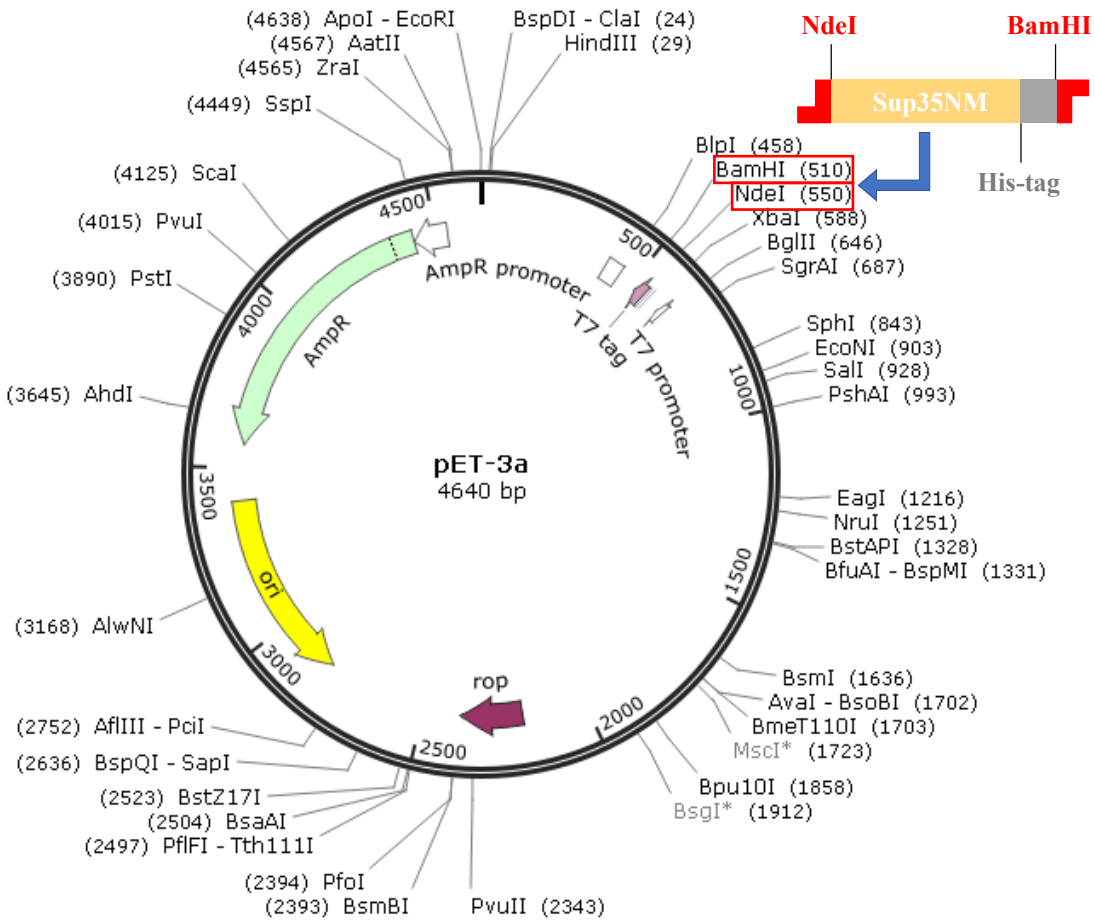

Figure 2.1.1a- Map of the plasmid containing the Sup35NM C-terminal Hexa-His gene. *Residues 1 – 253 of the Sup35 gene, encoding the NM region of the yeast Sup35 protein, were amplified from plasmid pUKC1620 by PCR and cloned into pET3a as a BamHI-NdeI fragment. The resulting pET3a-His6-NM plasmid was transformed into the E. coli strain BL21-DE3 to generate the Sup35NM C-terminal Hexa-His protein used in section 2.5.1. Image provided by Tracey Purton, Lab manager.*

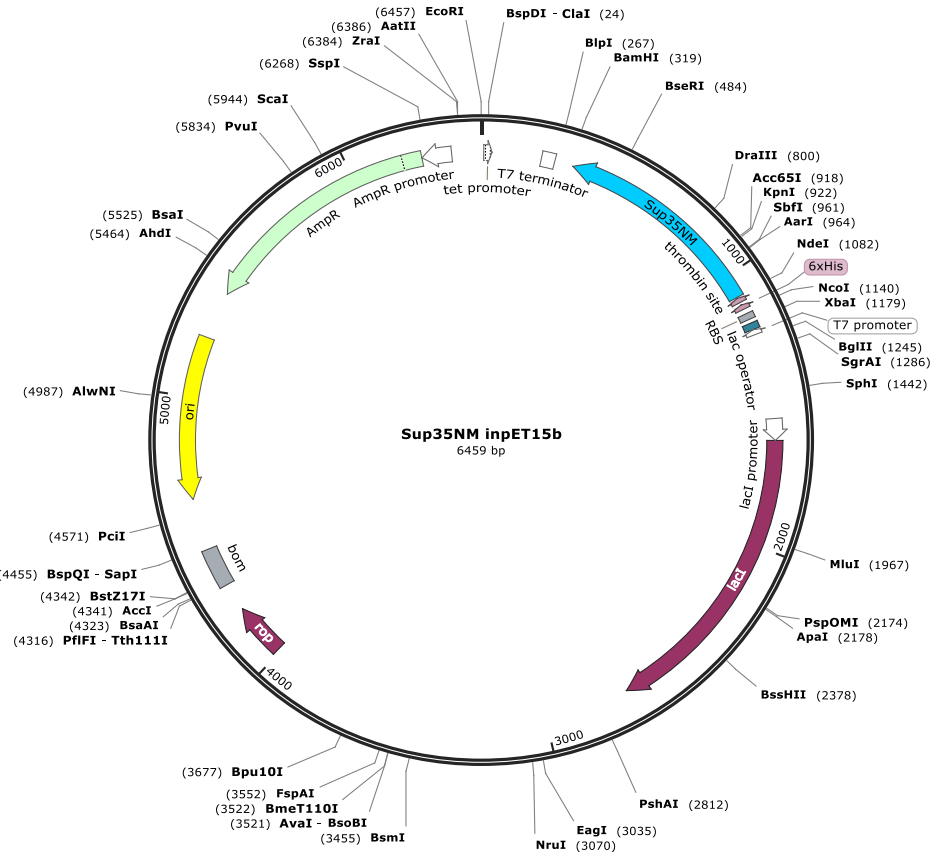

Figure 2.1.1b- Map of the plasmid containing the Sup35NM N-terminal Hexa-His gene. *Residues 1 – 253 of the Sup35 gene, encoding the NM region of the yeast Sup35 protein, were amplified from plasmid pUKC1620 by PCR and cloned into pET15b as a BamHI-NdeI fragment. The resulting pET15b-His6-NM plasmid was transformed into the E. coli strain BL21-DE3 to generate the Sup35NM N-terminal Hexa-His protein used in section* 2.5.2. *Image provided by Tracey Purton, Lab manager.*

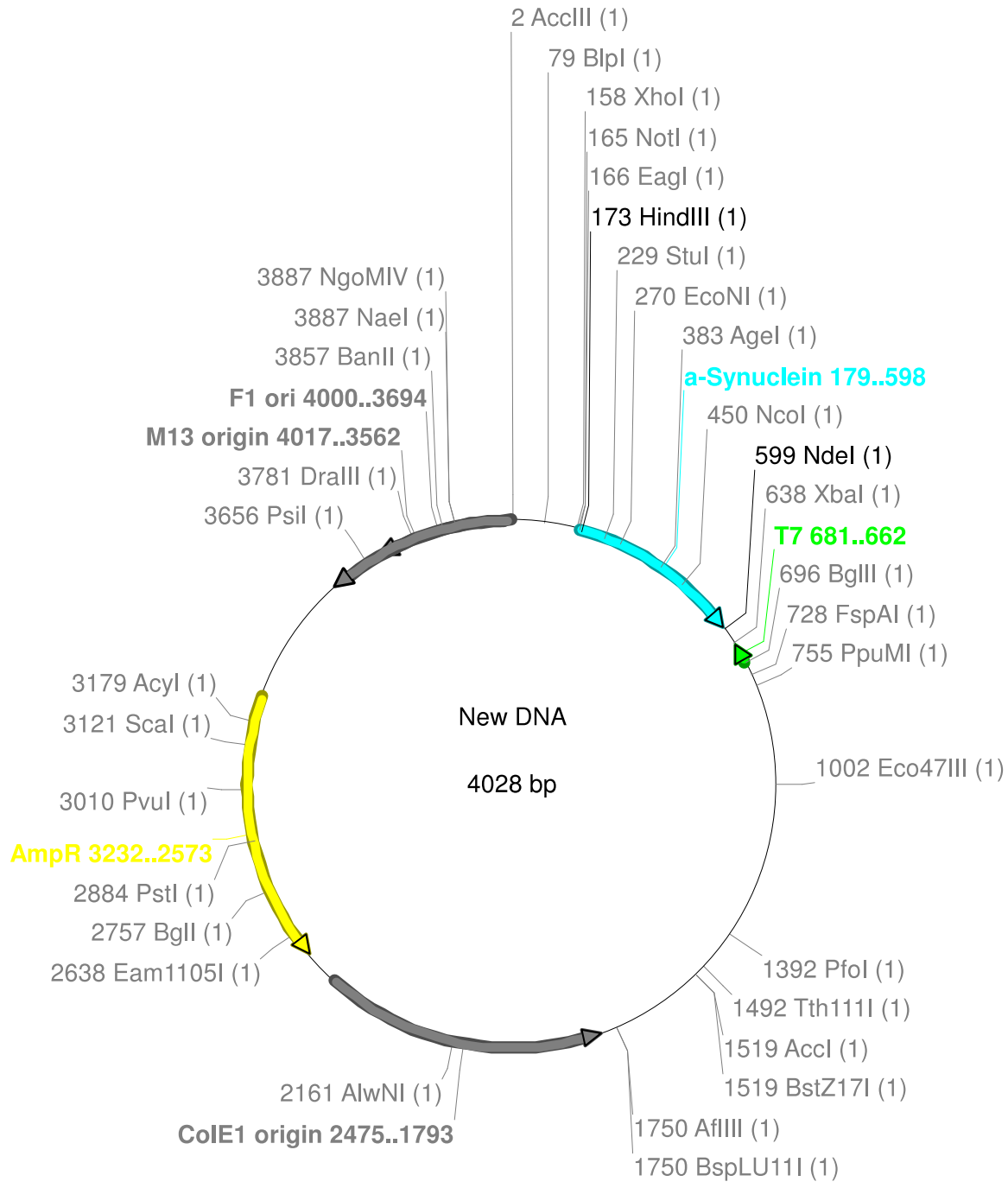

Figure 2.1.1c- Map of the plasmid containing the SNCA gene encoding the human α-synuclein protein. *The plasmid was inserted into the E. coli strain BL21-DE3 to generate the human α-synuclein protein used in section 2.5.3. Image provided by Tracey Purton, Lab manager.*

2.1.2 Lysogeny broth agar

Table 2.1.2- The components of lysogeny broth (LB) agar. *LB agar made in a 100 mL conical flask and was sterilised using a Prestige Medical Desktop autoclave before plating. Upon cooling, 0.1 mg/ml ampicillin sodium salt and 0.03 mg/ml chloramphenicol were added to facilitate selection of colonies. The BL21-DE3 E. coli strain expressing Sup35NM was streaked on LB agar under sterile conditions to generate individual colonies that would subsequently be added to liquid LB media for growth and expression.*

Substance	Lysis Buffer (100mL)
Tryptone	1 g
NaCl	1 g
Yeast extract	0.5 g
Distilled H_2O	100 mL
Agar	2 g

2.1.3 Lysogeny broth liquid media

Table 2.1.3- The components of lysogeny broth (LB) liquid media. *Each component was added to 4 sterilised 100 mL conical flasks. The mixture was further sterilised using a Prestige Medical Desktop autoclave before adding single colonies to each flask contain LB media to grown cultures of the BL21-DE3 E. coli strain expressing Sup35NM.*

Substance	Lysis Buffer (100mL)
Tryptone	1 g
NaCl	1 g
Yeast extract	0.5 g
Distilled H_2O	100 mL

2.1.4 Sup35NM C-terminal expression purification

2.1.4- The components of the buffers used in the purification of Sup35NM C-terminal prior to size exclusion chromatography. *The buffers used were: (1) 20 mM Tris-HCl pH 8.0, the component of subsequent buffers for affinity purification; (2) Melki lysis buffer (MLB); (3) Melki lysis buffer for denaturing (MLBG); (4) Melki lysis buffer for elution (MLBGE).*

Substance	20mM Tris-HCL	MLB	MLBG	MLBGE
20 mM Tris-HCL pH 8.0 stock	60.57 g of 1 M Tris-HCL pH 8.0	20 mL	20 mL	2 mL
0.5 M NaCl	-	29.2 g	29.2 g	2.92 g
Imidazole	-	1.35 g (20 mM)	1.35 g (20 mM)	1.7 g (0.25 M)
6 M GdnHCl	-	-	573 g	57.3 g
Water quality	Mili Q	Mili Q	Mili Q	Mili Q
pH	8.0	-	-	-
Total volume	500 mL	1000 mL	1000 mL	1000 mL

2.1.5 Size exclusion chromatography buffers

2.1.5- ***The components of the buffers used for the equilibration of the size exclusion chromatography column and subsequent elution of Sup35NM C-terminal from the column.*** *20 mM Tris-HCl pH 8.0 from table 2.1.4 was used to make the equilibration buffer and elution G buffer. The buffers were subsequently filtered using a 0.2 µm SFCA membrane filter and a vacuum, and degassed using a vacuum pump before adding to the size exclusion chromatography column for protein purification.*

Substance	Equilibration Buffer	Elution G Buffer
20 mM Tris HCL pH 8.0	20 mL	20 mL
0.5 M NaCl	29.1 g	29.1 g
6 M GdnHCl	-	573 g
Water quality	HPLC grade	HPLC grade
Total volume	1000 mL	1000 mL

2.1.6 Fibril formation buffers

2.1.6a- The components of the Sup35NM fibril formation buffer (SFFB). *SFFB was filtered using a 0.2 µm SFCA membrane filter and a vacuum, and degassed using a vacuum pump. Sup35NM was then exchanged into the SFFB using a PD-10 buffer exchange column to initiate fibril formation of monomeric Sup35NM.*

Substance	SFFB (400 mL)
20 mM NaH_2PO4	0.96 g
50 mM NaCl	1.17 g
Water quality	HPLC grade
pH	7.4
Total volume	400 mL

2.1.6b- The components of the α-synuclein fibril formation buffer (αFFB). *αFFB was filtered using a 0.2 µm SFCA membrane filter and a vacuum, and degassed using a vacuum pump. α-Synuclein was then exchanged into the αFFB using a PD-10 buffer exchange column to initiate fibril formation of monomeric α-synuclein.*

Substance	αFFB (400 mL)
25mM NaH_2PO4	2.0 g
150 mM NaCl	3.51 g
NaN_3	1 mL
Water quality	HPLC grade
pH	7.4
Total volume	400 mL

2.2 Expression of C-terminal Hexa-His tagged Sup35NM

The *E. coli* strain BL21-DE3, modified with the pET3a plasmid containing the Sup35NM C-terminal Hexa-His gene (Fig 2.1.1), was streaked onto several LB agar plates containing 0.03 mg/ml chloramphenicol and 0.1 mg/ml ampicillin sodium salt. Plates were subsequently

incubated overnight at 37°C to allow sufficient growth. The following morning, small individual colonies with less chance of acquiring random mutations were selected (Fig 2.2.1) and used to inoculate 4x100 mL conical flasks of LB broth supplemented with 0.1 mg/ml ampicillin sodium salt and 0.03 mg/ml chloramphenicol for further selection. Flasks were then incubated overnight in a 37°C shaker for 16 hours. The overnight cultures were subsequently spun down at 4000 rpm for 5 minutes and the resulting supernatant was discarded. The remaining pellets were resuspended in LB and transferred to 4x1 L baffled flasks of the same LB medium and incubated in a 37°C shaker. On reaching the log phase of the bacterial growth cycle as indicated by an OD_{600} of approximately 0.6, expression was induced with 1 mL of 1mM IPTG for 4 hours. Following the 4 hour induction course, cells were harvested by centrifugation at 4000 rpm for 10 minutes. The supernatant was discarded and the pellets were washed without lysing in 20 mL of MLB buffer. Cells were then pelleted by centrifugation at 4000 rpm for 5 minutes and subsequently stored at -80°C for purification.

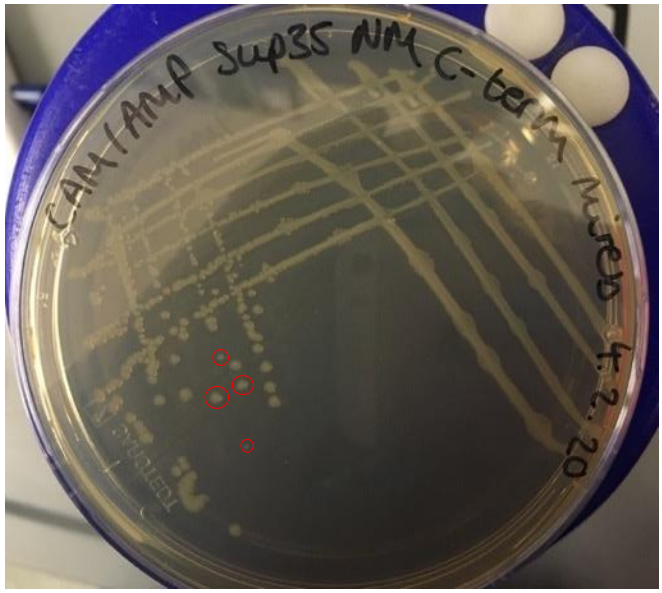

Figure 2.2.1- LB agar plate streaked with the BL21-DE3 E. coli strain expressing Sup35NM C-terminal. *The smallest colonies (circled in red), selected with 0.03 mg/ml chloramphenicol and 0.1 mg/ml ampicillin sodium salt, were removed for further growth as these are less likely to acquire random mutations.*

2.3 Expression and purification of C-terminal Hexa-His tagged Sup35NM

In preparation for the affinity purification step, frozen cell pellets were resuspended in 20 mL of MLBG buffer at a 5:1 (v/v) ratio and placed in ice to prevent defrosting. Mixtures were then lysed by sonication at an amplitude of 22 microns for 3 minutes with a minute interval back on ice between each 1 minute burst to disrupt the cell pellets until completely dissolved. The lysate was then centrifuged at 13000 rpm for 30 minutes to remove the cell debris (pellet) and collect the supernatant for further purification via Ni-NTA column. The Ni-NTA affinity resin was prepared from 4 mL of Chelating Sepharose Fast Flow (GE Healthcare) that was sequentially washed in a small plastic column with one column volume (CV) of mQH_2O, 0.2 M $NiCl_2$, MLB, and MLBG buffer. The equilibrated resin was resuspended in 4 mL of MLGB buffer and added to the lysate supernatant. The mixture was incubated for 1 hour at room temperature on a tube roller to allow agitation to improve binding of protein to the Ni-NTA resin. Following the incubation, the lysate/resin was collected by centrifugation at 4000 rpm for 5 minutes. The supernatant was discarded and the resulting pellet was subjected to two MLBG washes before being resuspended in MLBG and transferred to a poly-prep column. After a final wash with 1 CV of MLBG, elution of Sup35NM was achieved with the addition of 6 mL of MLBGE. 5 mL of the elution was immediately transferred to a size exclusion purification column which was previously equilibrated with 1 CV of HLPC water, 1 CV of Equilibration Buffer and 1 CV of Elution G Buffer, respectively. The size exclusion purification protocol was run using HiLoad 16/600 Superdex 200pg (GE Healthcare) column in an AKTA prime Plus chromatography system (GE Healthcare). Fractions corresponding to the Sup35 peak as displayed throughout the run were collected and pooled. The absorbance of the pool was measured at 280nm to give the final protein concentration. The elute was kept in GdnHCL, a denaturant which keeps Sup35NM in the monomeric form to prevent fibril formation. The sample was then snap frozen in liquid nitrogen in 1 mL aliquots and stored at -80°C for use in future fibril-forming reactions.

2.4 SDS-PAGE analysis of C-terminal Hexa-His tagged Sup35NM

To confirm the presence of monomeric Sup35NM at all stages of the purification, SDS-PAGE analysis was performed on samples collected at key points of the investigation. The samples collected included: (T) total lysate collected after sonication of the sample; (S) spun lysate collected after the protein mixture was spun down; (FT) flow through which was the supernatant left over from the Ni-NTA column; (Ni) sample eluted from the Ni-NTA pellet that was added to the ÅKTA for size exclusion chromatography; (P) final stock of Sup35NM collect from the ÅKTA column: (F1, F10, F19 and F25) fractions corresponding to the start and end of the Sup35 peak. 20 µL of each sample was transferred into a new Eppendorf tube, to which 20 µL of SDS loading buffer with DTT was added. Samples were then heated to boiling point for 5 minutes before being pulse spun for 5 seconds at room temperature. 15 µL of each sample and 10 µL of the ladder was loaded and assessed using a 12% SDS-PAGE gel. The gel tank was filled with 1X TGS running buffer and 120 V were applied for approximately 10 minutes, and then increased to 180 V for approximately 45 minutes when the dye had reached the stacking gel. Gel was then removed from the tank and submerged in instant blue dye while left on shaker for 30 minutes to allow the bands to be visualised. GeneSys software analysis was subsequently used to image the mini protein gel under Coomassie blue with the iris, zoom and focus maximised. Images were processed further to adjust the brightness and contrast before being exported and saved as TIFF.

2.5 *In vitro* fibril formation

2.5.1 C-terminal Hexa-His tagged Sup35NM

Controlled fibril formation was initiated upon removal of GdnHCL from Sup35NM and addition of fibril formation buffer. This buffer exchange is performed on 1 mL of 48.76 µM purified monomeric protein using a PD-10 column (GE Healthcare) as per manufacturer's

instruction. The PD-10 column was first equilibrated with 2.5 ml of stereo filtered SFFB that was produced using a Minisart Syringe Filter 0.2 μm. 1 mL of the Sup35NM pool was then added to the column, followed by another 1.5 mL of SFFB once the protein had fully entered the column. A final 3.5 mL of SFFB was added to elute the protein, the absorbance of which was measured at A_{280} to give a concentration of 0.14 μM using the beer-lambert law formula:

$A = \varepsilon cl$

A = Absorbance at A_{280}

ε = Molar absorbance coefficient $M^{-1}cm^{-}$

c = Molar concentration M

l = optical path length cm

A_{280} = 0.415

ε = 30.69 $\mu M^{-1}cm^{-1}$

l = 1 cm

c = A/εl

c = 0.415 / (1 x 30.69) = 0.014 μM (in 100 μL)

0.014 x 10 = 0.14 μM (in 1000 μL)

Sup35NM immediately dimerises and aggregates into fibrils upon addition of SFFB so the protein was aliquoted into protein LoBind Eppendorf tubes and allowed to polymerise at 30°C (quiescent) for further AFM imaging.

Further analysis of Sup35NM C-terminal was discontinued due to the Covid-19 lockdown. As a result, all Sup35NM C-terminal samples were discarded. Upon removal of the lockdown,

new purified protein samples could not be generated due to time constraints. Thus, further analysis was performed on new samples of Sup35NM N-terminal and α-synuclein that were kindly provided by Tracey Purton, lab manager.

2.5.2 N-terminal Hexa-His tagged Sup35NM

The buffer exchange is performed on 2 mL of 37 μM purified monomeric protein using a PD-10 column (GE Healthcare) as per manufacturer's instruction. The PD-10 column was first equilibrated with 25ml of stereo filtered SFFB that was produced using a Minisart Syringe Filter 0.2μm. 2 mL of the Sup35NM pool was then added to the column, followed by another 0.5 mL of SFFB once the protein had fully entered the column. A final 3.5 mL of SFFB was added to elute the protein which was collected in three fractions in LoBind Eppendorf tubes. The absorbance of each fraction was measured at A_{280}. The absorbance of fraction 1 and 2 was too high therefore only the concentration of fraction 3 was calculated. The protein was subsequently incubated at 30°C for one week to allow polymerisation into fibrils which would then be imaged by AFM before undergoing fragmentation by sonication.

A_{280} of fraction 1 = 1.06

A_{280} of fraction 2.8.1

A_{280} of fraction 3 = 0.65

c = 0.65 / (1 x 30.69) = 0.02 μM (in 100 μL)

0.02 x 10 = 0.2 μM (in 1000 μL)

2.5.3 α-synuclein

This buffer exchange is performed on 2 mL of 484.1 μM purified monomeric protein using a PD-10 column (GE Healthcare) as per manufacturer's instruction. The PD-10 column was first

equilibrated with 25ml of stereo filtered αFFB that was produced using a Minisart Syringe Filter 0.2µm. 2 mL of α-synuclein was then added to the column, followed by another 0.5 mL of αFFB once the protein had fully entered the column. A final 3.5 mL of αFFB was added to elute the protein, 700 µL of which was collected in a LoBind Eppendorf tube. The concentration of the elute was then diluted by a dilution factor of 10:100 and the absorbance measured at A_{280} to give the final concentration.

$A_{280} = 0.3$

$\varepsilon = 5120\ M^{-1}cm^{-1}$

c = M

l = 1 cm

0.3 x 10 = 3

c = 3 / (1 x 5.12) = 0.59 µM (in 100 µL)

0.59 x 10 = 5.9 µM (in 1000 µL)

5.9 x 0.7 = 4.13 µM (in 700 µL)

The protein was then incubated at 37°C on a shaker for one week to allow polymerisation into fibrils which would then be imaged by AFM before undergoing fragmentation by sonication.

2.6 Thioflavin T assays

2.6.1 C-terminal Hexa-His tagged Sup35NM growth assay preparation

Thioflavin T assays assay was used to follow fibril kinetics including formation, growth and the division of amyloid aggregates. The essay required a black puregrade 96-well plate (BRAND) (Corning Assay Plate, 96 wells, Non-Binding surface) and Thioflavin T to measure the fluorescence intensity. 99 µL of purified Sup35NM and 1 µL of ThT was aliquoted into 5

separate wells in the middle of the plate, giving a final protein concentration of 0.138 μM in a final volume of 100 μL. 100 μL of distilled water was added to all outside wells to prevent heat transfer. The plate was then sealed with Starseal Advanced Polyolefin Film (Starlab).

2.6.2 C-terminal Hexa-His tagged Sup35NM ThT kinetic assay

Polymerisation was monitored using a BGM labtech CLARIOstar at 30°C. Five experimental replicates were run in the same plate which was scanned using top optic. The fluorescence intensity was measured using the ThT pre-sets with excitation set to 440-12, dichroic at auto 460 and emission at 480-12. Readings were recorded every 15 minutes for 18 hours, producing ThT traces that were subsequently used to construct Sup35NM fibril ThT fluorescence curves.

2.6.3 Thioflavin T analysis

The .csv file produced by the Thioflavin T kinetics assay was imported into MATLAB to create ThT fluorescence curves with Growth time (hours) plotted as the X axis and ThT fluorescence intensity as the Y axis (Fig 3.1.3).

2.7 Controlled fibril fragmentation through mechanical perturbation

2.7.1 Fragmentation of N-terminal Hexa-His tagged Sup35NM fibrils

Sup35NM N-terminal fibril solution was stored in a LoBind Eppendorf tube at 30 ºC for one week. Fraction 3 obtained from the PD-10 column (section 2.5.2) was used. Since the initial concentration was thought to be 21.81 μM, 91.7 μL of the sample was diluted to 10 μM with 108.3 μL SFFB to create a 200μL sample for the fragmentation assay. Upon revision however, the final protein concentration was in fact 0.1 μM. 200 μL of *de novo* Sup35NM placed on ice cooled water-bath was pulse sonicated by a Q Sonica Q125 sonicator (frequency of 20 kHz) for 5 seconds at 20% amplitude. 20 μL of the sample was withdrawn to be imaged by AFM.

2.7.2 Fragmentation of α-synuclein fibrils

α-synuclein solution was stored in a LoBind Eppendorf tube in a 37 ºC shaking incubator for one week. The elute obtained from the PD-10 column (section 2.5.3) was used. Since the initial concentration was thought to be 20.1 μM, 100 μL of the sample was diluted to 10 μM with 100 μL SFFB to create a 200μL sample for the fragmentation assay. Upon revision however, the final protein concentration was actually 2.1 μM. 200 μL of *de novo* α-synuclein placed on ice cooled water-bath was pulse sonicated by a Q Sonica Q125 sonicator (frequency of 20 kHz) in consecutive 5 s on/off cycles (5 second intervals followed by 5 seconds of rest). The sonication series comprised of 5, 20, 80 and 320 seconds (time sonicating) at 20% amplitude. At each time point, 20 μL of the sample was withdrawn to be imaged by AFM.

De novo α-synuclein was subsequently further diluted to 0.4 μM (5x dilution) and 0.2 μM (10x dilution). The same sonication series used for 2.1 μM *de novo* α-synuclein was applied to each new concentration and 20 μL of sample was withdrawn after each time point for AFM imaging.

2.8 Atomic Force Microscopy

2.8.1 Mica disc preparation

Firstly, an Agar Scientific 9.9 mm Mica Disk was securely attached to an Agar Scientific 15 mm SPM Specimen Disk by double sided tape. This would be the platform for viewing Sup35NM fibrils using AFM. PVC tape was then used to cleave the exposed layer of mica to provide a flat and clean surface for protein fibrils to be deposited on.

2.8.2 Sample preparation

2.8.2.1 Sup35NM sample preparation

20 μL of protein was deposited onto freshly cleaved mica which was then immediately stored in a petri dish with the bottom covered by clean filter paper to prevent contamination as the fibrils attach to the exposed mica surface. Following a 10 minute incubation at room temperature, excess sample was removed by washing with 1 mL of stereo-filtered mQH_2O produced using a Minisart Syringe Filter 0.2μm, and then dried under a gentle stream of $N_{2(g)}$. After sample preparation, the mica disk is stored in a Petri dish until imaging.

2.8.2.2 α-synuclein sample preparation

20 μL of protein was deposited onto freshly cleaved mica which was then immediately stored in a petri dish with the bottom covered by clean filter paper to prevent contamination as the fibrils attach to the exposed mica surface. Following a 10 minute incubation at room temperature, excess sample was removed by washing with 1 mL of stereo-filtered mQH_2O produced using a Minisart Syringe Filter 0.2μm, and then dried under a gentle stream of $N_{2(g)}$. After sample preparation, the mica disk is stored in a Petri dish until imaging.

2.8.3 Gentle force-curve based AFM imaging

Fibril imaging was performed at room temperature using a Bruker Multimode 8 scanning probe microscope with a Nanoscope V controller, using the ScanAsyst peak-force tapping imaging mode. Bruker SCANASYST-AIR model AFM probes (Silicon Tip on Nitride Lever with tip height = 2.5 – 8 μm, nominal tip radius – 2nm, nominal spring constant = 0.4 N/m and nominal resonant frequency = 70 kHz) used throughout. Multiple 10 μM x 10 μM areas of the surface were scanned at a resolution of 1024 x 1024 pixels. All images captured were saved as .png file alongside the processed .000 file for further processing and analysis.

2.8.4 AFM image analysis

Bruker Nanoscope Analysis software (version 1.5, Bruker) was used to process and analyse all images saved as .000 files. Firstly, the image baseline was flattened by first order correction without thresholding to remove tilt and bow. The action was repeated to flatten the image further by the second order correction using a threshold value depending on the image. Flattened images were further processed to adjust the colour scheme, brightness and contrast, before being exported as .png files. Both the processed image files and raw data files were saved for recognition by the fibril tracing algorithm written in MATLAB.

2.9 Structural data extraction of fibril dimensions

In order to quantify and compare the overall heterogeneity of Sup35NM and α-synuclein fibrils, as well as fibrils within the same sample, nano-morphometric measurements were performed on individual filaments within each dataset. 200 fibrils from each sample were traced and digitally straightened using an in-house application to provide the width and length distribution of that population, before and after different lengths of controlled mechanical perturbation by sonication were applied (Supplementary figures 1-5 and table 1). The mean fibril lengths and widths were calculated and subsequently used in a heteroscedastic T-test where all sonicated α-synuclein amyloid fibril samples are compared to the non-sonicated sample. Tables 3.3.1a and 3.3.1b show whether the differences in the morphology of fibrils were significant, as suggested by the final p-values. The same pixel density is maintained for all images within the dataset.

CHAPTER 3: RESULTS

3.1 Fragmentation of Sup35NM amyloid fibrils

3.1.1 Expression and purification of C-terminal Hexa-His tagged Sup35NM

Synthetic Sup35NM C-terminal prion particles were produced *in vitro* from recombinant monomeric Sup35NM. As described in section 1.1.6, wild-type yeast prion protein Sup35 is composed of three regions, namely N, M, and C. The N (residues 1–123) and M (124–253) regions regulate amyloid formation and prion maintenance, while the C-terminal region (residues 254–685) controls the translation termination function (Marchante et al., 2017). The N and M regions (Sup35NM, residues 1–253) are therefore sufficient to confer the [*PSI*+] phenotype in yeast. The Sup35NM protein was expressed in the *E. coli* strain BL21-DE3 modified with the pET3a plasmid containing the Sup35NM C-terminal Hexa-His gene (section 2.1.1a). Cells were subsequently lysed by sonication and the recombinant Sup35NM protein monomers were extracted and purified under denaturing conditions (section 2.3). The elute obtained from size exclusion chromatography served as the monomeric Sup35NM C-terminal stock for future fibril-forming reactions (Fig 3.1.1a-b).

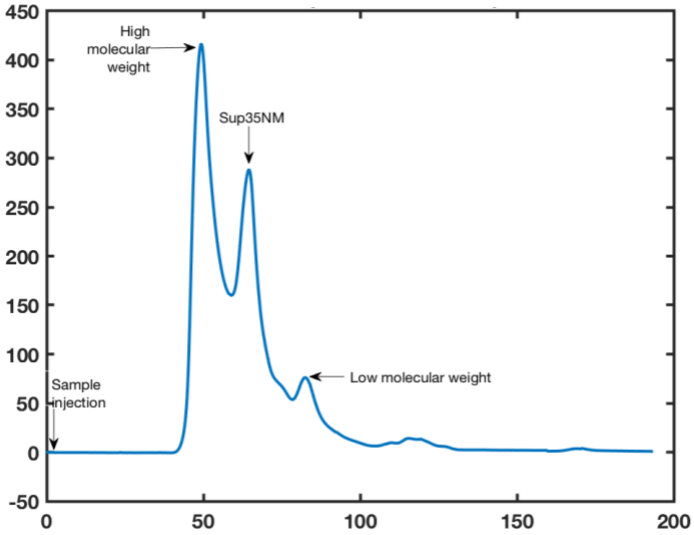

Figure 3.1.1a- Sup35NM C-terminal size exclusion chromatography graph. *Plot of the UV absorbance against elution volume. Protein mixture is separated based on size whereby larger proteins elute first because they are too big to pass through the porous matrix of the column, therefore they travel a shorter distance. These proteins are represented by the largest peak which is mainly denatured proteins from the sonication step to lyse cells. The second peak is Sup35NM and the last peak corresponds to smaller proteins which elute last because they travel through the porous matrix and the moving buffer, therefore travel the greatest distance.*

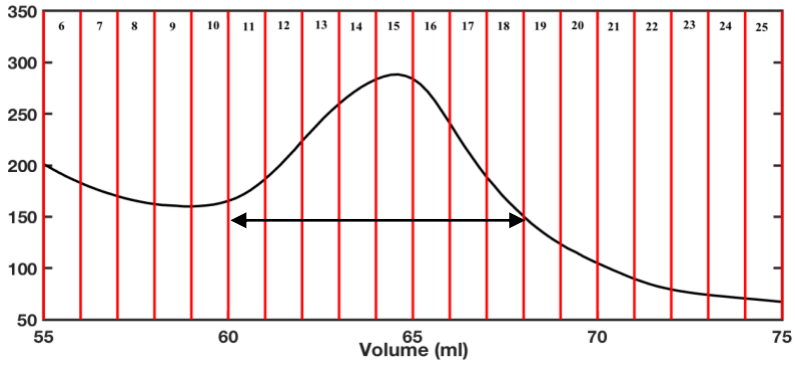

Figure 3.1.1b- Fractions of the Sup35NM C-terminal peak. *Close up of fractions 11 to 18 corresponding to the Sup35 peak which were collected and pooled. The pool was then snap frozen in liquid nitrogen as 1 mL aliquots which were then stored at -80 ºC until required.*

Table 3.1.1- The absorbance of each fraction corresponding to the Sup35NM C-terminal peak measured at 280 nm. *The absorbance of fractions 11 to 18 corresponding to the Sup35NM peak was measured at 280 nm before they were pooled. The OD of the pool was measured to be 1.453, from which the final protein concentration was subsequently calculated to be 48.76 μM using the beer-lambert law formula (section 2.5.1).*

Fraction	Absorbance at 280nm
11	1.025
12	1.198
13	1.426
14	1.595
15	1.665
16	1.546
17	1.265
18	1.00

3.1.2 Sup35NM C-terminal SDS-PAGE analysis

A 12% SDS-PAGE gel was run using samples collected at key points confirming the presence of monomeric Sup35NM at all stages of the purification protocol. The gel (Fig 3.2) shows Sup35NM is present in all 9 samples but most abundant in the first 5. The weight of monomeric Sup35NM is ~30kDa but the protein comes off at ~35kDa. The distortion of the bands is possibly due to the guanidine salt present in each sample to supress the protein in the monomeric form.

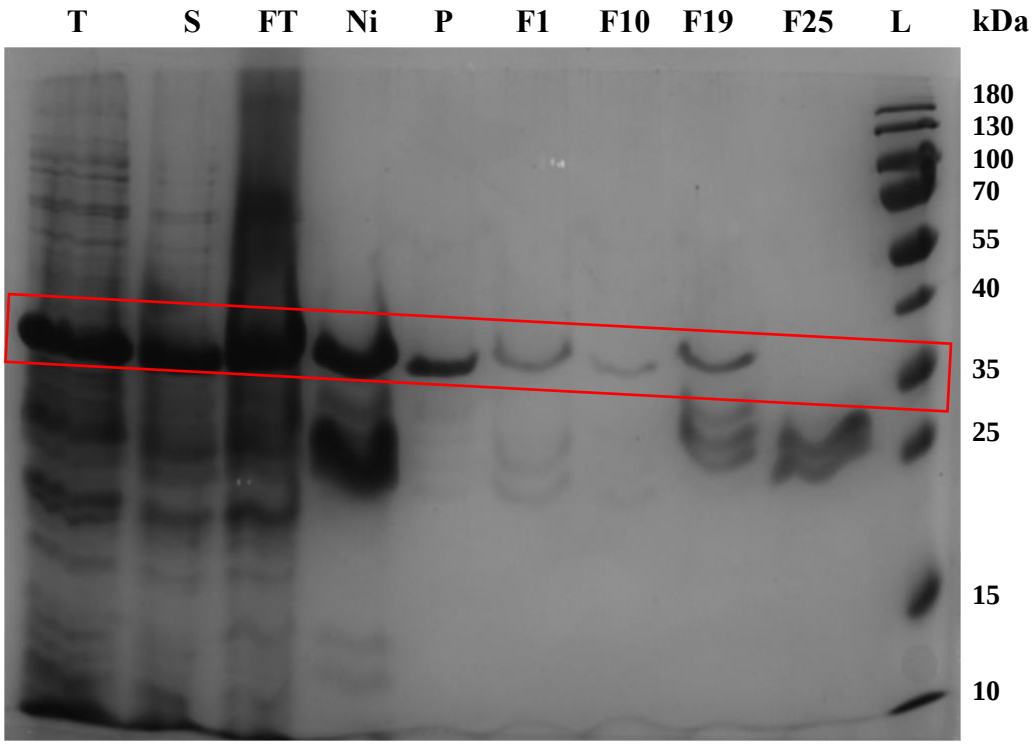

Figure 3.1.2- Sup35NM C-terminal SDS-PAGE gel. *12% SDS-PAGE gel confirming the presence of monomeric Sup35NM (red box) in all 9 samples collected from all the steps of the purification stage, but it is most prevalent in the first 5 samples. The samples are: (T) total lysate collected after sonication of the sample; (S) spun lysate collected after the protein mixture was spun down; (FT) flow through which was the supernatant left over from the Ni-NTA column; (Ni) elute from the Ni-NTA pellet that was added to the ÅKTA for size exclusion chromatography; (P) final stock of Sup35NM collect from the ÅKTA column; (F1, F10, F19 and F25) fractions corresponding to the start and end of the Sup35NM peak from Fig 3.1.1b; (L) ladder.*

3.1.3 *De novo* fibril formation of C-terminal Hexa-His tagged Sup35NM

Once the presence of monomeric Sup35NM was confirmed in the pool, a PD-10 buffer exchange column was used, as described in section 2.5.1, to initiate fibril formation. The growth of *de novo* Sup35NM was measured using the methodology described in section 2.6.1

and 2.6.2. The Sup35NM polymerisation reaction exhibits sigmoidal shape ThT fluorescence curve expected for amyloid formation, with the characteristic lag phase, elongation phase, and final plateau (Fig 3.1.3). The lag time of all 5 samples is fairly consistent, lasting approximately 2 hours in length. The gradient of the curves during the exponential elongation phase is more varied, lasting approximately 8-12 hours. The variation in the time taken to reach the final plateau phase is possibly due to the depleting monomer concentration as more is being added to the elongating ends of existing fibrils.

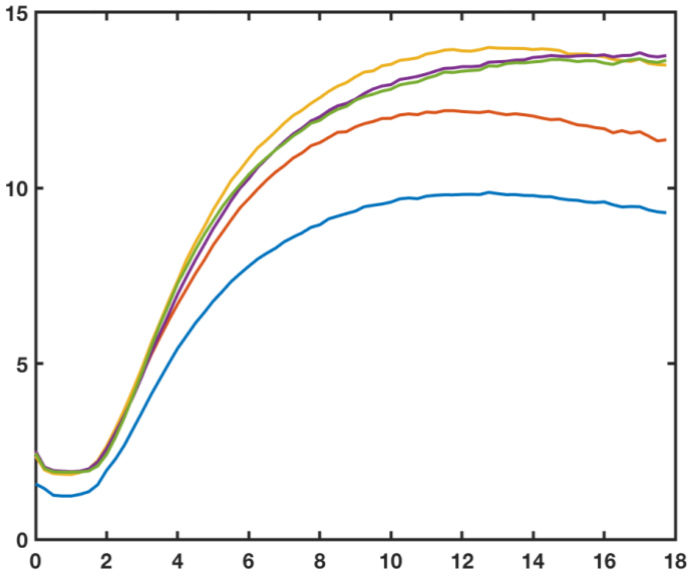

Figure 3.1.3- Sup35NM C-terminal polymerisation monitored using Thioflavin T. *Five experimental replicates were plotted, all producing a characteristic sigmoidal growth curve illustrating the three distinct stages of de novo fibril formation, namely a lag phase, an exponential elongation phase, and a final plateau. The monomeric Sup35NM C-terminal concentration was 0.14 μM, which was achieved by dilution with SFFB.*

3.1.4 AFM imaging of N-terminal Hexa-His tagged Sup35NM amyloid fibrils

Once the fibril formation of Sup35NM C-terminal was confirmed by ThT analysis, fibrils were subsequently imaged by AFM using the 0.14 μM sample from section 2.5.1 once they had fully

reached the plateau phase. Fibrils were not visible when imaged, even when Sup35NM C-terminal expression and purification was repeated several times. This stage was subsequently interrupted by the Covid-19 lockdown therefore all Sup35NM C-terminal samples were discarded. Due to time constraints, the following AFM imaging and analysis was conducted on Sup35NM N-terminal provided by Tracey Purton.

Gentle force-curve based AFM imaging was performed on Sup35NM N-terminal in order to analyse the fibril dimensions. The sample used was fraction 3 collected from the PD-10 column (section 2.5.2), the concentration of which was 0.2 μM. The concentration was initially believed to be 21.81 μM due to an error in calculation therefore 91.7 μL of the sample was diluted to 10 μM with 108.3 μL of SFFB to create a 200 μL sample for the subsequent fragmentation assay. 10 μM was chosen to be the standard concentration for imaging because from previous attempts, the amount of aggregated material produced at this concentration was optimum for subsequent fibril analysis. If the sample concentration is too high then it would be difficult to image and analyse distinct fibrils. Upon revision however, the final protein concentration was in fact 0.1 μM. Before conducting the assay, 20 μL of *de novo* Sup35NM fibrils was removed to be imaged by AFM, while the rest was subjected to 5 seconds of mechanical perturbation by sonication. Imaging was thus performed on fibrils in the plateau phase before (0 s) and after (5 s) sonication, showing multiple clusters of fibril particles. Sonicated fibrils appear shorter and more dispersed, with larger fibril clusters compared to non-fragmented initial samples. Due to the large dispersion of fibrils and fibril clusters, images were difficult to obtain within the short timeframe. Therefore, imaging of Sup35NM N-terminal was terminated after 5 s sonication and the analysis was directed to α-synuclein fibrils.

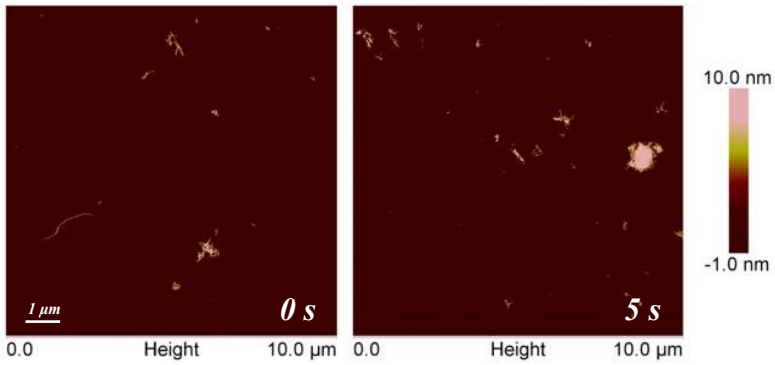

Figure 3.1.4- AFM images of Sup35NM N-terminal amyloid fibrils before and after sonication. *(left) de novo Sup35NM fibrils in the plateau phase before sonication (0 s). (right) Sup35NM fibrils after 5 seconds of pulse sonication. Samples produced de novo using 0.1 µM monomeric Sup35NM. The images are 10 µm x 10 µm in scan size at a resolution of 1024 x 1024 pixel. The height bar shows a range from -1 nm to +10 nm with respect to mica surface.*

3.2 Fragmentation of α-synuclein amyloid fibrils

As with Sup35NM, a PD-10 buffer exchange column was used to initiate fibril formation of α-synuclein, followed by gentle force-curve based AFM imaging performed on the elute (section 2.5.3). As in section 3.1.4 with Sup35NM, the initial concentration of α-synuclein was miscalculated to be 20.1 µM therefore 100 µL of the sample was diluted to 10 µM with 100 µL of αFFB to create a 200 µL sample for the subsequent fragmentation assay. Upon revision, the final protein concentration was calculated to be 2.1 µM. The corresponding AFM images are shown in figure 3.2.1. Both the *de novo* α-synuclein and Sup35NM N-terminal samples were intended to have the same concentration for a fair comparison between the two data sets. Although the concentrations are significantly different, some comparison between the AFM images can still be made. For example, Sup35NM N-terminal fibrils appear more clustered despite the low concentration (Fig 3.1.4) whereas α-synuclein fibrils appear much longer, forming larger networks (Fig 3.2.1). However, comparison between size and number of clusters was difficult because very few AFM images of Sup35NM obtained due to time constraints.

3.2.1 AFM imaging of *de novo* α-synuclein amyloid fibrils

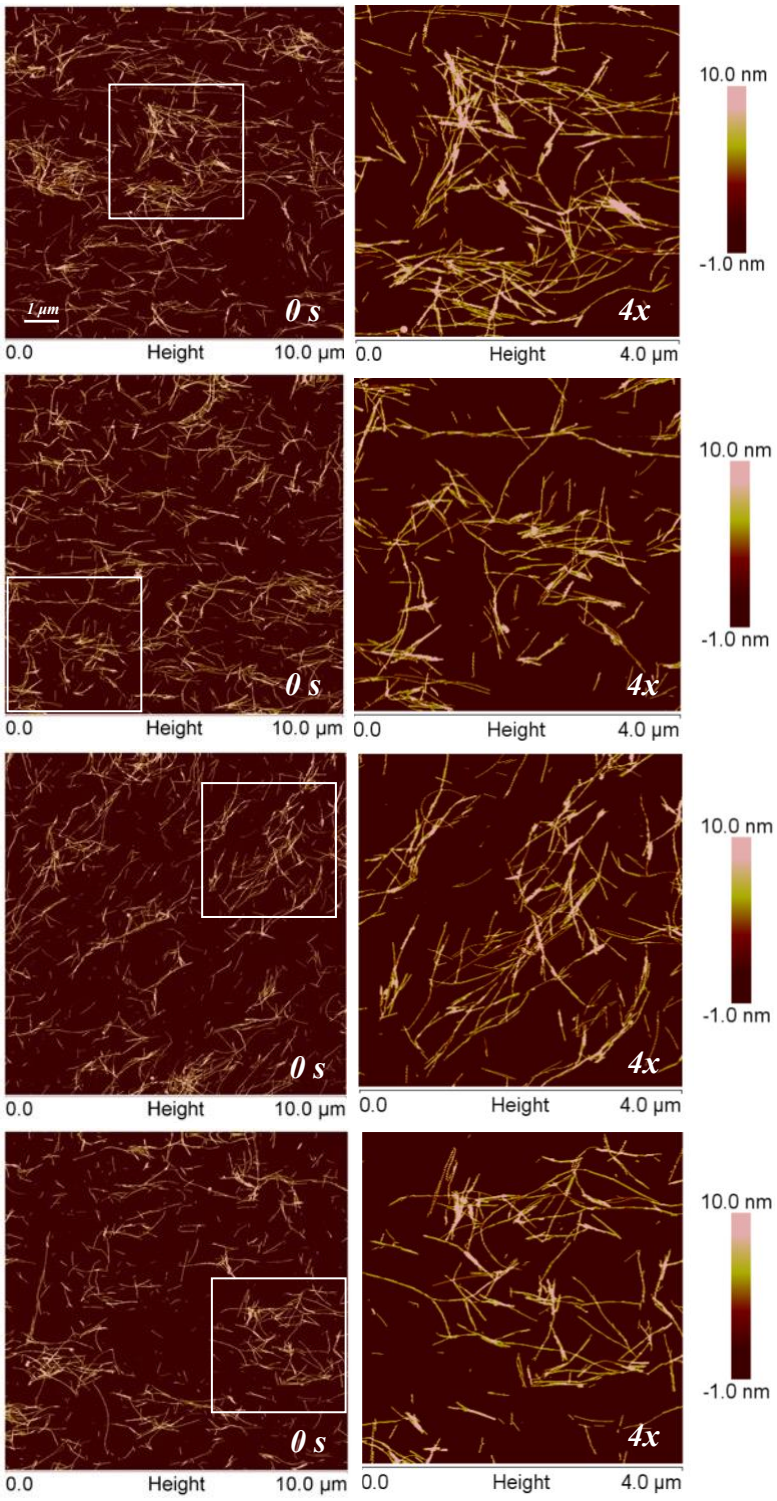

Figure 3.2.1- AFM images of de novo α-synuclein amyloid fibrils in the plateau phase. *Fibril samples produced de novo using 2.1 µM monomeric α-synuclein. The images are 10 µm x 10 µm in scan size at a resolution of 1024 x 1024 pixel. This size is represented by the scale bar. The height bar shows a range from -1 nm to +10 nm with respect to the mica surface.*

3.2.2 AFM imaging of sonicated α-synuclein amyloid fibrils

As with Sup35NM N-terminal in section 3.1.4, 2.1 μM α-synuclein fibrils were fragmented by pulse sonication in consecutive 5 s on/off cycles (5 second intervals followed by 5 seconds of rest) at an amplitude of 20% for 5, 20, 80 and 320 seconds. 20 μL of the sample was removed after each timepoint to be imaged by AFM. As expected, qualitative inspection of the AFM images during the course of the fragmentation series shows that amyloid fibrils fragment into increasingly smaller particles under greater mechanical perturbation. Figure 3.2.2a shows 2.1 μM α-synuclein fibrils sonicated for 5 seconds. At the lowest sonication timepoint, the sizes of the particles exhibits significant heterogeneity compared to the particles observed after 20 s, 80 s and 320 s at the same concentration in figure 3.2.2b. At these higher timepoints, the particle size gradually reduces to appear more uniform. Compared to Sup35NM (Fig 3.1.4), α-synuclein fibrils sonicated for 5 s (Fig 3.2.2a) also appear less dispersed and clustered. The greater clustering of Sup35NM is likely to be linked to inactivity but this deduction demands more Sup35NM AFM data. Regardless, it may also be linked to the fewer fibrils observed in the sonicated Sup35NM sample as larger clusters may be more difficult to fragment into smaller particles. Due to the high density of fibrils observed in sonicated α-synuclein AFM samples, *de novo* α-synuclein was subsequently diluted to 0.4 μM (5x dilution) to generate AFM images of more distinct fibrils, the dimensions of which would be much easier to trace using an in-house application in MATLAB. Figure 3.2.2b compares the sonication series of 2.1 μM (left) and 0.4 μM (right) α-synuclein fibrils. There appears to be little difference between the two sets of images as fibrils still appear too densely packed for subsequent tracing. Therefore, *de novo* α-synuclein fibrils were diluted once more to 0.2 μM (Fig 3.2.2c). Fibrils still appear highly concentrated but due to time constraints and Covid-19 lockdown restrictions, further dilution was not performed.

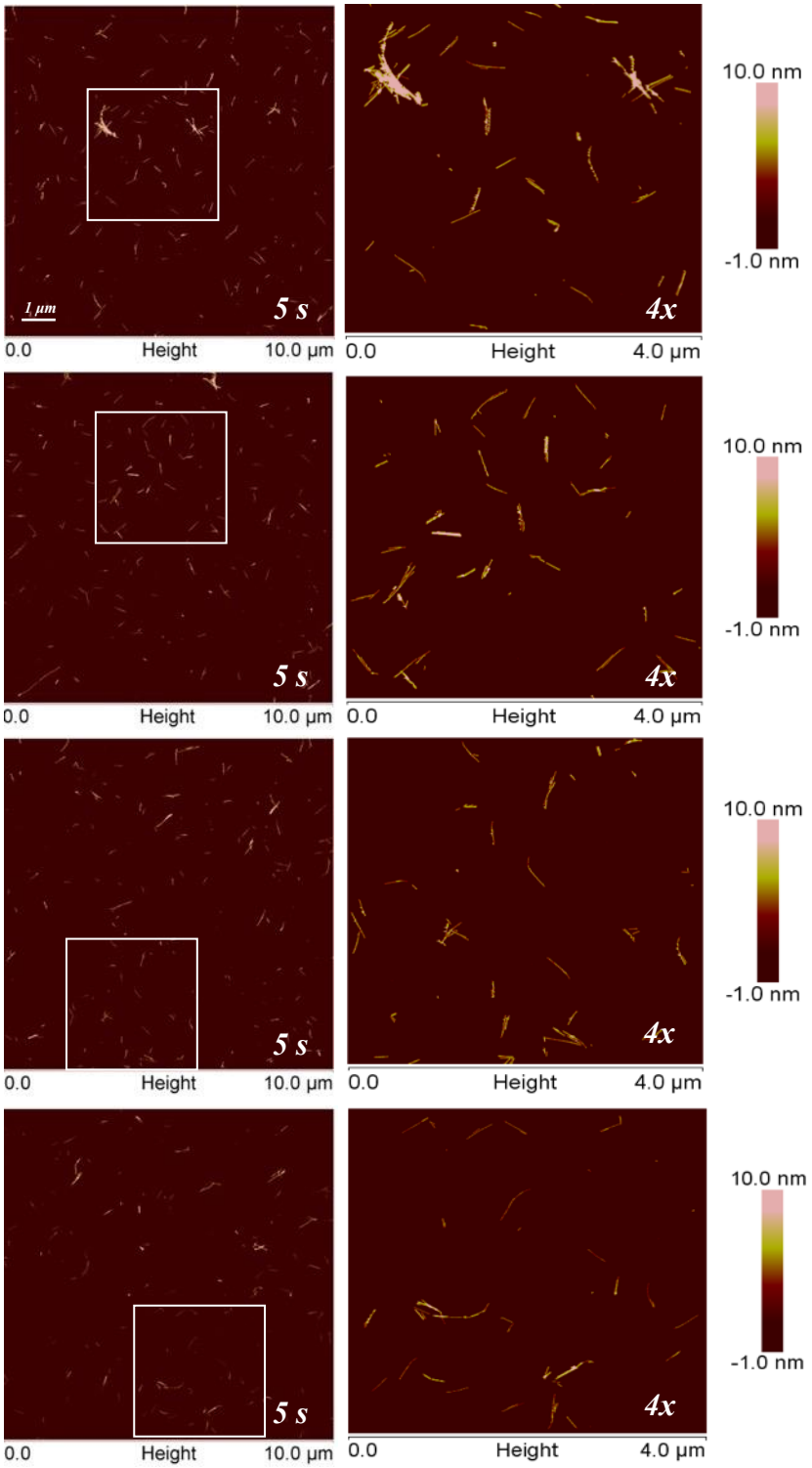

Figure 3.2.2a- AFM images of α-synuclein amyloid fibrils pulse sonicated for 5 seconds. *Fibril samples produced de novo using 2.1 µM monomeric α-synuclein that was pulse sonicated for 5 seconds at an amplitude of 20%. The images are 10 µm x 10 µm in scan size at a resolution of 1024 x 1024 pixel. This size is represented by the scale bar. The height bar shows a range from -1 nm to +10 nm with respect to the mica surface.*

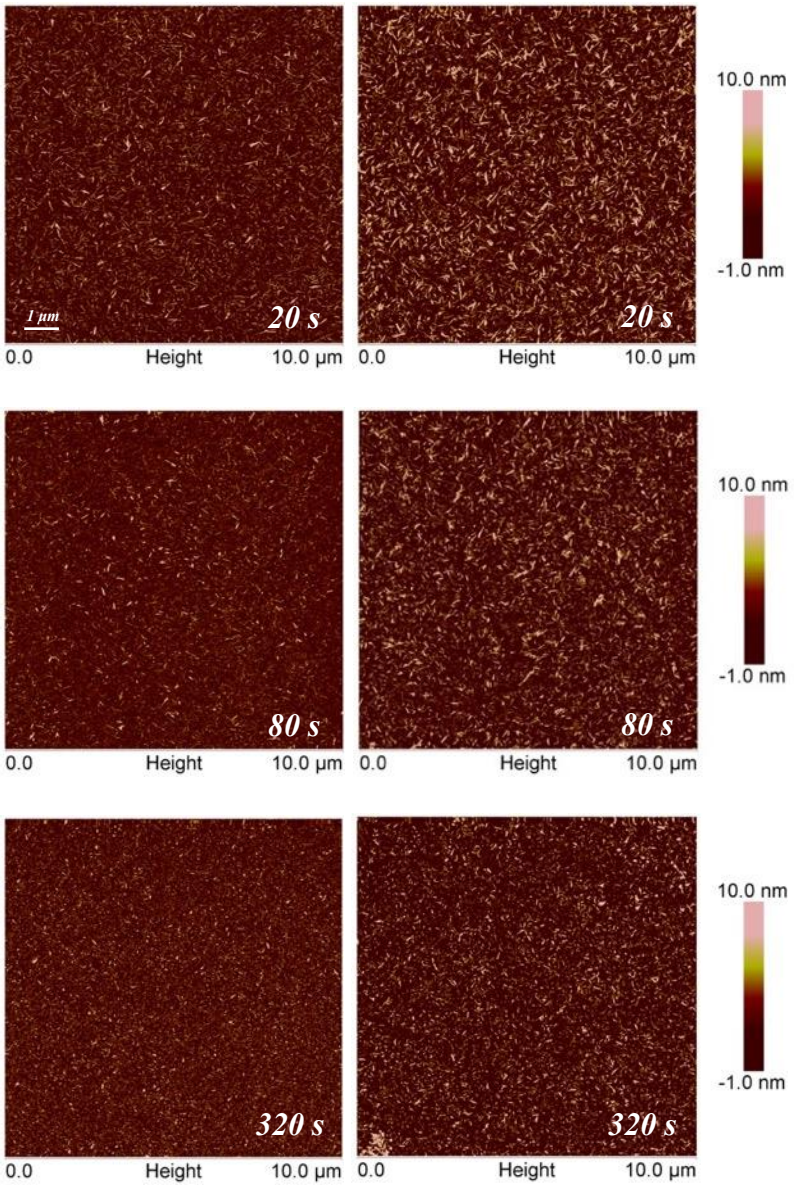

Figure 3.2.2b- α-synuclein fragmentation assay*. Series of AFM images showing different concentrations of α-synuclein fibrils that underwent successive fragmentation by pulse sonication (5 seconds on followed by 5 seconds off) at an amplitude of 20%. 20 µL of sample was removed after each time point (20, 80 and 320 seconds of total sonication time, not including resting time) to be imaged by AFM. The concentration of α-synuclein in the left series of images is 2.1 µM and 0.4 µM in the right series. All images are 10 µm x 10 µm in scan size at a resolution of 1024 x 1024 pixel. This size is represented by the scale bar. The height bar shows a range from -1 nm to +10 nm with respect to the mica surface.*

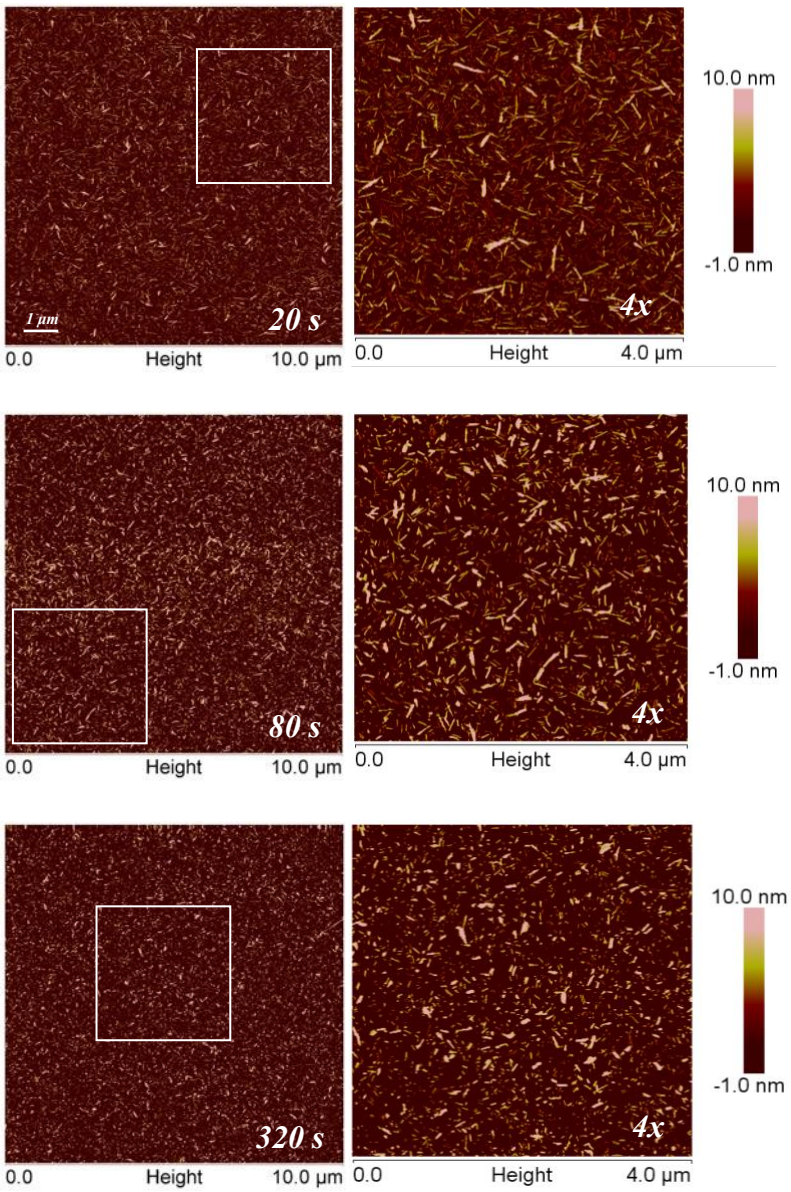

Figure 3.2.2c- 0.2 µM α-synuclein fragmentation assay*. Series of AFM images of fibrils produced de novo using 0.2 µM monomeric α-synuclein that underwent successive fragmentation by pulse sonication (5 seconds on followed by 5 seconds off) at an amplitude of 20%. 20 µL of sample was removed after each time point (20, 80 and 320 seconds of total sonication time, not including resting time) to be imaged by AFM. All images are 10 µm x 10 µm in scan size at a resolution of 1024 x 1024 pixel. This size is represented by the scale bar. The height bar shows a range from -1 nm to +10 nm with respect to the mica surface.*

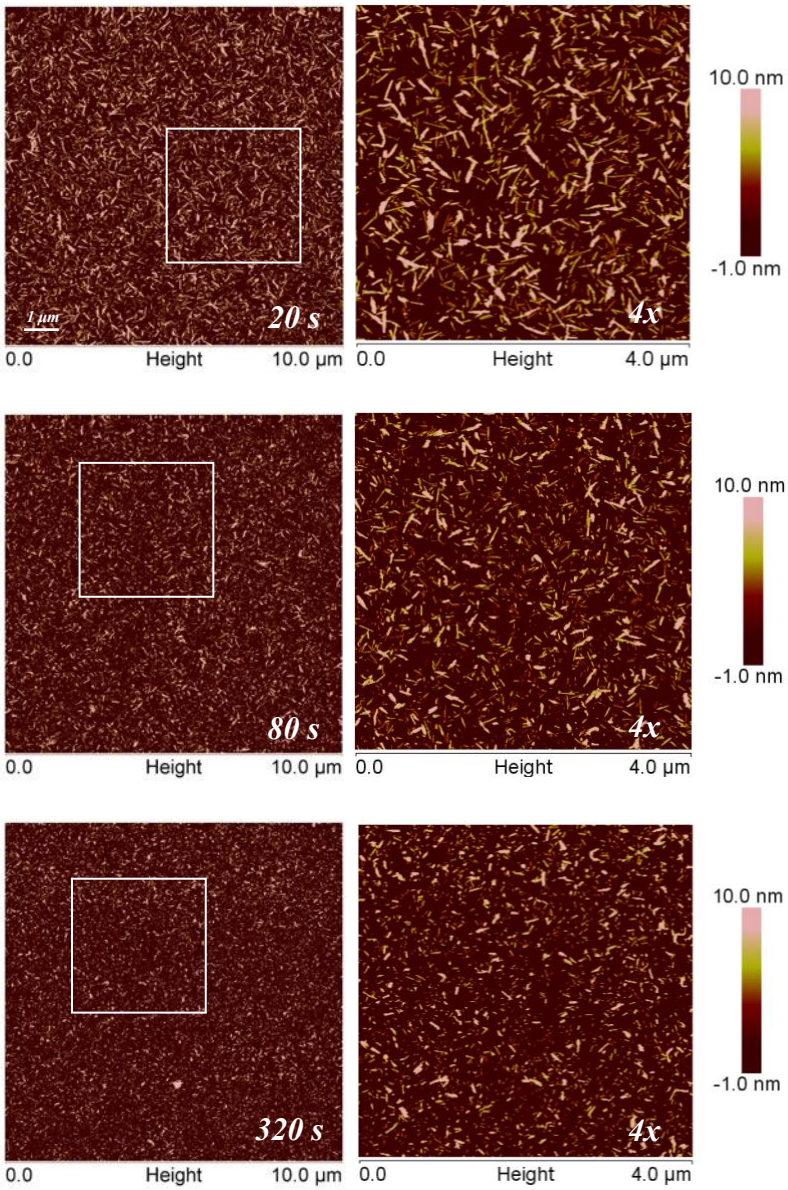

Figure 3.2.2d- Repeat of the 0.2 µM α-synuclein fragmentation assay*. Series of AFM images of fibrils produced de novo using 0.2 µM monomeric α-synuclein that underwent successive fragmentation by pulse sonication (5 seconds on followed by 5 seconds off) at an amplitude of 20%. 20 µL of sample was removed after each time point (20, 80 and 320 seconds of total sonication time, not including resting time) to be imaged by AFM. All images are 10 µm x 10 µm in scan size at a resolution of 1024 x 1024 pixel. This size is represented by the scale bar. The height bar shows a range from -1 nm to +10 nm with respect to the mica surface.*

3.3 Quantitative analysis of the α-synuclein fibril length and height distributions

3.3.1 Size distribution of the α-synuclein amyloid fibril sample

In order to resolve the size change of the α-synuclein amyloid particles in absolute length units, length distribution analysis on the α-synuclein fibril samples was performed by measuring the length of individual particles using the AFM images in section 3.2. The AFM image data was subsequently used to estimate the particle widths (mean particle heights) and particle lengths for each individual fibril. A total of 14 images were collected and analysed for 5 α-synuclein samples, with at least two images and 200 amyloid particles analysed per sample (Table 3.3.1a). The fibrils analysed were randomly selected (Supplementary figures 1-5 and table 1).

Increased time of mechanical perturbation by sonication generally results in reduced mean amyloid particle length. This trend is clearly displayed in the mean length vs. time plot and corresponding log-log plot (Fig 3.3.1), as well as the length distributions (Fig 3.3.2) and AFM images (Fig 3.2) which display an increasing number of increasingly shorter amyloid particles when samples were subjected to longer periods of sonication time. A T-test comparing all sonicated α-synuclein fibril samples to the non-sonicated sample confirms this trend (Table 3.3.1b). All p-values are below 0.05 therefore the difference in amyloid particle length is statistically significant. However, the mean particle length after 5 seconds of sonication shows a significant increase which is likely due to the low sample size and bias in image sampling (Table 3.3.1a). But overall, the data appears to support the findings by Xue et al., 2009. The γ constant determined by the slope of the straight line in the log-log plot provides further information on the division rate of fibrils. For example, $\gamma = 1$ suggests the fibril division rate only depends on the number of available division sites along the fibril, which is linearly dependent on the number of monomers and fibril length. However, $\gamma = >1$ indicates the division rate for fibril types including α-synuclein is highly dependent on fibril length (Beal et al., 2020). The latter is likely to be true for the α-synuclein fibrils studied in this investigation because the

γ value was estimated to be 7.7 using equations m = - 1/γ and y = - 0.13*x + 2.3, which is significantly larger than 1. The relationship between the slope of the line and γ also suggests that for any fibril type under certain conditions, the mean length and length distribution will reduce over time as fibrils divide but the shape of the distribution as function of time will remain the same (Beal et al., 2020). This 'self-similar length distribution' is true for the α-synuclein fibril fragmentation series in this investigation but a greater sample size is required to support this conclusion.

On the other hand, the mean amyloid particle height (width) remains unchanged when sonication time is increased. Both the height distributions (Fig 3.3.2) and the mean height decay data (Fig 3.3.1) shows no clear trend, suggesting mechanical perturbation does not generate new polymorphs, as expected. The results therefore confirm that mechanical perturbation only has a significant effect on amyloid particle length but not on individual fibril assemblies.

Table 3.3.1a - Quantitative analysis of the α-synuclein amyloid fibril samples. *AFM image data analysis statistics for characterised α-synuclein amyloid fibrils.*

Sample	**Fragmentation**	**AFM image analysis**			
	Sonication time/s	**Number of images**	**Number of fibril particles**	**Mean amyloid particle length/nm with SEM**	**Mean amyloid particle height/nm with SEM**
De novo	0	4	200	180.3 ± 7.6 nm	5.6 ± 0.06 nm
5s	5	4	200	233.2 ± 7.1 nm	5.1 ± 0.05 nm
20s	20	2	200	139.2 ± 3.7 nm	4.8 ± 0.09 nm
80s	80	2	200	119.6 ± 2.4 nm	5.3 ± 0.08 nm
320s	320	2	200	95.1 ± 1.8 nm	6.0 ± 0.11 nm

Table 3.3.1b - Statistical analysis for all sonicated α-synuclein fibril samples vs. the non-sonicated α-synuclein fibril sample. *The T-test comparing the sonicated α-synuclein fibril samples to the non-sonicated α-synuclein fibril sample confirms whether changes in amyloid particle length and width are statistically significant. A p-value below 0.05 suggests differences are statistically significant.*

Sample	**p-value**	
	Mean amyloid particle length	**Mean amyloid particle height**
5s	5.56×10^{-07}	1.22×10^{-07}
20s	2.32×10^{-06}	3.98×10^{-11}
80s	6.84×10^{-13}	3.16×10^{-3}
320s	2.01×10^{-22}	2.52×10^{-4}

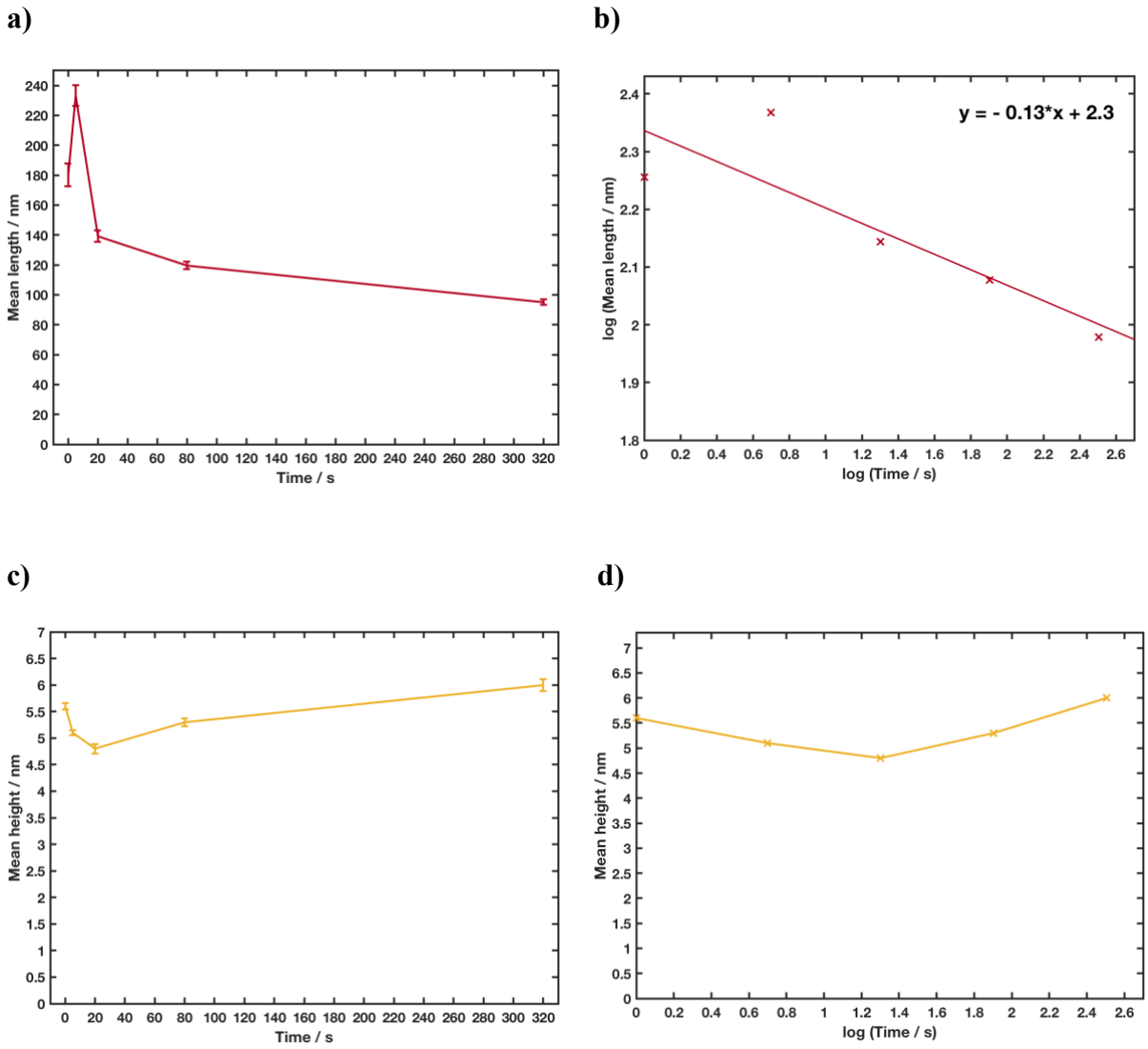

Figure 3.3.1- α-synuclein fibril length and height decay data extracted from table 3.3.1a. *(a) graph of the decay of mean fibril length during fragmentation by pulse sonication under increasing length of time. (b) log-log plot of mean length vs. time with the slope of the line representing - 1/γ where the constant γ describes the fibril length dependence of the division rate constant, as reported in Beal et al., 2020. (c) graph of the decay of mean fibril height (indicative of fibril width) during fragmentation by pulse sonication under increasing length of time. (d) log plot of mean height vs. time.*

3.3.2 Fibril length

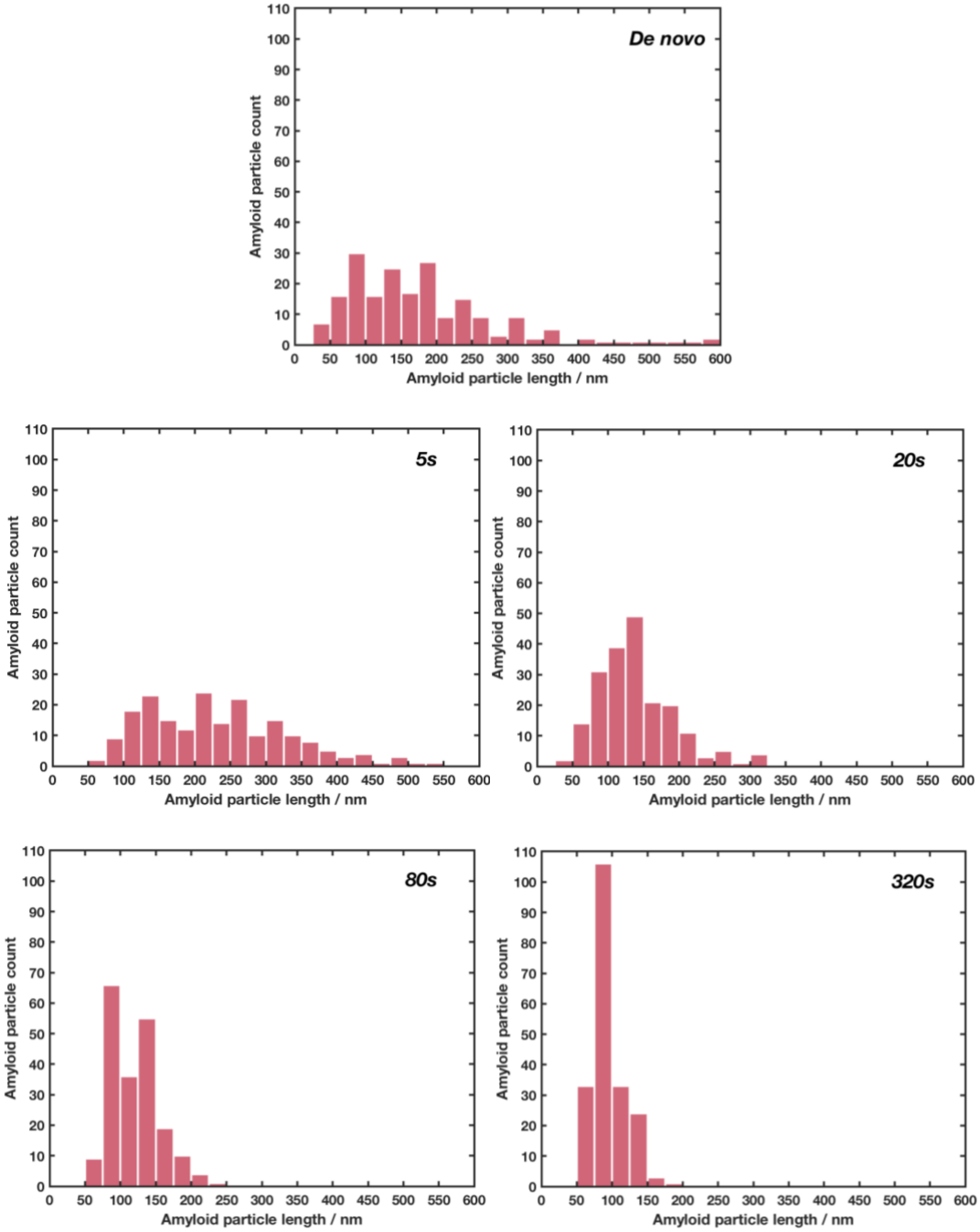

Figure 3.3.2- The length distribution of each α-synuclein fibril sample. *The amyloid particle size distributions represent 5 α-synuclein samples (De novo, 5s, 20s, 80, 320s) sonicated for different lengths of time which are displayed in each plot. The particle length (red bars) is plotted against the amyloid particle count (total = 200) in each sample.*

3.3.3 Fibril width

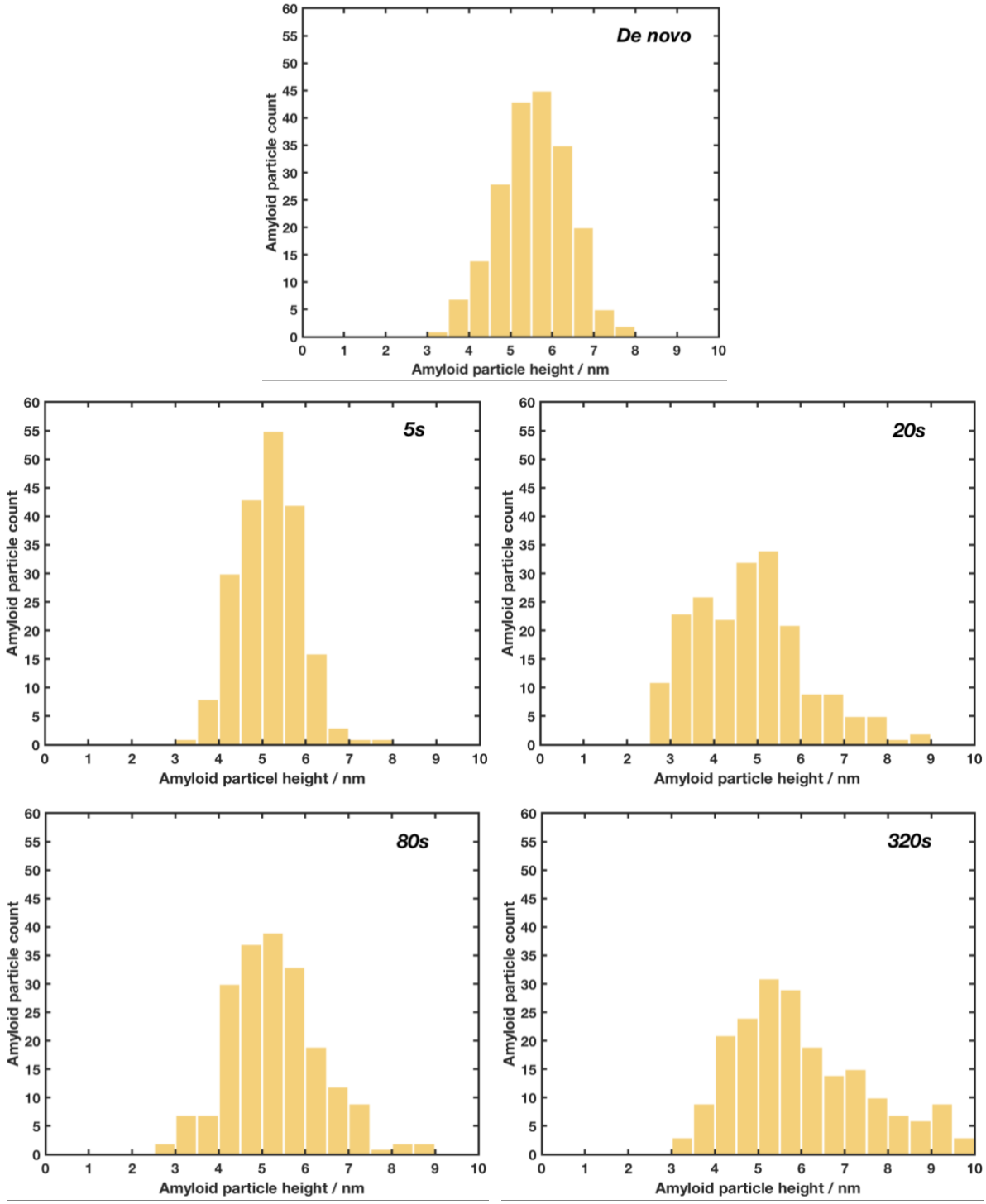

Figure 3.3.3- The height distribution of each α-synuclein fibril sample. *The particle size distributions represent 5 α-synuclein samples (De novo, 5s, 20s, 80, 320s) sonicated for different lengths of time which are displayed in each plot. The mean particle height (width) (yellow bars) is plotted against the amyloid particle count (total = 200) in each sample.*

Both the AFM images and the length and height distribution plots suggest *de novo* (non-sonicated) α-synuclein amyloid fibrils form large fibril networks that do not accurately reflect the length and width of the fibril population, possibly due to the low sample size and some bias. The length of non-sonicated fibrils ranges from 39.3 – 579.0 nm (Supplementary table 1). This sample exhibits the greatest variation in fibril dimensions where the highest number of fibrils were observed between 75 – 100 nm long (Supplementary table 2). In fact, the length of 70% of the fibrils was measured to be under 200 nm with increasingly fewer fibrils observed with a greater length. Reduction in length distribution was observed as length of sonication time was increased, suggesting sonication generates fibrils of apparently more uniform lengths (Fig 3.3.2). For example, after 5 seconds of sonication, the range of lengths was decreased by 15% to 68.7 – 528.1 nm and the greatest number of fibrils was observed with a length between 200 – 225 nm instead. After 20 seconds of sonication, the range was even lower at 39.3 – 315.5 nm, a 48.3% decrease from the non-sonicated sample. The length of 88% of the fibrils were measured to be under 200 nm with the majority being 125-150 nm long. The range continues to drop after 80 seconds of sonication to 58.9 – 245.4 nm, a 65% decrease. However, similarly to the non-sonicated sample, the majority of fibrils were 75 – 100 nm long. The same trend was observed for the 320s sonicated sample where 53% of fibrils were 75 – 100 nm long. The range was even smaller, 58.8 – 176.8 nm, a 78% decrease from the *de novo* sample. The sonication however did not have a significant effect on the width of α-synuclein fibrils, only a subtle increase in height distribution (Fig 3.3.3) which is likely due to experimental variations.

Chapter 4 DISCUSSION

4.1 Role of fibril fragmentation in amyloid cytotoxicity

It is evident from the growing research conducted over the past decade that amyloid and prion proteins perturb cellular processes which are consequently associated with fatal neurodegenerative disorders and systemic amyloidosis. This thesis has summarised some important aspects of the current understanding of amyloid structure, formation, toxicity, as well as crucial biological functions in several different organisms. But despite the rapid progression in this field, many aspects of amyloid diseases are highly nuanced. For example, a growing number of diseases are associated with amyloid proteins with prion-like properties where amyloid particles can transmit into nearby healthy cells to effectively propagate by a prion-like mechanism i.e. recruit non-prion soluble proteins into insoluble amyloid fibrils (Bousset et al., 2020). As mentioned in section 1.1.7, transmissible amyloid proteins include Aβ, α-synuclein, tau and huntington, whereby cell-to-cell transmission occurs by diffusion across the cellular membrane via interaction with a number of active protein import and export mechanisms (Marchante et al., 2017). These findings confirm that the binary prion/non-prion view does not sufficiently explain the difference between transmissible and non-transmissible amyloid. Rather, the transmissibility of amyloid is a much more complex biological property, one that is likely to be a general trait of all amyloid species under the appropriate physical properties and environmental conditions. This underlying question has formed the basis of this research project, that is, to better understand how the mesoscopic and suprastructural properties of amyloid particles affect their biological activities such as their cytotoxic and infectious potentials. This will ultimately determine whether they are biologically functional and provide insight into why some amyloid proteins are associated with devastating human diseases. As described in section 1.4.4, fibril fragmentation is an important step in the amyloid/prion life-cycle, the rate of which is linked to pathogenicity because it results in the exponential growth

in the number of amyloid particles (Beal et al., 2020). Moreover, it has also been observed that daughter particles generated from the fragmentation of parent fibrils lead to a reduction in the overall size distribution as fragmentation proceeds either by mechanical perturbation by sonication, enzymatic action or other cellular or environmental perturbations (Beal et al., 2020). These two findings are likely to be a key determinant in the overall cytotoxic and infectious potentials of disease-associated amyloid. Thus, the stability of amyloid fibrils towards fragmentation, indicative of fibrils' resistance towards fragmentation, may be a good indicator of the fibrils' pathogenicity. This notion initially lead to the selection of two amyloid forming protein model systems, Sup35NM and α-synuclein, which generated their respective prion and prion-like amyloid fibrils. Results would've allowed a direct comparison between structural changes. However, due to unforeseen circumstances presented by the Covid-19 lockdown, sufficient data was only collected and analysed for α-synuclein. Therefore a comparison between fragmentation rates and thus level of cytotoxicity, as initially intended, could not be made, but will constitute an important future goal for this avenue of research.

4.2 Preparation of Sup35NM amyloid fibrils

Sup35 is a functional prion protein found in *Saccharomyces cerevisiae.* The loss-of-function phenotype, *[PSI+]*, is known to play a crucial role in tRNA-mediated suppression of nonsense mutations, resulting in the synthesis of a functional polypeptide. As described in section 1.1.6, although Sup35 comprises of 685 amino-acid residues with three distinct domains, the N-terminal domain is sufficient for *[PSI+]* occurrence and maintenance. Interestingly, the protein remains soluble in *[PSI+]* cells even when the N-terminal domain is deleted (Bousset et al., 2020). The M-domain (residues 124–253) is also important for *[PSI+]* propagation because the highly charged residues modulate the solubility of non-prion Sup35. The two constructs investigated in this study are the truncated versions Sup35NM (residues 1–253), bearing either

N- or C-terminal poly-histidine tags. Initially, Sup35NM with C-terminal poly-histidine tags was prepared because this construct was known to produce higher quality filaments and data set. The monomeric protein was produced by inducing its expression in modified *E. coli* cells which were transformed by the pET3a plasmid containing the Sup35NM C-terminal Hexa-His gene (section 2.1.1). Following successful expression, the cells were lysed by sonication and the monomeric protein was extracted and purified under denaturing conditions (section 2.3). The elute obtained from size exclusion chromatography was confirmed to be purified via SDS-PAGE analysis (Fig 3.1.2) and was stored at -80 ºC for future fibril-forming reactions. Next, after some trial and error, the suitable conditions were determined under which to form *de novo* amyloid fibrils which were subsequently prepared for imaging by AFM. Unfortunately, fibrils were not visible when initially imaged, even when the expression and purification was repeated several times to obtain a higher protein concentration. The poor results were possibly due to errors during protein preparation, fibril deposition on mica when preparing samples for AFM, or not spending sufficient time searching for fibrils during AFM imaging. Since fibrils could not be confirmed by AFM imaging, fibril fragmentation by sonication was not performed as initially intended to test the fibril stability.

Following the Covid-19 lockdown, subsequent AFM imaging and analysis was conducted on purified Sup35NM with N-terminal poly-histidine tags provided by Tracey Purton. Interestingly, although it is well established that the Sup35NM domain is critical for *[PSI+]* formation and maintenance, recent studies have shown the driving force for fibril formation and the structural characteristics of the fibrils depends on the location of the His-tag. It is reported that Sup35NM bearing a His-tag on the N-terminal end is structurally similar to the untagged Sup35NM. The N-terminal poly-His tag therefore only marginally alters the structure of untagged Sup35NM fibrils. However, when the His-tag is placed on the C-terminal end of

the protein, the NM fibril structure drastically changes with an increased infectious potential compared to the untagged Sup35NM N-terminal counterpart (Bousset et al., 2020). One explanation why Sup35pNM-His construct induces *[PSI+]* formation with a greater efficiency is that it consists of several different polymorphs, a greater number of which have more potent seeding capacity than the His-Sup35pNM counterparts. Moreover, the structural heterogeneity of Sup35pNM-His may be more compatible with the Sup35pNM folding landscape. This may facilitate growth of fibrillar Sup35pNM-His by recruitment of Sup35NM monomers and possibly yielding fibrils that are more susceptible to fragmentation which in turn would generate more short fibrils increasing *[PSI+]* induction (Bousset et al., 2020).

4.3 The α-synuclein amyloid model system

α-synuclein is a prion-like amyloid protein associated with Parkinson's disease, a fatal neurogenerative disorder which affects approximately 10 million people worldwide. As mentioned in section 1.2.2.3, monomeric α-synuclein is intrinsically disordered but plays an important role in vesicle trafficking at low concentration within the presynaptic region of neurons. It is thought that exceeding a critical concentration increases misfolding of the protein, which in turn increases the likelihood of aggregation and formation of intracellular inclusions comprising of β-sheet rich polymers assembled into various oligomers or larger amyloidogenic fibrils. Interestingly, α-synuclein isolated from intracellular inclusions often harbours extensive post-translational modifications such as phosphorylation, truncation, ubiquitination, nitration, sumoylation, and several others (Sorrentino and Giasson, 2020). Misfolding and aggregation ultimately leads to neuronal toxicity and dysfunction as the disease progresses in a prion-like manner. The idea that α-synuclein has prion-like properties was first suggested when PD patients who had fetal stem cell grafts placed into their brains developed intracellular α-synuclein inclusions within the grafts, indicating a "spread" of pathology (Brundin and

Melki, 2017). Moreover, early *in vitro* observations also demonstrated that the addition of α-synuclein seeds to a solution of monomeric α-synuclein could induce fibril growth by templated elongation where free monomers are converted to the same β-sheet conformation and added to growing filament ends. This process of conformational templating further confirms the prion-like properties of α-synuclein. For these reasons, α-synuclein was the second model system selected for study in this project because like Sup35NM, α-synuclein is known to produce quality filaments (which can be easily imaged by AFM) and data set which would not only provide insight into the difference between functional and disease associated amyloid but also allow comparison between prion and prion-like species. This comparison was not possible in the end since Sup35NM N-terminal fibrils could not be imaged in time due to Covid-19 lockdown restrictions. Nonetheless, the lengths of single α-synuclein amyloid particles sonicated at various lengths of time were quantitatively determined by AFM image analysis, allowing the systematic investigation of the length distribution of different samples.

4.4 Fibril fragmentation and stability

It is established that fragmentation of amyloid fibrils is one of the most important stage in the propagation of the amyloid conformation because fibril fragmentation is essentially the replication step in the amyloid lifecycle which not only drives the proliferation of amyloid species but also regulates the biological role (Beal et al., 2020). The stability of fibrils is influenced by their suprastructural properties, such as clustering, width distribution, and length distribution, which in turn depends on their precise atomic structure. Therefore, in order to understand how the mesoscopic level structural properties of α-synuclein influence the tendency of fibrils towards fragmentation, fibrils were analysed before and after mechanical perturbation by pulse sonication at 20 kHz and 20% amplitude for exponentially increasing periods of time. Sonication was initially intended for both Sup35NM N-terminal and α-

synuclein fibril types to allow more controlled fragmentation to facilitate an easier comparison between amyloid particles of both systems and quantify differences in stability of functional and disease-associated fibrils. However, the sonication series was only completed for α-synuclein where results from the fragmentation series suggest the structural properties of fibrils are likely to impact its biological role. In order to confirm this, the α-synuclein data set can be compared to other systems in future experiments.

4.4.1 Fragmentation of Sup35NM fibrils

Figure 3.1.4 shows how sonicated and non-sonicated N-terminal Hexa-His tagged Sup35NM fibrils vary. Both samples were difficult to image by AFM because fibrils were extremely dispersed and alongside time constraints, only one image of each sample was obtained. Due to the low sample size, it is difficult to accurately analyse the change in suprastructural properties. One possible explanation for the large dispersion is that fibrils were aggregated in large clusters or bundles in an area of mica that was not scanned. Some small bundles are observed in the non-sonicated sample whereas a large cluster is visible in the sonicated sample. The fibrils found in bundles and clusters are thought to be relatively inert, and thus less infectious compared to their less aggregated counterparts (Marchante et al., 2017). The reduced activity of Sup35NM particles is likely to be linked to the stability of these fibrils, which in turn may be influenced by the function of the system. As suggested in section 1.2.3, functional amyloid are typically more stable than disease-associated amyloid because they exist to serve a crucial function which requires a high level of stability in order to achieve a prolonged effect until that function is no longer required. This is true for the majority of functional amyloid examples mentioned in this thesis where aggregation is carefully controlled by a combination of chemical modifications and biochemical changes in the cellular environment such as in temperature, pH conditions, and exposure to various solvents and metal ions. Loss of stability would therefore

reduce their functionality by increasing the number of fibrils or oligomeric species that would normally be carefully contained by protein compartmentalisation. As mentioned in section 1.2.2, an accumulation of amyloid fibrils or oligomers generally has a negative impact on cell proteostasis, potentially leading to cell death and tissue damage which often manifests as fatal neurodegenerative disorders if accumulation occurs in the brain. However, Sup35NM is unique to the functional amyloid examples presented in section 1.2.3 because as a prion, its function depends on its transmissibility which in turn is influenced by a high fragmentation rate. This notion explains why *de novo* Sup35NM fibrils (Fig 3.1.4) appear much shorter compared to *de novo* α-synuclein fibrils (Fig 3.2.1) and even the sonicated α-synuclein fibrils (Fig 3.2.2a). Thus, despite the incomplete fragmentation series for Sup35NM, it can be assumed that Sup35NM fragments at a higher rate than α-synuclein due to the presence of significantly shorter *de novo* amyloid particles. The high fragmentation rate of Sup35NM is crucial for the propagation of the prion conformation because it generates more reactive fibril ends for elongation and subsequent fragmentation into smaller amyloid particles that are capable of transferring between cells. Therefore, functionality would decrease if stability was to increase, the opposite of which would be expected for amyloid with structural or storage roles. The results therefore confirm that Sup35NM is less stable than α-synuclein due to its role as a functional prion. The functionality would also cause Sup35NM to generate a high aggregate yield quickly, possibly resulting in the formation of large clusters and bundles such as those observed in Fig 3.2.1.

4.4.2 Fragmentation of α-synuclein fibrils

α-synuclein fibrils were much easier to visualise due to increased concentration in comparison to Sup35NM (2.1 μM vs 0.1 μM, respectively) and increased incubation temperature (37°C vs 30°C). The increased concentration was not intended, but due to a miscalculation in the initial

sample concentration after the protein was collected from the PD-10 column. However, since the rate of fibril fragmentation is not known to be influenced by concentration, the error can be overlooked and comparison between the Sup35NM N-terminal fibril sample is still possible. The need for increased incubation temperature and 180 rpm shaking suggest that *de novo* growth of α-synuclein is considerably slower than that of Sup35NM under standard laboratory conditions, possibly because the α-synuclein primary nuclei form less readily. Forming *de novo* α-synuclein and Sup35NM N-terminal fibrils under the same conditions was not attempted due to time constraints but the task is unlikely to be successful because the fast aggregation rate of Sup35NM is possibly linked to its functional role as a prion. By definition (section 1.1.4), prions have evolved to have a higher fragmentation rate than amyloid in order to maximise the number of potential seeds generated to facilitate effective propagation of the prion conformation. One clear observation from the *de novo* α-synuclein sample is that fibrils appear more bundled compared to the *de novo* Sup35NM fibril sample, and have been suggested to be like a ribbon structure (Makky et al., 2016). Although these bundle structures have been shown previously, they are more likely to occur as a result of the higher concentration of α-synuclein fibrils prepared for imaging by AFM. Compared to the sonicated Sup35NM sample, fewer bundles of α-synuclein are visible after 5 seconds of sonication but despite the higher concentration, no large clusters were observed. In fact, clusters were not observed in any of the α-synuclein samples. This immediately suggests that α-synuclein fibrils are more active than those of Sup35NM and hence the full-length Sup35 prion. The fragmentation series for α-synuclein (Fig 3.2.2) did however impact the amyloid particle length distribution (Fig 3.3.2). The main effect of sonication was a clear decrease in the mean amyloid particle length (table 3.3.1a) and an increase in the number of amyloid particles (Fig 3.2.1 and 3.2.2a-c). This relationship is confirmed by further statistical analysis whereby a T-test was performed, providing final p-values < 0.05 which suggest the differences in the morphology of sonicated

vs. non-sonicated fibrils are statistically significant (Table 3.3.1b). The decay in fibril length with time is also seen on the log-log plot of mean fibril length vs. time (Fig 3.3.1). The plot follows a straight line which indicates a self-similar length distribution that is achieved (section 3.3.1), confirming the linear relationship between fibril length and sonication time (Beal et al., 2020). Fibrils also appear to have become more homogenous in length as length of sonication time is increased, as evident by a decrease in the range of lengths observed. However, fibrils don't become more homogenous because the pattern of distribution is not changed, only the mean length. There is little difference between the *de novo* and 5s sonicated length distribution plots, only a slight increase in the range of lengths within the 5s sonicated sample population. One reason why fewer fibrils shorter than 50 nm are shown in all samples is because short fibrils were much more difficult to accurately trace even though many were present. As a result, the length distribution plots do not accurately reflect the length of all fibril populations. This drawback can be overcome by further reducing the fibril concentration and manually measuring a greater number of fibrils within a random *10 μm x 10 μm* area of the mica, or using a tracing software which automatically measures the lengths of all fibril within an even larger area of mica. Nonetheless, the current data set can also be used to determine the structural characteristics of each fibril population. For example, the presence of short fibrils (<50nm) observed in the *de novo* α-synuclein sample suggests some degree of fragmentation has occurred as fibrils elongate without disturbance (agitation). This further confirms that both mechanisms occur simultaneously during the amyloid life cycle as described in section 1.4.1.

On the other hand, sonication appears to have no clear effect on the fibril width (Fig 3.3.1-2), confirming that no new fibril polymorphs were generated during the fragmentation series. The results therefore confirm that the physical consequences of fibril fragmentation are a reduction in the surface area parallel to the long axis of each fibril as demonstrated by the shortening of

fibrils, and an increase in the total surface area of fibril ends as demonstrated by the greater number of fibrillar particles. Several studies have reported that the primary cause of toxicity in amyloid disease depends critically on the amyloid fibril length, without the occurrence of parallel changes in their molecular structure or chemical composition (Beal et al., 2020; Marchante et al., 2017; Xue et al., 2009). Although end stage fibrils are generally considered relatively inert compared to short prefibrillar oligomers, some studies have suggested various different mechanisms of fibril-associated cytotoxicity: (1) the process of fibril formation may cause cytotoxicity; (2) the fibrils themselves may be the cytotoxic species because they serve as a source of prefibrillar cytotoxic oligomers that are released upon depolymerisation caused by interaction with lipids (Carulla et al., 2005; Martins et al., 2008). Nonetheless, fibril fragmentation remains a crucial aspect of amyloid disease because the physical dimensions have previously been shown to be an important parameter in defining the infective potential of amyloid particles (Marchante et al., 2017). In terms of Sup35NM, it has been demonstrated that individual prion particles above 200 nm in length have a greater tendency to interact and form higher-order aggregate superstructures in the form of fibril clusters and networks, and are therefore considered non-infectious because they cannot diffuse through the cellular membranes to infect new cells. However, successful infection also relies on interactions with intracellular factors such as chaperones, co-chaperones and the proteostasis machinery. Therefore, inability to cross cell membranes may also result from lack of interaction with the propagation machinery. Additionally, the infectivity of amyloid particles shorter than 200 nm is largely dependent on particle concentration, their diffusion properties, and interactions with other cellar components in the cytosol, with membranes, and other surfaces.

4.5 Conclusions and further research

In conclusion, fragmentation by sonication has been shown to have a significant effect on the physical characteristics of Sup35NM N-terminal and α-synuclein fibrils such as reduction in the average fibril length. The results also confirm an increase in the number of fibril extension sites with increased sonication, thereby increasing the biological availability of fibrillar material and the likelihood of interaction with cellular membranes, enhancing the cytotoxic potential. Moreover, reduction in overall fibril size also enhances diffusion by increasing fibril-membrane surface interactions and/or reducing fibril-fibril interactions within large fibril clusters and networks. Increased biological availability and surface activity of short fibrils in turn increases the likelihood of internalisation of fibrils by cells and their infective potential. These findings suggest that strategies to promote elongation of short prefibrillar amyloid particles into large, non-transmissible superstructures might prevent prion-like transmission and therefore delay the progression of amyloid disease, particularly for Parkinson's disease because although α-synuclein is heavily researched, its infective potential is still unknown.

Given the importance of small diffusible amyloid particles and their infectious potential, one direction for future work could be to calculate the size threshold for effective transmission activity of other prions and prion-like amyloid structures such as α-synuclein and amyloid-β. Amyloid-β is considered more cytotoxic due to a higher tendency towards fragmentation. Therefore, comparing suprastructural properties, such as clustering, bundling, twist, stiffness, width and length distribution, may provide insight into the mechanisms controlling the rate of fragmentation, and therefore transmission of different amyloid particles. This will ultimately help devise the most effective therapeutic strategy to combat progression of individual amyloid diseases. Moreover, comparison with more systems will also allow the identification of the general factors influencing the amyloid/prion lifecycle. It is therefore important to continue

direct comparisons between functional and disease associated amyloid/prions to understand how biological adaptations may have influenced their characteristics. As mentioned in section 4.2, the location of the poly-histidine tags drastically changes the Sup35NM fibril structure (Bousset et al., 2020). Therefore a comparison between different Sup35NM constructs will also prove to be valuable in revealing the effects of poly-histidine tags on the infective potential of specific constructs. On the other hand, comparison between Sup35NM and full-length Sup35 will provide greater insight into the effects of the C-terminal domain on the whole protein.

In order to make a fair comparison between data sets, it is important to have a large sample size so that the analysis is more reliable and representative of the whole fibril population. This can be achieved by collecting more AFM images of each protein sample in order to trace a greater number of fibrils, possibly several thousand in each sample. One way to improve the quality of tracing would be to use a fibril tracing algorithm to measure the physical dimensions of as many fibrils as possible within a given area of mica scanned. This will not only provide a large sample size but also remove bias in choosing which fibrils to trace. Both outcomes will make the results more representative of the fibrils within each sample, making the analysis more accurate. Higher quality tracing will also allow a more accurate comparison between fibril widths, making it easier to identify any new polymorphs.

Lastly, *in vivo* fibril fragmentation is also influenced by chemical, thermal, or enzymatic action by molecular chaperones Hsp104 or ClpB. Therefore, another area of research could be to measure the effects that varying these conditions will have on the formation and fragmentation rate of different fibril types. One way to test whether stability towards fragmentation depends on the cellular environment is to use different salt concentrations or temperature at which fibrils are incubated at before preparation of AFM samples. In addition, other forms of mechanical

perturbation such as shaking and stirring can also be used to test their effect on different fibril types because the stability of some fibrils may vary depending on the nature of the perturbation. Finally, understanding how molecular chaperones promote amyloid fragmentation, degradation and/or propagation of the amyloid conformation is also important in resolving how physiological changes may influence the complex behaviour of the amyloid lifecycle.

REFERENCES

1. Arosio, P., J. Knowles, T.P., Linse, S., 2015. On the lag phase in amyloid fibril formation. Phys. Chem. Chem. Phys. 17, 7606–7618.
2. Aubrey, L.D., Blakeman, B.J.F., Lutter, L., Serpell, C.J., Tuite, M.F., Serpell, L.C., Xue, W.-F., 2020. Quantification of amyloid fibril polymorphism by nano-morphometry reveals the individuality of filament assembly. bioRxiv 2020.01.14.905877
3. Audas, T.E., Audas, D.E., Jacob, M.D., Ho, J.J.D., Khacho, M., Wang, M., Perera, J.K., Gardiner, C., Bennett, C.A., Head, T., Kryvenko, O.N., Jorda, M., Daunert, S., Malhotra, A., Trinkle-Mulcahy, L., Gonzalgo, M.L., Lee, S., 2016. Adaptation to Stressors by Systemic Protein Amyloidogenesis. Dev. Cell 39, 155–168.
4. Ban, T., Hamada, D., Hasegawa, K., Naiki, H., Goto, Y., 2003. Direct observation of amyloid fibril growth monitored by thioflavin T fluorescence. J. Biol. Chem. 278, 16462–16465.
5. Barral, J.M., Broadley, S.A., Schaffar, G., Hartl, F.U., 2004. Roles of molecular chaperones in protein misfolding diseases. Semin. Cell Dev. Biol., Protein Misfolding and Human Disease and Developmental Biology of the Retina 15, 17–29.
6. Batarseh, Y., Duong, Q.-V., Mousa, Y., Al Rihani, S., Elfakhri, K., Kaddoumi, A., 2016. Amyloid-β and Astrocytes Interplay in Amyloid-β Related Disorders. Int. J. Mol. Sci. 17, 338.
7. Baxa, U., Cassese, T., Kajava, A.V., Steven, A.C., 2006. Structure, function, and amyloidogenesis of fungal prions: filament polymorphism and prion variants. Adv. Protein Chem. 73, 125–180.
8. Beal, D.M., Tournus, M., Marchante, R., Purton, T., Smith, D.P., Tuite, M.F., Doumic, M., Xue, W.-F., 2020. The Division of Amyloid Fibrils. bioRxiv 506386.

9. Benilova, I., Karran, E., Strooper, B.D., 2012. The toxic Aβ oligomer and Alzheimer's disease: an emperor in need of clothes. Nat. Neurosci. 15, 349–357.
10. Bousset, L., Luckgei, N., Kabani, M., Gardiennet, C., Schütz, A.K., Melki, R., Meier, B.H., Böckmann, A., 2020. Prion Amyloid Polymorphs – The Tag Might Change It All. Front. Mol. Biosci. 7.
11. Brundin, P., Melki, R., 2017. Prying into the Prion Hypothesis for Parkinson's Disease. J. Neurosci. 37, 9808–9818.
12. Bucciantini, M., Calloni, G., Chiti, F., Formigli, L., Nosi, D., Dobson, C.M., Stefani, M., 2004. Prefibrillar amyloid protein aggregates share common features of cytotoxicity. J. Biol. Chem. 279, 31374–31382.
13. Buell, A.K., Galvagnion, C., Gaspar, R., Sparr, E., Vendruscolo, M., Knowles, T.P.J., Linse, S., Dobson, C.M., 2014. Solution conditions determine the relative importance of nucleation and growth processes in α-synuclein aggregation. Proc. Natl. Acad. Sci. 111, 7671–7676.
14. Burre, J., Sharma, M., Tsetsenis, T., Buchman, V., Etherton, M.R., Sudhof, T.C., 2010. -Synuclein Promotes SNARE-Complex Assembly in Vivo and in Vitro. Science 329, 1663–1667.
15. Buxbaum, J.N., Linke, R.P., 2012. A molecular history of the amyloidoses. J. Mol. Biol. 421, 142–159.
16. Carulla, N., Caddy, G.L., Hall, D.R., Zurdo, J., Gairí, M., Feliz, M., Giralt, E., Robinson, C.V., Dobson, C.M., 2005. Molecular recycling within amyloid fibrils. Nature 436, 554–558.
17. Castle, A.R., Gill, A.C., 2017. Physiological Functions of the Cellular Prion Protein. Front. Mol. Biosci. 4.

18. Chaari, A., 2019. Molecular chaperones biochemistry and role in neurodegenerative diseases. Int. J. Biol. Macromol. 131, 396–411.
19. Chiti, F., Dobson, C.M., 2017. Protein Misfolding, Amyloid Formation, and Human Disease: A Summary of Progress Over the Last Decade. Annu. Rev. Biochem. 86, 27–68.
20. Chiti, F., Dobson, C.M., 2006. Protein Misfolding, Functional Amyloid, and Human Disease. Annu. Rev. Biochem. 75, 333–366.
21. Cho, M.-H., Cho, K., Kang, H.-J., Jeon, E.-Y., Kim, H.-S., Kwon, H.-J., Kim, H.-M., Kim, D.-H., Yoon, S.-Y., 2014. 1775.
22. Chuang, E., Hori, A.M., Hesketh, C.D., Shorter, J., 2018. Amyloid assembly and disassembly. J. Cell Sci. 131, jcs189928.
23. Ciechanover, A., Kwon, Y.T., 2015a. Degradation of misfolded proteins in neurodegenerative diseases: therapeutic targets and strategies.
24. Ciechanover, A., Kwon, Y.T., 2015b. Degradation of misfolded proteins in neurodegenerative diseases: therapeutic targets and strategies. Exp. Mol. Med. 47, e147–e147.
25. Clavaguera, F., Akatsu, H., Fraser, G., Crowther, R.A., Frank, S., Hench, J., Probst, A., Winkler, D.T., Reichwald, J., Staufenbiel, M., Ghetti, B., Goedert, M., Tolnay, M., 2013. Brain homogenates from human tauopathies induce tau inclusions in mouse brain. Proc. Natl. Acad. Sci. U. S. A. 110, 9535–9540.
26. Clavaguera, F., Tolnay, M., Goedert, M., 2017. The Prion-Like Behavior of Assembled Tau in Transgenic Mice. Cold Spring Harb. Perspect. Med. 7, a024372.
27. Cohen, A.S., 1986. General Introduction and a Brief History of Amyloidosis, in: Marrink, J., Van Rijswijk, M.H. (Eds.), Amyloidosis. Springer Netherlands, Dordrecht, pp. 3–19.

28. Cohen, Samuel I A, Linse, S., Luheshi, L.M., Hellstrand, E., White, D.A., Rajah, L., Otzen, D.E., Vendruscolo, M., Dobson, C.M., Knowles, T.P.J., 2013. Proliferation of amyloid-β42 aggregates occurs through a secondary nucleation mechanism. Proc. Natl. Acad. Sci. U. S. A. 110, 9758–63.
29. Cohen, Samuel I. A., Linse, S., Luheshi, L.M., Hellstrand, E., White, D.A., Rajah, L., Otzen, D.E., Vendruscolo, M., Dobson, C.M., Knowles, T.P.J., 2013. Proliferation of amyloid-β42 aggregates occurs through a secondary nucleation mechanism. Proc. Natl. Acad. Sci. U. S. A. 110, 9758–9763.
30. Cremades, N., Dobson, C.M., 2018. The contribution of biophysical and structural studies of protein self-assembly to the design of therapeutic strategies for amyloid diseases. Neurobiol. Dis., Pathogenic templating proteins in Neurodegenerative Disease 109, 178–190.
31. Danzer, K.M., Kranich, L.R., Ruf, W.P., Cagsal-Getkin, O., Winslow, A.R., Zhu, L., Vanderburg, C.R., McLean, P.J., 2012. Exosomal cell-to-cell transmission of alpha synuclein oligomers. Mol. Neurodegener. 7, 42.
32. Dear, A.J., Meisl, G., Šarić, A., Michaels, T.C.T., Kjaergaard, M., Linse, S., Knowles, T.P.J., 2020. Identification of on- and off-pathway oligomers in amyloid fibril formation. Chem. Sci. 11, 6236–6247.
33. Demuro, A., Mina, E., Kayed, R., Milton, S.C., Parker, I., Glabe, C.G., 2005. Calcium dysregulation and membrane disruption as a ubiquitous neurotoxic mechanism of soluble amyloid oligomers. J. Biol. Chem. 280, 17294–17300.
34. Dergalev, A.A., Alexandrov, A.I., Ivannikov, R.I., Ter-Avanesyan, M.D., Kushnirov, V.V., 2019. Yeast Sup35 Prion Structure: Two Types, Four Parts, Many Variants. Int. J. Mol. Sci. 20.

35. Dobson, C.M., Knowles, T.P.J., Vendruscolo, M., 2020. The Amyloid Phenomenon and Its Significance in Biology and Medicine. Cold Spring Harb. Perspect. Biol. 12, a033878.

36. Drisaldi, B., Colnaghi, L., Fioriti, L., Rao, N., Myers, C., Snyder, A.M., Metzger, D.J., Tarasoff, J., Konstantinov, E., Fraser, P.E., Manley, J.L., Kandel, E.R., 2015. SUMOylation Is an Inhibitory Constraint that Regulates the Prion-like Aggregation and Activity of CPEB3. Cell Rep. 11, 1694–1702.

37. Eichner, T., Radford, S.E., 2011. A Diversity of Assembly Mechanisms of a Generic Amyloid Fold. Mol. Cell 43, 8–18.

38. Eisenberg, D., Jucker, M., 2012. The Amyloid State of Proteins in Human Diseases. Cell 148, 1188–1203.

39. Fernández, M.R., Batlle, C., Gil-García, M., Ventura, S., 2017. Amyloid cores in prion domains: Key regulators for prion conformational conversion. Prion 11, 31–39.

40. Fioriti, L., Myers, C., Huang, Y.-Y., Li, X., Stephan, J.S., Trifilieff, P., Colnaghi, L., Kosmidis, S., Drisaldi, B., Pavlopoulos, E., Kandel, E.R., 2015. The Persistence of Hippocampal-Based Memory Requires Protein Synthesis Mediated by the Prion-like Protein CPEB3. Neuron 86, 1433–48.

41. Fitzpatrick, A.W.P., Debelouchina, G.T., Bayro, M.J., Clare, D.K., Caporini, M.A., Bajaj, V.S., Jaroniec, C.P., Wang, L., Ladizhansky, V., Muller, S.A., MacPhee, C.E., Waudby, C.A., Mott, H.R., De Simone, A., Knowles, T.P.J., Saibil, H.R., Vendruscolo, M., Orlova, E.V., Griffin, R.G., Dobson, C.M., 2013. Atomic structure and hierarchical assembly of a cross- amyloid fibril. Proc. Natl. Acad. Sci. 110, 5468–5473.

42. Gallardo, R., Ranson, N.A., Radford, S.E., 2020. Amyloid structures: much more than just a cross-β fold. Curr. Opin. Struct. Biol., Folding and Binding ● Proteins 60, 7–16.

43. Gaspar, R., Meisl, G., Buell, A.K., Young, L., Kaminski, C.F., Knowles, T.P.J., Sparr, E., Linse, S., 2017. Secondary nucleation of monomers on fibril surface dominates α -synuclein aggregation and provides autocatalytic amyloid amplification. Q. Rev. Biophys. 50, e6.
44. Giasson, B.I., Lee, V.M.Y., Trojanowski, J.Q., 2003. Interactions of amyloidogenic proteins. NeuroMolecular Med. 4, 49–58.
45. Greenwald, J., Riek, R., 2010. Biology of Amyloid: Structure, Function, and Regulation. Structure 18, 1244–1260.
46. Griffith, J.S., 1967. Nature of the Scrapie Agent: Self-replication and Scrapie. Nature 215, 1043–1044.
47. Guenther, E.L., Ge, P., Trinh, H., Sawaya, M.R., Cascio, D., Boyer, D.R., Gonen, T., Zhou, Z.H., Eisenberg, D.S., 2018. Atomic-level evidence for packing and positional amyloid polymorphism by segment from TDP-43 RRM2. Nat. Struct. Mol. Biol. 25, 311–319.
48. Hashimoto, M., Hsu, L.J., Xia, Y., Takeda, A., Sisk, A., Sundsmo, M., Masliah, E., 1999. Oxidative stress induces amyloid-like aggregate formation of NACP/α-synuclein in vitro. NeuroReport 10, 717.
49. Horwich, A.L., 2011. Protein folding in the cell: an inside story. Nat. Med. 17, 1211–1216.
50. Invernizzi, G., Papaleo, E., Sabate, R., Ventura, S., 2012. Protein aggregation: Mechanisms and functional consequences. Int. J. Biochem. Cell Biol. 44, 1541–1554.
51. Jackson, M.P., Hewitt, E.W., 2017. Why are Functional Amyloids Non-Toxic in Humans? Biomolecules 7, 71.

52. Jarrett, J.T., Lansbury, P.T., 1993. Seeding “one-dimensional crystallization” of amyloid: A pathogenic mechanism in Alzheimer’s disease and scrapie? Cell 73, 1055–1058.

53. Jeon, I., Cicchetti, F., Cisbani, G., Lee, S., Li, E., Bae, J., Lee, N., Li, L., Im, W., Kim, M., Kim, H.S., Oh, S.-H., Kim, T.-A., Ko, J.J., Aubé, B., Oueslati, A., Kim, Y.J., Song, J., 2016. Human-to-mouse prion-like propagation of mutant huntingtin protein. Acta Neuropathol. (Berl.) 132, 577–592.

54. Jeong, J.S., Ansaloni, A., Mezzenga, R., Lashuel, H.A., Dietler, G., 2013. Novel mechanistic insight into the molecular basis of amyloid polymorphism and secondary nucleation during amyloid formation. J. Mol. Biol. 425, 1765–1781.

55. Kaminski Schierle, G.S., van de Linde, S., Erdelyi, M., Esbjörner, E.K., Klein, T., Rees, E., Bertoncini, C.W., Dobson, C.M., Sauer, M., Kaminski, C.F., 2011. In Situ Measurements of the Formation and Morphology of Intracellular β-Amyloid Fibrils by Super-Resolution Fluorescence Imaging. J. Am. Chem. Soc. 133, 12902–12905.

56. Karube, H., Sakamoto, M., Arawaka, S., Hara, S., Sato, H., Ren, C.-H., Goto, S., Koyama, S., Wada, M., Kawanami, T., Kurita, K., Kato, T., 2008. N-terminal region of α-synuclein is essential for the fatty acid-induced oligomerization of the molecules. FEBS Lett. 582, 3693–3700.

57. Ke, P.C., Zhou, R., Serpell, L.C., Riek, R., Knowles, T.P.J., Lashuel, H.A., Gazit, E., Hamley, I.W., Davis, T.P., Fändrich, M., Otzen, D.E., Chapman, M.R., Dobson, C.M., Eisenberg, D.S., Mezzenga, R., 2020. Half a century of amyloids: past, present and future. Chem. Soc. Rev.

58. Khurana, R., Uversky, V.N., Nielsen, L., Fink, A.L., 2001. Is Congo Red an Amyloid-specific Dye? J. Biol. Chem. 276, 22715–22721.

59. Kilpatrick, K., Novoa, J.A., Hancock, T., Guerriero, C.J., Wipf, P., Brodsky, J.L., Segatori, L., 2013. Chemical Induction of Hsp70 Reduces α-Synuclein Aggregation in Neuroglioma Cells. ACS Chem. Biol. 8, 1460–1468.
60. Knowles, T.P.J., Vendruscolo, M., Dobson, C.M., 2014. The amyloid state and its association with protein misfolding diseases. Nat. Rev. Mol. Cell Biol. 15, 384–396.
61. Konno, H., Watanabe-Nakayama, T., Uchihashi, T., Okuda, M., Zhu, L., Kodera, N., Kikuchi, Y., Ando, T., Taguchi, H., 2020. Dynamics of oligomer and amyloid fibril formation by yeast prion Sup35 observed by high-speed atomic force microscopy. Proc. Natl. Acad. Sci. 117, 7831–7836.
62. Krebs, M.R.H., Morozova-Roche, L.A., Daniel, K., Robinson, C.V., Dobson, C.M., 2004. Observation of sequence specificity in the seeding of protein amyloid fibrils. Protein Sci. Publ. Protein Soc. 13, 1933–1938.
63. Kuchibhotla, K.V., Goldman, S.T., Lattarulo, C.R., Wu, H.-Y., Hyman, B.T., Bacskai, B.J., 2008. Aβ Plaques Lead to Aberrant Regulation of Calcium Homeostasis In Vivo Resulting in Structural and Functional Disruption of Neuronal Networks. Neuron 59, 214–225.
64. Kyle, R.A., 2001. Amyloidosis: a convoluted story. Br. J. Haematol. 114, 529–538.
65. Laron, Z., 2018. The Era of Cadaveric Pituitary Extracted Human Growth Hormone (1958-1985):Biological and Clinical Aspects. Pediatr. Endocrinol. Rev. PER 16, 11–16.
66. Lees, A.J., Hardy, J., Revesz, T., 2009. Parkinson's disease. Lancet Lond. Engl. 373, 2055–2066.
67. Leifer, B.P., 2009. Alzheimer's disease: Seeing the signs early. J. Am. Acad. Nurse Pract. 21, 588–595.

68. Leopold, P.E., Montal, M., Onuchic, J.N., 1992. Protein folding funnels: a kinetic approach to the sequence-structure relationship. Proc. Natl. Acad. Sci. 89, 8721–8725.
69. Li, J., McQuade, T., Siemer, A.B., Napetschnig, J., Moriwaki, K., Hsiao, Y.-S., Damko, E., Moquin, D., Walz, T., McDermott, A., Chan, F.K.-M., Wu, H., 2012. The RIP1/RIP3 Necrosome Forms a Functional Amyloid Signaling Complex Required for Programmed Necrosis. Cell 150, 339–350.
70. Linse, S., 2019. Mechanism of amyloid protein aggregation and the role of inhibitors. Pure Appl. Chem. 91, 211–229.
71. Lipinski, M.M., Zheng, B., Lu, T., Yan, Z., Py, B.F., Ng, A., Xavier, R.J., Li, C., Yankner, B.A., Scherzer, C.R., Yuan, J., 2010. Genome-wide analysis reveals mechanisms modulating autophagy in normal brain aging and in Alzheimer's disease. Proc. Natl. Acad. Sci. 107, 14164–14169.
72. Liu, B., Moloney, A., Meehan, S., Morris, K., Thomas, S.E., Serpell, L.C., Hider, R., Marciniak, S.J., Lomas, D.A., Crowther, D.C., 2011. Iron Promotes the Toxicity of Amyloid β Peptide by Impeding Its Ordered Aggregation. J. Biol. Chem. 286, 4248–4256.
73. Lutter, L., Serpell, C.J., Tuite, M.F., Xue, W.-F., 2019. The molecular lifecycle of amyloid – Mechanism of assembly, mesoscopic organisation, polymorphism, suprastructures, and biological consequences. Biochim. Biophys. Acta BBA - Proteins Proteomics 1867, 140257.
74. Mack, K.L., Shorter, J., 2016. Engineering and Evolution of Molecular Chaperones and Protein Disaggregases with Enhanced Activity. Front. Mol. Biosci. 3.
75. Maji, S.K., Perrin, M.H., Sawaya, M.R., Jessberger, S., Vadodaria, K., Rissman, R.A., Singru, P.S., Nilsson, K.P.R., Simon, R., Schubert, D., Eisenberg, D., Rivier, J.,

Sawchenko, P., Vale, W., Riek, R., 2009. Functional amyloids as natural storage of peptide hormones in pituitary secretory granules. Science 325, 328–32.

76. Makky, A., Bousset, L., Polesel-Maris, J., Melki, R., 2016. Nanomechanical properties of distinct fibrillar polymorphs of the protein α-synuclein. Sci. Rep. 6, 37970.
77. Mandelkow, E.-M., Mandelkow, E., 2012. Biochemistry and cell biology of tau protein in neurofibrillary degeneration. Cold Spring Harb. Perspect. Med. 2, a006247.
78. Manni, G., Lewis, V., Senesi, M., Spagnolli, G., Fallarino, F., Collins, S.J., Mouillet-Richard, S., Biasini, E., 2020. The cellular prion protein beyond prion diseases. Swiss Med. Wkly. 150.
79. Marchante, R., Beal, D.M., Koloteva-Levine, N., Purton, T.J., Tuite, M.F., Xue, W.-F., 2017. The physical dimensions of amyloid aggregates control their infective potential as prion particles. eLife 6, e27109.
80. Marshall, K.E., Marchante, R., Xue, W.-F., Serpell, L.C., 2014. The relationship between amyloid structure and cytotoxicity. Prion 8, 192–196.
81. Martins, I.C., Kuperstein, I., Wilkinson, H., Maes, E., Vanbrabant, M., Jonckheere, W., Van Gelder, P., Hartmann, D., D'Hooge, R., De Strooper, B., Schymkowitz, J., Rousseau, F., 2008. Lipids revert inert Aβ amyloid fibrils to neurotoxic protofibrils that affect learning in mice. EMBO J. 27, 224–233.
82. Morris, A.M., Watzky, M.A., Agar, J.N., Finke, R.G., 2008. Fitting neurological protein aggregation kinetic data via a 2-step, minimal/"Ockham's razor" model: the Finke-Watzky mechanism of nucleation followed by autocatalytic surface growth. Biochemistry 47, 2413–2427.
83. Murphy, M.P., LeVine, H., 2010. Alzheimer's Disease and the β-Amyloid Peptide. J. Alzheimers Dis. JAD 19, 311.

84. Nagele, R.G., Wegiel, Jerzy, Venkataraman, V., Imaki, H., Wang, K.-C., Wegiel, Jarek, 2004. Contribution of glial cells to the development of amyloid plaques in Alzheimer's disease. Neurobiol. Aging 25, 663–674.

85. Nelson, R., Sawaya, M.R., Balbirnie, M., Madsen, A.Ø., Riekel, C., Grothe, R., Eisenberg, D., 2005. Structure of the cross-beta spine of amyloid-like fibrils. Nature 435, 773–778.

86. Nussbaum, J.M., Schilling, S., Cynis, H., Silva, A., Swanson, E., Wangsanut, T., Tayler, K., Wiltgen, B., Hatami, A., Rönicke, R., Reymann, K., Hutter-Paier, B., Alexandru, A., Jagla, W., Graubner, S., Glabe, C.G., Demuth, H.-U., Bloom, G.S., 2012. Prion-like behaviour and tau-dependent cytotoxicity of pyroglutamylated amyloid-β. Nature 485, 651–655.

87. Otzen, D., Riek, R., 2019. Functional Amyloids. Cold Spring Harb. Perspect. Biol. 11, a033860.

88. Ow, S.-Y., Dunstan, D.E., 2014. A brief overview of amyloids and Alzheimer's disease. Protein Sci. Publ. Protein Soc. 23, 1315–1331.

89. Owen, M.C., Gnutt, D., Gao, M., Wärmländer, S.K.T.S., Jarvet, J., Gräslund, A., Winter, R., Ebbinghaus, S., Strodel, B., 2019. Effects of in vivo conditions on amyloid aggregation. Chem. Soc. Rev. 48, 3946–3996.

90. Paleologou, K.E., Oueslati, A., Shakked, G., Rospigliosi, C.C., Kim, H.-Y., Lamberto, G.R., Fernandez, C.O., Schmid, A., Chegini, F., Gai, W.P., Chiappe, D., Moniatte, M., Schneider, B.L., Aebischer, P., Eliezer, D., Zweckstetter, M., Masliah, E., Lashuel, H.A., 2010. Phosphorylation at S87 Is Enhanced in Synucleinopathies, Inhibits α-Synuclein Oligomerization, and Influences Synuclein-Membrane Interactions. J. Neurosci. 30, 3184–3198.

91. Pallarès, I., Ventura, S., 2016. Understanding and predicting protein misfolding and aggregation: Insights from proteomics. PROTEOMICS 16, 2570–2581.

92. Patel, N., Ramachandran, S., Azimov, R., Kagan, B.L., Lal, R., 2015. Ion Channel Formation by Tau Protein: Implications for Alzheimer's Disease and Tauopathies. Biochemistry 54, 7320–7325.

93. Pawar, A.P., DuBay, K.F., Zurdo, J., Chiti, F., Vendruscolo, M., Dobson, C.M., 2005. Prediction of "Aggregation-prone" and "Aggregation-susceptible" Regions in Proteins Associated with Neurodegenerative Diseases. J. Mol. Biol. 350, 379–392.

94. Peduzzo, A., Linse, S., Buell, A.K., 2020. The Properties of α-Synuclein Secondary Nuclei Are Dominated by the Solution Conditions Rather than the Seed Fibril Strain. ACS Chem. Neurosci. 11, 909–918.

95. Penke, B., Szűcs, M., Bogár, F., 2020. Oligomerization and Conformational Change Turn Monomeric β-Amyloid and Tau Proteins Toxic: Their Role in Alzheimer's Pathogenesis. Molecules 25.

96. Pulawski, W., Ghoshdastider, U., Andrisano, V., Filipek, S., 2012. Ubiquitous Amyloids. Appl. Biochem. Biotechnol. 166, 1626–1643.

97. Purro, S.A., Farrow, M.A., Linehan, J., Nazari, T., Thomas, D.X., Chen, Z., Mengel, D., Saito, T., Saido, T., Rudge, P., Brandner, S., Walsh, D.M., Collinge, J., 2018. Transmission of amyloid-β protein pathology from cadaveric pituitary growth hormone. Nature 564, 415–419.

98. Roberts, B.R., Ryan, T.M., Bush, A.I., Masters, C.L., Duce, J.A., 2012. The role of metallobiology and amyloid-β peptides in Alzheimer's disease. J. Neurochem. 120, 149–166.

99. Sabate, R., Rousseau, F., Schymkowitz, J., Batlle, C., Ventura, S., 2015. Amyloids or prions? That is the question. Prion 9, 200–206.

100. Selkoe, D.J., Hardy, J., 2016. The amyloid hypothesis of Alzheimer's disease at 25 years. EMBO Mol. Med. 8, 595–608.

101. Serrano-Pozo, A., Frosch, M.P., Masliah, E., Hyman, B.T., 2011. Neuropathological alterations in Alzheimer disease. Cold Spring Harb. Perspect. Med. 1, a006189.

102. Shammas, S.L., Garcia, G.A., Kumar, S., Kjaergaard, M., Horrocks, M.H., Shivji, N., Mandelkow, Eva, Knowles, T.P.J., Mandelkow, Eckhard, Klenerman, D., 2015. A mechanistic model of tau amyloid aggregation based on direct observation of oligomers. Nat. Commun. 6, 1–10.

103. Sigurdson, C.J., Bartz, J.C., Glatzel, M., 2019. Cellular and Molecular Mechanisms of Prion Disease. Annu. Rev. Pathol. Mech. Dis. 14, 497–516.

104. Sorrentino, Z.A., Giasson, B.I., 2020. The emerging role of α-synuclein truncation in aggregation and disease. J. Biol. Chem. 295, 10224–10244.

105. Stohr, J., Weinmann, N., Wille, H., Kaimann, T., Nagel-Steger, L., Birkmann, E., Panza, G., Prusiner, S.B., Eigen, M., Riesner, D., 2008. Mechanisms of prion protein assembly into amyloid. Proc. Natl. Acad. Sci. 105, 2409–2414.

106. Tabner, B.J., Turnbull, S., El-Agnaf, O.M.A., Allsop, D., 2002. Formation of hydrogen peroxide and hydroxyl radicals from Aβ and α-synuclein as a possible mechanism of cell death in Alzheimer's disease and Parkinson's disease. Free Radic. Biol. Med. 32, 1076–1083.

107. Tanaka, M., Collins, S.R., Toyama, B.H., Weissman, J.S., 2006. The physical basis of how prion conformations determine strain phenotypes. Nature 442, 585–589.

108. Tarutani, A., Arai, T., Murayama, S., Hisanaga, S., Hasegawa, M., 2018. Potent prion-like behaviors of pathogenic α-synuclein and evaluation of inactivation methods. Acta Neuropathol. Commun. 6, 29.

109. Torrente, M.P., Shorter, J., 2013. The metazoan protein disaggregase and amyloid depolymerase system: Hsp110, Hsp70, Hsp40, and small heat shock proteins. Prion 7, 457–463.

110. Ubeda-Bañon, I., Saiz-Sanchez, D., Flores-Cuadrado, A., Rioja-Corroto, E., Gonzalez-Rodriguez, M., Villar-Conde, S., Astillero-Lopez, V., Cabello-de la Rosa, J.P., Gallardo-Alcañiz, M.J., Vaamonde-Gamo, J., Relea-Calatayud, F., Gonzalez-Lopez, L., Mohedano-Moriano, A., Rabano, A., Martinez-Marcos, A., 2020. The human olfactory system in two proteinopathies: Alzheimer's and Parkinson's diseases. Transl. Neurodegener. 9, 22.

111. Uversky, V.N., Li, J., Fink, A.L., 2001. Evidence for a partially folded intermediate in alpha-synuclein fibril formation. J. Biol. Chem. 276, 10737–10744.

112. Vanden Berghe, T., Hassannia, B., Vandenabeele, P., 2016. An outline of necrosome triggers. Cell. Mol. Life Sci. CMLS 73, 2137–52.

113. Vestergaard, B., Groenning, M., Roessle, M., Kastrup, J.S., Weert, M. van de, Flink, J.M., Frokjaer, S., Gajhede, M., Svergun, D.I., 2007. A Helical Structural Nucleus Is the Primary Elongating Unit of Insulin Amyloid Fibrils. PLOS Biol. 5, e134.

114. Wentink, A., Nussbaum-Krammer, C., Bukau, B., 2019. Modulation of Amyloid States by Molecular Chaperones. Cold Spring Harb. Perspect. Biol. 11.

115. Wong, Y.C., Holzbaur, E.L.F., 2015. Autophagosome dynamics in neurodegeneration at a glance. J. Cell Sci. 128, 1259–1267.

116. Wong, Y.C., Holzbaur, E.L.F., 2014. The Regulation of Autophagosome Dynamics by Huntingtin and HAP1 Is Disrupted by Expression of Mutant Huntingtin, Leading to Defective Cargo Degradation. J. Neurosci. 34, 1293–1305.

117. Xue, W.-F., Hellewell, A.L., Gosal, W.S., Homans, S.W., Hewitt, E.W., Radford, S.E., 2009. Fibril Fragmentation Enhances Amyloid Cytotoxicity. J. Biol. Chem. 284, 34272–34282.

118. Zandomeneghi, G., Krebs, M.R.H., McCammon, M.G., Fändrich, M., 2004. FTIR reveals structural differences between native beta-sheet proteins and amyloid fibrils. Protein Sci. Publ. Protein Soc. 13, 3314–3321.

SUPPLEMENTARY INFORMATION

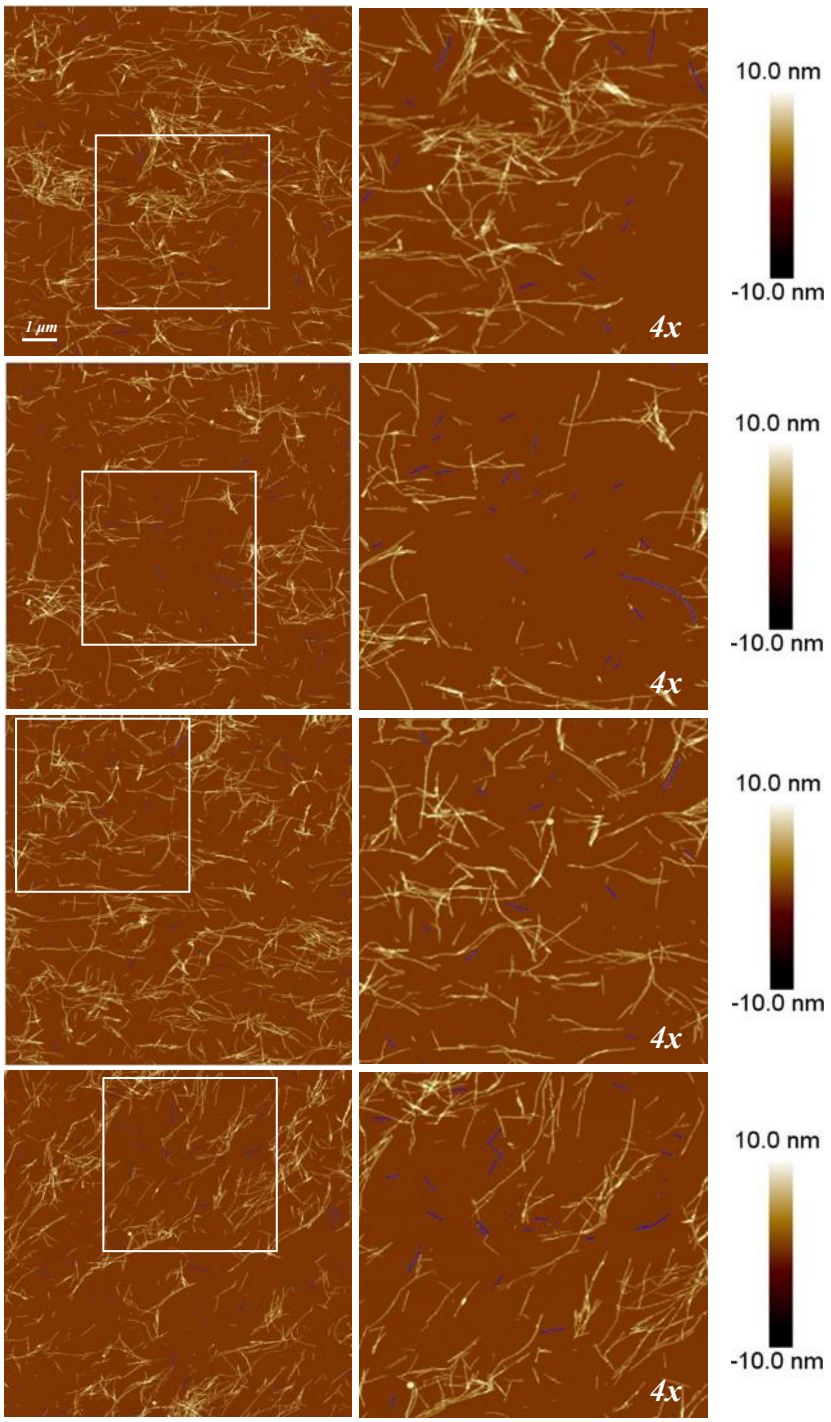

Supplementary figure 1- AFM images of traced α-synuclein fibrils in the plateau phase. *Fibril samples produced de novo using a monomeric concentration of 2.1 µM. The images are 10 µm x 10 µm in scan size at a resolution of 1024 x 1024 pixel. This size is represented by the scale bar. The height bar shows a range of 20 nm from -10 nm to +10 nm with respect to the mica surface. No processing was performed.*

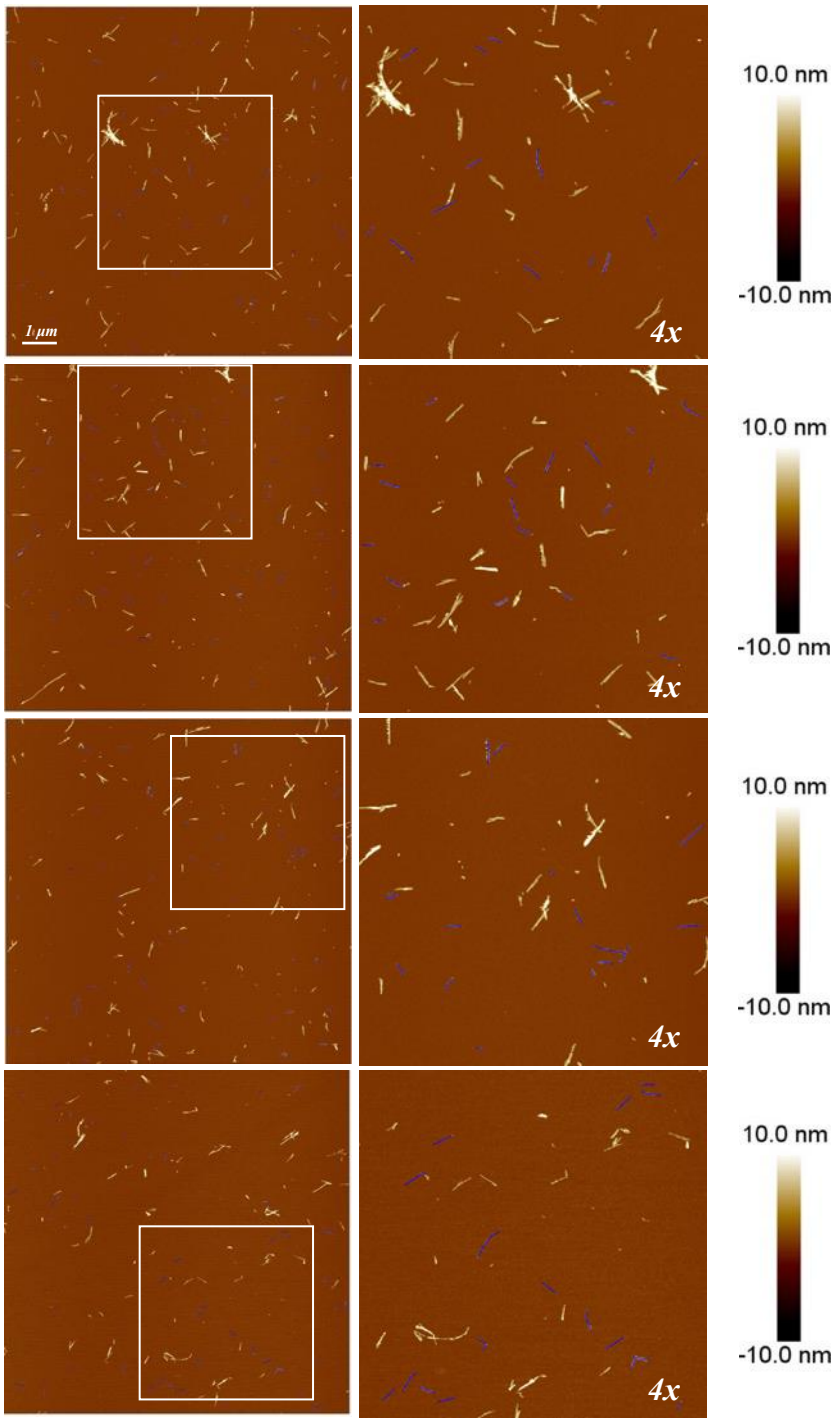

Supplementary figure 2- AFM images of traced α-synuclein fibrils pulse sonicated for 5 seconds. *Fibril samples produced de novo using 2.1 µM monomeric α-synuclein that was pulse sonicated for 5 seconds at 20 kHz and 20% amplitude. The images are 10 µm x 10 µm in scan size at a resolution of 1024 x 1024 pixel. This size is represented by the scale bar. The height bar shows a range of 20 nm from -1 nm to +10 nm with respect to the mica surface. No processing was performed.*

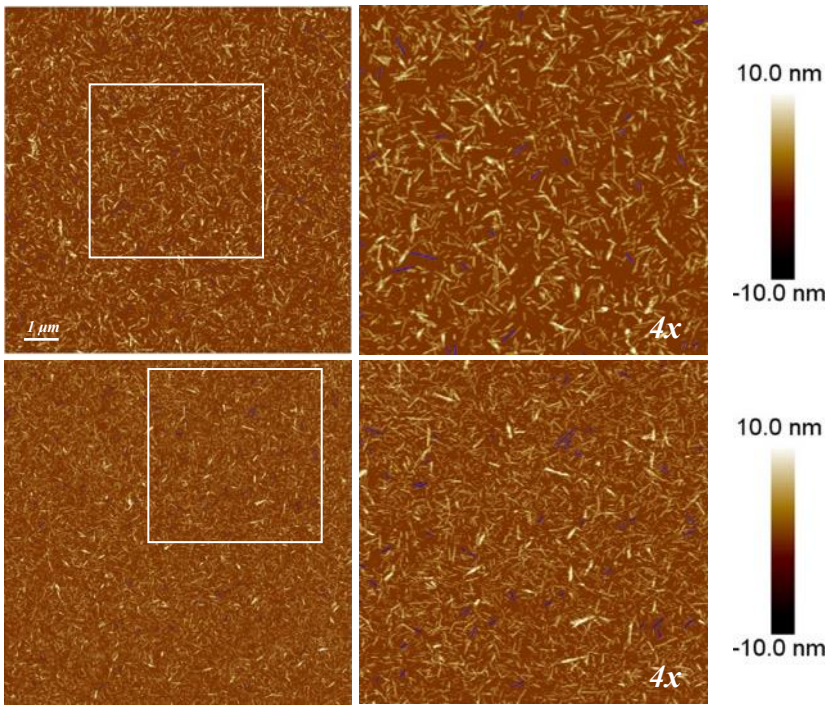

Supplementary figure 3- AFM images of traced α-synuclein fibrils pulse sonicated for 20 seconds. *Fibril samples produced de novo using 0.2 µM monomeric α-synuclein that was pulse sonicated for 5 seconds at 20 kHz and 20% amplitude. The images are 10 µm x 10 µm in scan size at a resolution of 1024 x 1024 pixel. This size is represented by the scale bar. The height bar shows a range of 20 nm from -1 nm to +10 nm with respect to the mica surface. No processing was performed.*

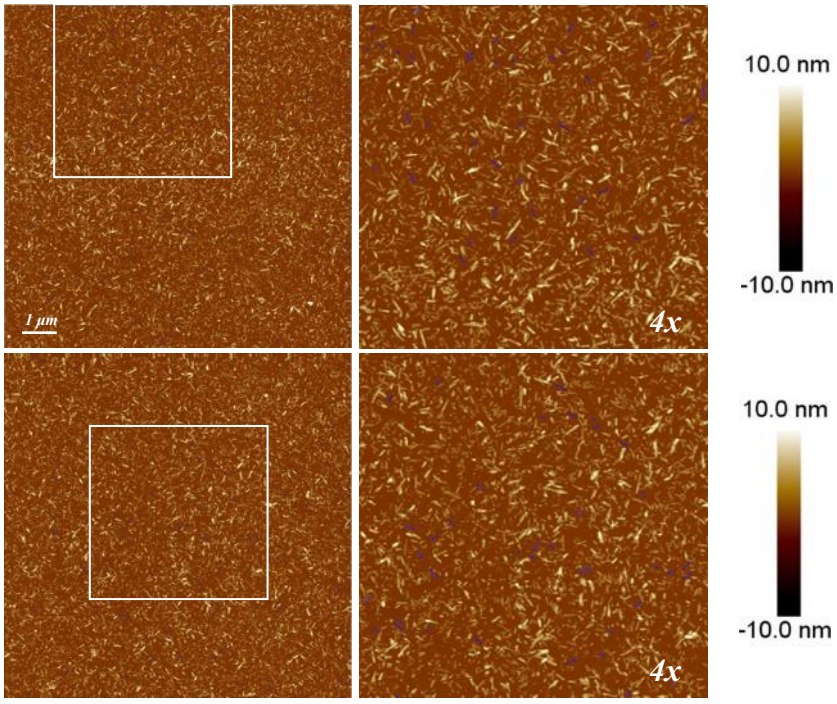

Supplementary figure 4- AFM images of traced α-synuclein fibrils pulse sonicated for 80 seconds. *Fibril samples produced de novo using 0.2 µM monomeric α-synuclein that was pulse sonicated for 5 seconds at 20 kHz and 20% amplitude. The images are 10 µm x 10 µm in scan size at a resolution of 1024 x 1024 pixel. This size is represented by the scale bar. The height bar shows a range of 20 nm from -1 nm to +10 nm with respect to the mica surface. No processing was performed.*

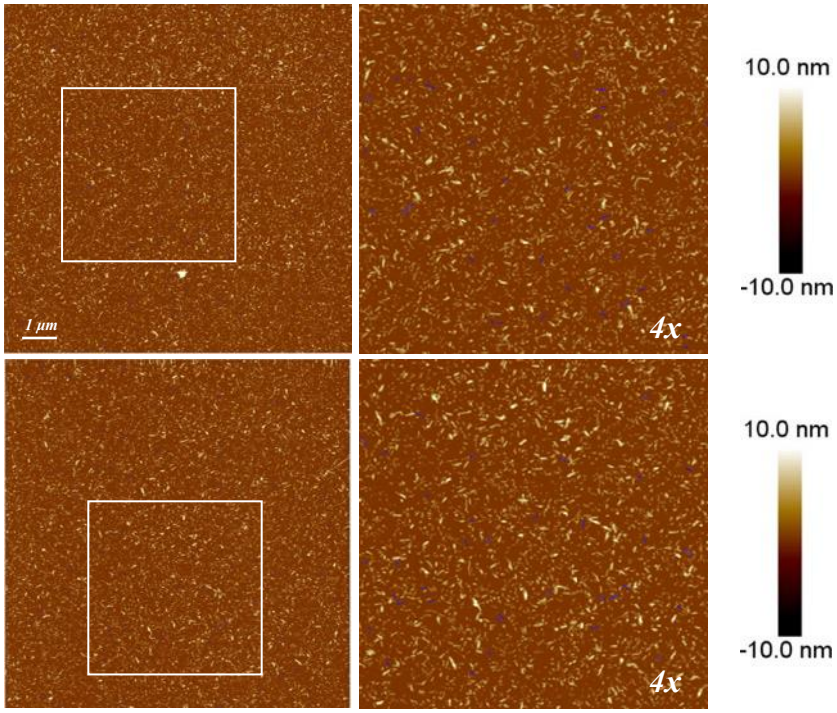

Supplementary figure 5- AFM images of traced α-synuclein fibrils pulse sonicated for 320 seconds. *Fibril samples produced de novo using 0.2 µM monomeric α-synuclein that was pulse sonicated for 5 seconds at 20 kHz and 20% amplitude. The images are 10 µm x 10 µm in scan size at a resolution of 1024 x 1024 pixel. This size is represented by the scale bar. The height bar shows a range of 20 nm from -1 nm to +10 nm with respect to the mica surface. No processing was performed.*

Supplementary Table 1- Morphometric parameters of individual fibrils traced in each α-synuclein sample. *The length of each fibril was calculated by multiplying the lContour value of each fibril by the resolution. The mean height of each fibril (indicative of fibril width) was provided by calculating the mean of the Z values of each fibril.*

Amyloid particle length/nm						**Mean amyloid particle height/nm**				
Sample										
De novo	**5s**	**20s**	**80s**	**320**		**De novo**	**5s**	**20**	**80s**	**320s**
39.3	68.7	39.3	58.9	58.8		3.3	3.4	2.8	2.7	3.3
39.3	68.8	49.1	59.2	58.9		3.5	3.5	2.8	2.7	3.4
39.3	78.7	58.7	68.7	58.9		3.6	3.7	2.8	3.2	3.5
49.1	88.0	58.8	68.7	58.9		3.7	3.8	2.9	3.3	3.6
49.1	88.3	58.8	68.7	58.9		3.8	3.8	2.9	3.3	3.6
49.1	88.4	58.9	68.7	58.9		3.9	3.9	2.9	3.3	3.8
49.1	88.6	68.3	68.7	58.9		4.0	3.9	2.9	3.4	3.8
58.8	88.7	68.4	68.7	58.9		4.0	3.9	3.0	3.4	3.9
58.8	97.7	68.4	69.1	59.0		4.0	4.0	3.0	3.5	3.9
58.9	97.8	68.4	78.0	59.0		4.0	4.0	3.0	3.7	3.9
58.9	98.1	68.5	78.4	59.1		4.1	4.0	3.0	3.8	4.0
58.9	107.4	68.5	78.5	68.4		4.1	4.1	3.0	3.8	4.0
58.9	107.5	68.7	78.5	68.5		4.2	4.2	3.0	3.9	4.0
58.9	107.9	68.7	78.5	68.6		4.3	4.2	3.0	3.9	4.1
58.9	107.9	68.7	78.5	68.6		4.3	4.2	3.1	3.9	4.1
68.4	108.0	68.7	78.5	68.6		4.3	4.3	3.1	4.0	4.1
68.5	108.0	78.2	78.5	68.6		4.3	4.3	3.1	4.0	4.2

68.6	108.1	78.2	78.5	68.6		4.4	4.3	3.1	4.0	4.2
68.7	109.1	78.2	78.5	68.6		4.4	4.3	3.1	4.0	4.2
68.7	116.7	78.2	78.5	68.7		4.4	4.3	3.2	4.0	4.3
68.7	117.3	78.2	78.5	68.7		4.4	4.3	3.2	4.1	4.3
68.8	117.3	78.3	78.5	68.7		4.5	4.3	3.2	4.1	4.3
69.0	117.3	78.4	78.5	68.7		4.5	4.3	3.3	4.1	4.4
78.5	117.4	78.5	78.5	68.7		4.5	4.4	3.3	4.1	4.4
78.5	117.4	78.7	78.5	68.7		4.6	4.4	3.3	4.2	4.4
78.5	117.5	88.0	78.5	68.7		4.7	4.4	3.3	4.2	4.4
78.5	117.7	88.0	78.6	68.7		4.7	4.4	3.3	4.2	4.4
78.5	117.8	88.2	78.7	68.8		4.7	4.4	3.4	4.2	4.4
78.5	118.4	88.4	78.8	68.8		4.7	4.4	3.4	4.2	4.4
78.5	127.1	88.5	78.9	68.9		4.7	4.4	3.4	4.2	4.5
78.5	127.1	89.3	79.2	69.1		4.8	4.4	3.4	4.3	4.5
78.5	127.1	89.8	79.4	69.1		4.8	4.4	3.5	4.3	4.5
78.6	127.1	97.4	88.2	69.3		4.8	4.4	3.5	4.3	4.5
78.6	127.1	97.8	88.3	77.7		4.8	4.4	3.5	4.3	4.5
88.3	127.1	97.9	88.3	78.0		4.9	4.4	3.5	4.3	4.6
88.3	127.2	97.9	88.3	78.2		4.9	4.5	3.6	4.4	4.6
88.3	127.3	97.9	88.3	78.2		4.9	4.5	3.6	4.4	4.6
88.6	127.6	98.0	88.3	78.2		4.9	4.5	3.6	4.4	4.6
88.7	136.9	98.1	88.3	78.3		4.9	4.5	3.6	4.4	4.6
98.1	136.9	98.1	88.3	78.3		4.9	4.5	3.6	4.4	4.7
98.1	136.9	98.2	88.3	78.4		4.9	4.5	3.6	4.4	4.7

98.1	136.9	98.2	88.3	78.5	4.9	4.5	3.6	4.4	4.7
98.1	137.7	98.2	88.3	78.5	4.9	4.5	3.7	4.5	4.7
98.1	146.6	98.4	88.3	78.5	5.0	4.6	3.7	4.5	4.7
98.1	146.6	98.4	88.3	78.5	5.0	4.6	3.7	4.5	4.8
98.1	146.6	99.6	88.3	78.5	5.0	4.6	3.7	4.5	4.8
98.1	146.6	99.9	88.4	78.5	5.0	4.6	3.7	4.5	4.8
98.1	147.1	107.5	88.4	78.5	5.0	4.6	3.8	4.5	4.8
98.1	147.2	107.5	88.4	78.5	5.0	4.6	3.8	4.5	4.8
98.1	147.2	107.5	88.4	78.5	5.0	4.6	3.8	4.5	4.8
98.2	147.2	107.5	88.5	78.5	5.0	4.6	3.8	4.5	4.9
98.2	147.2	107.5	88.6	78.5	5.0	4.6	3.8	4.5	4.9
98.2	155.9	107.5	88.6	78.5	5.0	4.6	3.9	4.6	4.9
107.6	156.4	107.5	88.7	78.5	5.0	4.6	3.9	4.6	4.9
107.8	156.4	107.5	89.3	78.5	5.0	4.6	3.9	4.6	4.9
107.9	156.4	107.5	89.6	78.5	5.0	4.6	3.9	4.6	4.9
108.0	156.6	107.6	97.9	78.5	5.0	4.7	3.9	4.6	5.0
117.7	157.0	107.6	98.0	78.5	5.1	4.7	3.9	4.6	5.0
117.8	157.1	107.7	98.0	78.5	5.1	4.7	4.0	4.6	5.0
117.8	157.1	107.8	98.1	78.5	5.1	4.7	4.0	4.7	5.0
117.8	166.0	107.9	98.1	78.5	5.1	4.7	4.0	4.7	5.0
117.8	166.2	108.0	98.1	78.5	5.1	4.7	4.0	4.7	5.0
117.8	166.2	108.0	98.1	78.5	5.1	4.7	4.0	4.7	5.1
117.8	166.2	108.0	98.1	78.5	5.1	4.7	4.0	4.7	5.1
117.8	166.2	108.0	98.1	78.5	5.1	4.8	4.1	4.7	5.1

117.8	166.8	108.2	98.1	78.5	5.2	4.8	4.1	4.7	5.1
117.9	166.8	108.5	98.1	78.6	5.2	4.8	4.1	4.8	5.2
118.1	175.4	117.3	98.2	78.6	5.2	4.8	4.1	4.8	5.2
118.1	176.0	117.3	98.2	78.6	5.2	4.8	4.2	4.8	5.2
127.6	176.0	117.3	98.2	78.6	5.2	4.9	4.2	4.8	5.2
127.6	176.0	117.3	98.3	78.6	5.2	4.9	4.2	4.8	5.2
127.6	176.6	117.3	98.5	78.6	5.2	4.9	4.2	4.9	5.2
127.6	185.7	117.3	99.0	78.6	5.3	4.9	4.3	4.9	5.2
127.6	185.7	117.3	99.0	78.7	5.3	4.9	4.3	4.9	5.2
127.6	185.7	117.3	99.8	78.7	5.3	4.9	4.3	4.9	5.3
127.8	185.8	117.4	107.7	78.7	5.3	4.9	4.3	4.9	5.3
137.4	186.3	117.4	107.7	78.8	5.3	4.9	4.3	4.9	5.3
137.4	195.5	117.4	107.9	78.9	5.3	4.9	4.4	4.9	5.3
137.4	195.6	117.5	107.9	78.9	5.3	5.0	4.4	5.0	5.3
137.4	204.8	117.8	107.9	79.3	5.3	5.0	4.4	5.0	5.4
138.0	205.0	117.8	107.9	87.5	5.3	5.0	4.4	5.0	5.4
138.6	205.3	117.9	107.9	88.1	5.3	5.0	4.5	5.0	5.4
146.9	205.3	117.9	107.9	88.1	5.3	5.0	4.5	5.0	5.4
147.2	205.3	118.0	108.0	88.2	5.4	5.0	4.5	5.0	5.4
147.2	205.3	118.2	108.1	88.2	5.4	5.0	4.6	5.0	5.5
147.2	205.3	118.3	108.2	88.3	5.4	5.0	4.6	5.0	5.5
147.2	205.3	126.9	108.4	88.3	5.4	5.0	4.6	5.0	5.5
147.2	205.3	126.9	108.7	88.3	5.4	5.0	4.6	5.1	5.5
147.2	205.3	127.1	110.4	88.3	5.5	5.1	4.6	5.1	5.5

147.2	205.3	127.1	117.5	88.3	5.5	5.1	4.6	5.1	5.5
147.2	205.4	127.1	117.6	88.3	5.5	5.1	4.6	5.1	5.5
147.2	206.1	127.1	117.8	88.3	5.5	5.1	4.7	5.1	5.5
147.3	215.0	127.1	117.8	88.3	5.5	5.1	4.7	5.1	5.5
147.6	215.0	127.1	117.8	88.3	5.5	5.1	4.7	5.1	5.5
157.0	215.1	127.1	117.8	88.3	5.5	5.1	4.8	5.1	5.6
157.0	215.1	127.1	117.8	88.4	5.5	5.1	4.8	5.1	5.6
157.0	215.1	127.2	117.8	88.4	5.6	5.1	4.8	5.1	5.6
157.0	215.1	127.4	117.8	88.4	5.6	5.1	4.8	5.1	5.6
157.0	215.2	127.5	117.8	88.4	5.6	5.1	4.8	5.1	5.6
157.1	215.9	127.5	117.8	88.4	5.6	5.1	4.8	5.1	5.6
157.1	224.5	127.6	117.8	88.4	5.6	5.1	4.8	5.2	5.6
166.5	224.8	127.6	117.8	88.4	5.6	5.1	4.8	5.2	5.7
166.6	224.9	127.6	117.8	88.4	5.6	5.2	4.8	5.2	5.7
166.8	234.6	127.9	117.8	88.4	5.6	5.2	4.8	5.2	5.7
166.8	234.6	128.1	117.9	88.4	5.6	5.2	4.9	5.2	5.7
166.8	234.6	128.7	118.0	88.4	5.6	5.2	4.9	5.2	5.8
166.9	235.5	136.8	118.0	88.5	5.7	5.2	4.9	5.3	5.8
167.0	235.5	136.8	118.1	88.5	5.7	5.2	4.9	5.3	5.8
167.0	244.4	136.8	118.4	88.7	5.7	5.2	4.9	5.3	5.9
167.2	244.4	136.9	118.5	88.9	5.7	5.2	5.0	5.3	5.9
167.4	244.4	136.9	119.6	89.1	5.7	5.2	5.0	5.3	5.9
176.6	244.6	137.0	127.4	89.1	5.7	5.2	5.0	5.3	5.9
176.6	244.7	137.4	127.5	89.1	5.8	5.2	5.0	5.3	5.9

176.6	245.3	137.4	127.6	89.6	5.8	5.2	5.0	5.3	5.9
176.6	245.4	137.4	127.6	97.4	5.8	5.2	5.0	5.4	6.0
176.6	245.4	137.6	127.6	97.9	5.8	5.2	5.0	5.4	6.0
176.7	245.6	137.7	127.6	98.1	5.8	5.3	5.0	5.4	6.0
176.8	254.1	137.9	127.6	98.1	5.8	5.3	5.0	5.4	6.0
176.8	254.2	139.2	127.6	98.1	5.8	5.3	5.0	5.4	6.0
186.4	254.2	146.6	127.6	98.1	5.8	5.3	5.0	5.4	6.0
186.5	254.2	146.6	127.6	98.1	5.8	5.3	5.0	5.4	6.0
186.5	254.2	146.7	127.6	98.1	5.8	5.3	5.1	5.5	6.1
186.5	254.2	146.7	127.6	98.1	5.8	5.3	5.1	5.5	6.1
186.5	254.2	146.7	127.6	98.2	5.8	5.3	5.1	5.5	6.1
186.5	255.2	146.9	127.6	98.2	5.9	5.4	5.1	5.5	6.1
186.5	255.2	147.2	127.6	98.2	5.9	5.4	5.2	5.5	6.1
186.6	263.9	147.2	127.6	98.2	5.9	5.4	5.2	5.5	6.1
187.7	263.9	147.2	127.7	98.2	5.9	5.4	5.2	5.5	6.2
195.9	263.9	147.2	127.7	98.2	5.9	5.4	5.2	5.6	6.2
196.2	264.0	147.3	127.7	98.2	5.9	5.4	5.2	5.6	6.2
196.2	264.0	147.4	127.7	98.3	5.9	5.4	5.2	5.6	6.2
196.3	264.0	147.4	127.9	98.4	5.9	5.4	5.3	5.6	6.3
196.3	264.1	148.0	128.2	98.4	5.9	5.4	5.3	5.6	6.3
196.3	265.0	148.3	128.2	98.4	5.9	5.5	5.3	5.6	6.4
196.3	265.0	148.7	128.4	98.5	6.0	5.5	5.3	5.6	6.4
196.3	273.7	156.3	128.6	98.5	6.0	5.5	5.3	5.7	6.4
196.5	273.7	156.3	129.5	98.7	6.0	5.5	5.3	5.7	6.5

196.6	274.1	156.5	137.4	98.8		6.0	5.5	5.3	5.7	6.6
206.1	274.8	156.7	137.4	99.9		6.0	5.5	5.3	5.7	6.6
206.1	283.6	156.8	137.4	100.3		6.0	5.5	5.3	5.7	6.6
206.1	284.5	157.0	137.5	101.0		6.0	5.5	5.4	5.7	6.6
206.1	284.6	157.0	137.5	107.7		6.0	5.5	5.4	5.7	6.7
206.5	293.3	157.1	137.6	107.8		6.1	5.5	5.4	5.7	6.7
215.9	293.3	157.5	137.6	107.9		6.1	5.6	5.4	5.7	6.7
215.9	293.3	158.2	137.6	108.0		6.1	5.6	5.4	5.8	6.8
215.9	293.3	159.6	137.9	108.0		6.1	5.6	5.4	5.8	6.8
215.9	293.3	166.2	137.9	108.0		6.1	5.6	5.5	5.8	6.8
225.6	294.4	166.2	138.0	108.0		6.1	5.6	5.5	5.8	6.9
225.7	294.4	166.4	138.0	108.0		6.1	5.6	5.5	5.8	7.0
225.7	303.0	166.5	138.0	108.0		6.1	5.6	5.5	5.9	7.0
225.7	303.0	166.7	147.1	108.1		6.1	5.6	5.6	5.9	7.0
225.7	304.2	166.8	147.2	108.3		6.1	5.7	5.6	5.9	7.0
225.7	304.2	166.9	147.2	108.4		6.1	5.7	5.7	5.9	7.1
225.9	304.2	166.9	147.2	109.0		6.1	5.7	5.7	6.0	7.1
226.0	312.8	166.9	147.2	110.4		6.2	5.7	5.7	6.0	7.1
226.2	312.8	167.0	147.2	117.7		6.2	5.7	5.7	6.0	7.1
235.5	312.9	176.0	147.2	117.8		6.2	5.7	5.7	6.0	7.1
235.5	313.1	176.0	147.2	117.8		6.2	5.7	5.7	6.0	7.3
235.5	314.0	176.0	147.3	117.8		6.2	5.7	5.7	6.0	7.3
235.5	314.4	176.6	147.3	117.8		6.2	5.7	5.7	6.1	7.4
235.5	322.6	176.6	147.3	117.8		6.2	5.7	5.8	6.1	7.4

235.6	322.6	185.7	147.4	117.8	6.3	5.7	5.8	6.1	7.4
255.2	322.6	185.8	147.4	117.8	6.3	5.7	5.8	6.1	7.5
255.2	322.6	185.8	147.4	117.8	6.3	5.8	5.8	6.1	7.5
255.2	332.4	186.3	147.8	117.9	6.3	5.8	5.8	6.2	7.6
255.5	332.4	186.5	149.0	117.9	6.3	5.8	5.8	6.2	7.7
265.0	332.8	186.5	157.0	118.0	6.4	5.8	5.9	6.2	7.7
266.1	333.7	186.5	157.0	118.1	6.4	5.8	5.9	6.3	7.7
274.3	333.7	186.8	157.0	118.6	6.4	5.8	6.0	6.3	7.8
274.8	342.1	188.4	157.0	119.1	6.4	5.9	6.1	6.3	7.8
274.8	342.1	195.5	157.1	119.4	6.4	5.9	6.1	6.3	7.9
275.5	342.1	196.1	157.1	120.3	6.4	5.9	6.2	6.3	7.9
284.6	342.1	196.2	157.2	127.6	6.5	5.9	6.2	6.4	8.0
294.4	342.3	196.3	157.2	127.6	6.6	5.9	6.3	6.4	8.1
304.2	351.9	196.3	157.2	127.7	6.6	5.9	6.4	6.5	8.2
304.2	353.3	196.3	157.3	127.8	6.6	5.9	6.4	6.5	8.2
304.2	353.5	205.3	157.3	127.9	6.6	6.0	6.4	6.6	8.2
304.3	361.1	206.1	157.4	128.4	6.6	6.0	6.5	6.6	8.3
304.4	361.7	206.2	157.6	129.4	6.6	6.0	6.5	6.6	8.4
314.0	361.7	215.1	166.5	137.2	6.6	6.0	6.6	6.6	8.4
314.1	361.8	215.2	166.9	137.3	6.6	6.0	6.6	6.7	8.6
323.9	373.0	215.4	166.9	137.4	6.6	6.0	6.6	6.7	8.6
324.0	381.2	215.9	167.0	137.4	6.7	6.1	6.7	6.7	8.6
333.7	381.2	215.9	167.0	137.4	6.7	6.1	6.8	6.8	8.7
344.3	381.3	216.1	167.4	137.5	6.8	6.1	6.8	6.8	8.7

363.1	381.7	216.3	176.7	137.5	6.8	6.1	6.8	6.9	8.8
363.1	391.2	216.3	176.7	138.5	6.8	6.1	6.8	7.1	9.2
363.1	400.8	225.7	177.8	147.2	6.9	6.2	7.0	7.1	9.2
372.9	400.8	235.4	178.5	147.2	6.9	6.2	7.1	7.1	9.3
373.0	400.8	235.5	186.5	147.2	6.9	6.2	7.1	7.2	9.4
412.2	430.8	255.2	186.5	147.2	6.9	6.3	7.1	7.3	9.4
412.3	439.9	255.2	186.5	147.2	7.0	6.3	7.3	7.3	9.4
441.6	440.2	255.7	186.5	147.2	7.0	6.3	7.7	7.4	9.4
471.0	449.7	263.9	186.6	147.3	7.0	6.5	7.8	7.4	9.4
490.7	469.3	274.9	187.0	147.3	7.1	6.5	7.8	7.4	9.5
520.2	479.0	284.6	206.1	147.7	7.3	6.6	7.9	7.7	9.9
539.6	479.1	304.2	206.1	157.2	7.3	6.7	7.9	8.0	9.9
569.3	488.7	304.2	206.1	157.2	7.5	6.8	8.1	8.4	9.9
578.9	500.5	314.2	206.2	167.0	7.7	7.0	8.7	8.7	10.0
579.0	528.1	315.5	245.4	176.8	7.8	7.5	8.9	8.8	10.2

Supplementary table 2- Quantitative analysis of the characterised lengths of α-synuclein fibrils in each sample. *The table shows the frequency of a range of various lengths of α-synuclein fibrils extracted from the length distribution plots.*

Amyloid particle count	Sample	Amyloid particle length / nm																							
		0-25	**25-50**	**50-75**	**75-100**	**100-125**	**125-150**	**150-175**	**175-200**	**200-225**	**225-250**	**250-275**	**275-300**	**300-325**	**325-350**	**350-375**	**375-400**	**400-425**	**425-450**	**450-475**	**475-500**	**500-525**	**525-550**	**550-575**	**575-600**
	De novo	0	7	17	30	16	25	17	27	9	15	9	3	9	2	5	0	2	1	1	1	1	1	1	2
	5s	0	0	2	9	18	23	15	12	24	14	22	10	15	10	8	5	3	4	1	3	1	1	0	0
	20s	0	2	14	31	39	49	21	20	11	3	5	1	4	0	0	0	0	0	0	0	0	0	0	0
	80s	0	0	9	66	36	55	19	10	4	1	0	0	0	0	0	0	0	0	0	0	0	0	0	0
	320s	0	0	33	106	33	24	3	1	0	0	0	0	0	0	0	0	0	0	0	0	0	0	0	0

Supplementary table 3- Quantitative analysis of the characterised widths of α-synuclein fibrils in each sample. *The table show the frequency of a range of heights (indicative of width) of α-synuclein fibrils extracted from the height distribution plots.*

	Sample	Amyloid particle height / nm																		
		0-0.5	**0.5-1**	**1-1.5**	**1.5-2**	**2-2.5**	**2.5-3**	**3-3.5**	**3.5-4**	**4-4.5**	**4.5-5**	**5-5.5**	**5.5-6**	**6-6.5**	**6.5-7**	**7-7.5**	**7.5-8**	**8-8.5**	**8.5-9**	**9-9.5**	**9.5-10**
Amyloid particle count	***De novo***	0	0	0	0	0	0	1	7	14	28	43	45	35	20	5	2	0	0	0	0
	5s	0	0	0	0	0	0	1	8	30	43	55	42	16	3	1	1	0	0	0	0
	20s	0	0	0	0	11	23	26	22	32	34	21	9	9	5	5	1	2	0	0	0
	80s	0	0	0	0	0	2	7	7	30	37	39	33	19	12	9	1	2	2	0	0
	320s	0	0	0	0	0	0	3	9	21	24	31	29	19	14	15	10	7	6	9	3